Study of the Mechanical and Metallurgical Properties of AMDRY 9954 HVOF Coated Ti-6Al-4V Alloy

By

Dahham M. Al-Anazi

BS & MSc in Mechanical Engineering

September 2007

This thesis is submitted to Dublin City University as the fulfillment of the requirement for the award of degree of

Doctor of Philosophy

Supervisors

Professor M.S.J. Hashmi
Professor B.S. Yilbas

School of Mechanical & Manufacturing Engineering
Dublin City University

I hereby certify that this material, which I now submit for assessment on the programme of study leading to the award of Doctor of Philosophy is my own work and has not been taken from the work of others save and to the extent that such work has been cited and acknowledged within the text of my work.

Signed: _____ ID No. 53134508

Date: _____

ACKNOWLEDGMENTS

First and foremost, all praise to Almighty, Allah Who gave me the courage and patience to carry out this work and I ask to accept my little effort. May He, *subhanahu-wat-Aala*, guide the humanity and me to the right path.

My deep appreciation to my Ph.D, thesis advisors Professor M.S.J. Hashmi from Dublin City University, Ireland and Professor B.S. Yilbas from King Fahd University of Petroleum and Minerals, Saudi Arabia for their continuous support and matchless patience throughout this work. Their suggestions were always valuable and working with them was always indeed a wonderful and learning experience. Continuously, they were supportive and kind to me.

I would also like to thank both Dublin City University in Ireland and King Fahd University of Petroleum and Minerals in Saudi Arabia for providing everything necessary to make this work possible.

Thanks are due to my employer Saudi Aramco for all helps and encouragements to complete this work.

Last but not least, I owe my beloved family, an expression of gratitude for their help, patience and encouragement.

Tile of Thesis: Study of the Mechanical and Metallurgical Properties of AMDRY 9954 HVOF Coated Ti-6Al-4V Alloy

Name of Student: Dahham M. Al-Anazi **Student Number**: 53134508

ABSTRACT

Ti-6Al-4V alloy is commonly used in gas turbines due to its excellent tensile and fatigue strength, corrosion resistance, and high toughness to mass ratio. In the present study, the metallurgical and mechanical properties of High Velocity Oxygen Fuel (HVOF) thermally sprayed AMDRY 9954 ($Co_{bal}.Ni_{32}Cr_{21}Al_8Y_{0.5}$) superalloy powder on Ti-6Al-4V alloy are examined. The mechanical tests include three point bending, tensile, fatigue, indentation, and microhardness tests. The mechanical tests are applied on Ti-6Al-4V specimens (a) as-received, (b) as-received heat treated, (c) coated then heat treated and (d) coated without heat treatment. Three-point bending tests are carried out to investigate the coating-base material interface properties and the influence of heat treatment on the interface properties. Tensile tests are performed to evaluate the adhesion of the thermally sprayed coating to Ti-6Al-4V alloy. The fatigue tests are conducted to study the fatigue resistance behavior of the coated substrate martial under fluctuating load. Finite element method (FEM) is introduced to simulate the bending and tensile testing situations and predict the stress distribution in the workpieces. In addition, the microhardness and the indentation tests are carried out to measure the hardness and estimate the plane fracture toughness of the coating, respectively. The metallurgical characterization and surface morphology prior and after mechanical testing are investigated using SEM, optical microscopy, EDS, and XRD. It is found that heat treatment modifies the elastic modulus of the coating; in addition, tensile and fatigue performance of the specimens subjected to the heat treatment is low.

Table of Contents

		Page
Declaration		2
Acknowledgments		3
Abstract		4
Table of contents		5
1. Introduction		11
2. Literature Review		21
2.1	Mechanical Properties	21
2.1.1	Three Point Bending Test	22
2.1.2	Fatigue Properties	24
2.1.3	Microhardness Measurements	27
2.2	HVOF Coating Powder	30
2.3	Heat Treatment	32
2.4	HVOF Spraying Parameters	34
2.5	Coating Characterization	40
2.6	Numerical simulation	48
3. Experimental Equipment and Procedures		51
3.1	Specimen Design	52
3.2	Surface Preparation	54
3.2.1	Grit Blasting	54
3.2.2	Heat Treatment	56
3.3	HVOF Thermal Spraying Process	57
3.3.1	HVOF Coating Powder	57
3.3.2	HVOF Equipment	58
3.4	Experimental Mechanical Tests	60
3.4.1	Three Point Bending Test	62
3.4.1.1	Determination of Young's Modulus by Three Point-Bending Tests	64
3.4.2	Tensile Tests	67
3.4.3	Fatigue Tests	68
3.4.4	Vicker's indentation Test	71
3.4.4.1	Determining Young's Modulus By Indentation Test	72
3.5	Characterization Tests	76

Page

3.5.1 SEM and EDS, and Optical Microscopy 76
3.5.2 X-Ray Diffraction (XRD) 78
3.5.3 Sample Mounting 78
3.6 Finite Element Modeling 80
4. Results and Discussions 88
4.1 Three Point Bending Tests 88
4.2 Fatigue Tests 106
4.3 Tensile Tests 117
4.4 Fracture Toughness measurement 130
5. Conclusion and Future Work 136
References 143
Appendix 153

List of Tables

		Page
3.1	Chemical Composition of AMDRY 9954 Powder	57
3.2	Process Parameters of HVOF Thermal Spray Hybrid Diamond Jet ..	58
3.3	Equipment Specification for INSTRON 8801	62
3.4	Data used in calculating of Young's modulus from three-point bending tests	66
3.5	Specification of Indentation Hardness Tester	71
3.6	Data Obtained After Indenting Tests	74
3.7	X-Ray Diffraction Machine Specifications	78
4.1	EDS Analysis Results for the Coating Prior and After the Heat Treatment	109
4.2	The slope and coefficient obtained from equation 3.6 for each workpiece.....	113
4.3	Young's Modulus Obtained from Three Point Bending and Indention Tests	134

List of Figures

		Page
1.1	Schematic of the general thermal spray process	13
1.2	Key components of HVOF spray system	13
1.3	Schematic of a typical HVOF spray gun air cooled	15
1.4	Schematic of HVOF spraying gun water cooled	15
1.5	Application of HVOF coating in gas turbine component	17
1.6	HVOF applied on pump impeller	17
3.1	Three point bending, Fatigue and Tensile testing Specimen Design	53
3.2	Cutting machine used for fabricating substrate specimens.	53
3.3	Zero Pulsar grit blasting machine (BCS Company, Inc.)	55
3.4	Photograph of grit blasting chamber	55
3.5	Lindberg heat treatment furnace Model 51662	56
3.6	SEM micrographs of AMDRY 9954 used in HVOF spraying.....	57
3.7	Sulzer Metco Hybrid Diamond Jet gun controlled by FANUC Robot M-710i	59
3.8	Powder Feeder Model 1264	59
3.9	Specimens after Coating for three point bending, tensile, and fatigue tests	60
3.10	Mechanical Testing Machine (Instron 8801)	62
3.11	A photograph of three-point bending test set up	63
3.12	A photograph of workpiece after the three-point bending test	64
3.13	A schematic view of three-point bending testing and relevant dimensions	66
3.14	Indentation Hardness Tester BUEHLER®	72
3.15a	A schematic view of indention and relevant dimensions.	75
3.15b	Geometric configuration of indention mark and crack length in relation to fracture toughness measurement	75
3.16	Scanning Electron Microscope model JEOL JSM 6460 LV	77
3.17	Optical microscopy (Olympus)	77
3.18	X-Ray Diffraction machine model AXS D8 Bruker Inc	79
3.19	Automatic Mounting Press (BUEHLER® SimpliMet® 3000)	79
3.20 a	Three-dimensional view of workpiece used in the simulations three-point bending tests.....	85

		page
3.20 b	3-D view of workpiece used in the simulations of tensile test.....	85
3.21a	3-D view of the mesh used in simulations of bending tests	86
3.21b	3-D view of the mesh used in simulations of tensile tests	86
3.22a	2-D view of mesh used in the three point bending test simulations corresponds to the cross-sectional view along the x-axis.	87
3.22b	2-D close view of the mesh in the central region of the workpiece, which is used for the three point bending test simulations.	87
4.1	Load and displacement characteristics of the workpiece after three-point bend tests	90
4.2	Coating cross-section prior and after the heat treatment process	92
4.3	Coat cross-section and top view of coated surface after three-point bending tests	94
4.4	Force versus displacement behavior obtained from three point experiment and used in the FEM (ANSYS) simulations	95
4.5a	Von-Mises stress at three load conditions	97
4.5b	Contour plots of von-Mises stress at three load conditions. The stress unit is in Pa. [(a) at 120 N, (b) at 3000 N, and (c) at 4250 N].	98
4.5c	Contour plots of von-Mises stress and strain at two load conditions. [at 3000 N and at 4250 N].....	99
4.6a	Equivalent total strains at three loading conditions at coating-base material interface	101
4.6b	Contours plot of total strains at three loading conditions at coating-base material interface.....	102
4.6c	von-Mises stress along the thickness (cross-section of the workpiece) and axial location is the middle point.	105
4.7a	SEM micrograph of coating cross-section prior and after heat treatment	107
4.7b	Optical photograph and SEM micrograph of splats and oxide formation around the splats	108
4.8	XRD results obtained for heat treated and untreated coated workpieces	110
4.9	Logarithmic scale of alternating stress with number of cycles for different fatigue tested workpieces	111
4.10	Percentage of fatigue failure with alternating stress for heat treated and untreated coated workpieces	115
4.11a	SEM micrograph of cross-section of fractured coating after fatigue testing of untreated workpiece	115

		page
4.11b	SEM micrograph of cross-section of fractured coating after fatigue testing of heat treated workpiece. Delaminating of coating in the surface region is evident	116
4.11c	SEM micrograph of cross-section of fractured coating after fatigue testing of heat treated workpiece.	116
4.12	Optical photographs of fatigue tested workpieces	117
4.13	Tensile test results for as received uncoated, as received coated, heat treated uncoated and heat treated coated workpieces	119
4.14	View of fractured surfaces after the tensile tests	120
4.15	Load displacement characteristics obtained from experiment and used in FEM simulations	124
4.16	von-Mises stress along the *x*-axis (horizontal distance) at coating workpiece interface (Force = 30,400 N)	125
4.17	von-Mises stress along the *y*-axis (vertical distance) at coating workpiece interface (Force = 30,400 N)	125
4.18	von-Mises stress along the *z*-axis (distance along thickness) across the coating and workpiece (Force = 30,400 N)	126
4.19	Equivalent total strain along the z-axis (distance along thickness) across the coating and workpiece (Force = 30,400 N)	126
4.20a	Three-dimensional contour plot of von-Mises stress in the workpiece (Force = 30,400 N)	127
4.20b	Two-dimensional contour plot of von-Mises stress (at the top view of the workpiece surface) (Force = 30,400 N).	127
4.20c	Two-dimensional contour plot of von-Mises stress (at the side view of the workpiece surface) (Force = 30,400 N).	127
4.21a	Three-dimensional contour plot of equivalent total strain in the workpiece (Force = 30,400 N)	128
4.21b	Two-dimensional contour plot of equivalent total strain (at the top view of the workpiece surface) (Force = 30,400 N).....	128
4.21c	Two-dimensional contour plot of equivalent total strain (at the side view of the workpiece surface) (Force = 30,400 N).....	128
4.21d	Three-dimensional contour plot of equivalent plastic strain in the workpiece (Force = 30,400 N).....	129
4.21e	Two-dimensional contour plot of equivalent plastic strain (at the top view of the workpiece surface) (Force = 30,400 N).....	129
4.21f	Two-dimensional contour plot of equivalent plastic strain (at the side view of the workpiece surface) (Force = 30,400 N).....	129
4.22	Top and cross-sectional views of coating before and after heat treatment	131
4.23	EDS line scan across the splat and its boundary	132
4.24	SEM micrographs of cracks formed in the coating after the bending tests.	134
4.25	Indention marks on the surface of the coating prior and after heat treatment	135

Chapter 1 - Introduction

Coating of high-temperature components is required in power generating units for protecting the surface of the components from excessive heating, erosion, and corrosion during operation. Coatings must have resistance to high-temperature as well as to mechanical forces. In addition, the coating process must be effective, low cost, and fast. One of the coating methods fulfilling these conditions is High Velocity Oxy-Fuel coating (HVOF). Although the process is fast, effective, and low cost, due to the irregularities associated within the resulting coating, investigation into the process is necessary for further improvements of the coating quality. The mechanical properties of the coating, particularly at coating-base material interface, are important properties required by the coating. Consequently, the study of mechanical properties of coating-base material interface becomes essential.

Titanium alloys are used in many industries such as the aerospace, power plant, and oil industries. The combination of high toughness to mass ratio and corrosion resistance make titanium alloys the material of choice for many critical applications. Titanium alloys are used for demanding applications such as in static and rotating gas turbine engine components and in oil refinery heat exchangers. Because of its excellent corrosion resistance, titanium alloys are also used for chemical processing, desalination, valve and pump parts as well as marine equipment. In addition, high toughness to mass ratio lowers the weight of the

components produced from this alloy in the gas turbine engine. This enables to move easily the gas turbine engine to the remote areas where the electrical power is required, particularly in the Kingdom of Saudi Arabia. The most widely used titanium alloy is the Ti-6Al-4V alpha-beta alloy. However, Ti-6Al-4V alloy has relatively poor surface properties against wear and high temperature. Coating of the material becomes essential once the substrate surface is exposed to harsh environments. This coating can be achieved by the use of High Velocity Oxygen Fuel (HVOF) thermal spraying processes.

Thermal spraying refers to a group of processes in which molten or partially molten metallic or nonmetallic materials are sprayed onto a prepared substrate to form a coating. The sprayed material can originally be in the form of wire, rod, or powder. As the coating materials are fed through the spray unit, they are heated to a molten state and carried by a stream of compressed gas onto a substrate. As the particles strike the surface, they flatten and form thin platelets that adhere to the irregularities of the prepared surface [1]. Figure 1.1 illustrates a general thermal spraying process.

HVOF is one of the most common thermal spray processes which is applied to deposit coating on a substrate material to enhance its mechanical properties. The resulting coating has properties including high wear resistance, corrosion resistance, low oxide content, low stress, low porosity, and high bonding strength to the base metal [2]. In the HVOF process as shown in Figure 1.2, a blend of fuel and oxygen is injected into a torch or gun and combusted. It uses a fuel such as propylene, hydrogen, propane, or kerosene which is mixed with oxygen in a

combustion chamber. This combustion process melts a powder that is continually fed into a gun using a carrier gas and pushes it at high speeds (1,500 - 2,500 m/sec) towards the surface of the part to be coated. The combustion products flow through a nozzle and a powder feed stock is injected into the gas stream, which accelerates the powder up to 1,000 m/sec [1]. The powder partially melts in the stream and deposits upon the substrate.

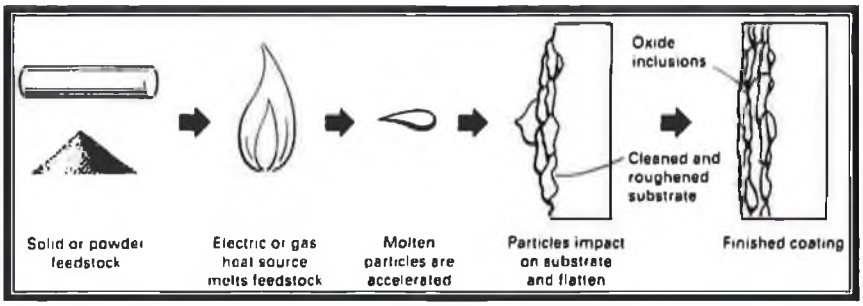

Figure 1.1 Schematic of the general thermal spray process [1]

Figure 1.2 Key components of HVOF spray system [3]

There are a number of HVOF guns on the market which use different methods to achieve high velocity spraying. Figure 1.3 shows a method that uses a system of a

high pressure combustion nozzle and air cap. Fuel and oxygen are supplied at high pressure, combustion occurs outside the nozzle but within an air cap supplied with compressed air. The compressed air pinches and accelerates the flame and acts as a coolant for the gun. Powder is fed at high pressure axially from the centre of the nozzle [4].

Another method is a high pressure water cooled combustion chamber and long nozzle as shown in Figure 1.4. Fuel and oxygen are fed into the chamber; combustion produces a hot high pressure flame which is forced down a nozzle increasing its velocity. Powder is fed axially into the combustion chamber under high pressure or fed through the side of nozzle where the pressure is lower [4].

In the aerospace field, as well as in the power generation stationary gas turbine field, HVOF thermal spray coatings are getting more and more important in the improvement of the base materials surface properties especially against corrosion, and erosion at elevated temperatures. The direct exposure to liquid, gases, and particulate solids can produce chemical corrosion or erosion of a solid surface. The high speed movement of these corrosive fluids prevents the formation of protective oxides and permits this hostile interaction of corrosion or erosion to take place [5].

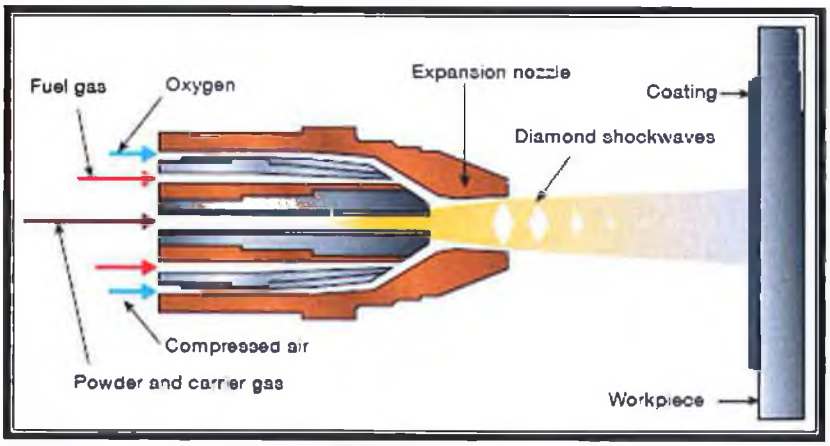

Figure 1.3 Schematic of a typical HVOF spray gun air cooled [3]

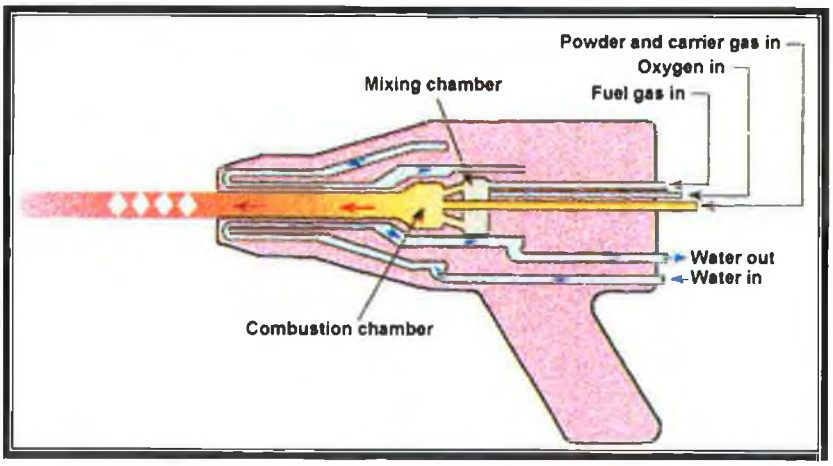

Figure 1.4 Schematic of HVOF Spraying Gun Water Cooled [6]

Gas turbine vanes for example are coated by HVOF thermal spraying process to prevent high temperature failure and extending the life span of the vanes. see Figure 1.5. The metal powder is available in many compositions; however, CoNiCrAlY is a common powder that is applied by HVOF thermal spraying process to produce the coating protecting the gas turbine hot path components from oxidation and other forms of corrosion at high temperatures [3].

Wear resistance is another major application of the HVOF thermal spraying process. HVOF permits rapid application of coating on variety of components that suffer form wear. The deterioration of surfaces due to wear is a concern in many industries. Worn components can often be repaired but this is generally very expensive. Protecting the surfaces against wear by applying HVOF thermal spray coatings can be the most economical way to offset the high costs associated with component repair or replacement [5]. In Figure 1.6, a pump impeller is coated by wear resistance powder using HVOF process to achieve erosion and abrasion resistance.

HVOF coatings are used in applications where the highest density and strength is required which is not found in most of other thermal spray processes. Many applications are using HVOF thermal spray coatings due to its features over the other thermal spray process. Coatings produced by the HVOF process have much better machinability compared with other methods. The coating is clean, hard and dense with fine homogeneous structures, and coating porosity has closely approached wrought materials [3]. HVOF systems are available with closed-loop

computer control and robotics capability and can be fully automated. The surface finishes are generally smooth and can be used in the as-sprayed condition [3].

Figure 1.5 application of HVOF coating in Gas turbine component. The coating is AMDRY 9954 and the component is in service in Saudi Aramco.

Figure 1.6 HVOF applied on to a Pump Impeller [3]

The important factors of HVOF are the high kinetic energy and high velocity that is being produced and transferred to the substrate. The thermal and kinetic energy of the high velocity particles are embedded into the substrate to form a superior coating with the following characteristics [7]:

- More uniform and high densities because of the high kinetic energy and the high turbulence experienced by particles within the combustion chamber. As the coating is high dense and less porosity, the corrosion resistance will be improved.
- Low thermal input because of the substrate temperature is less than 150 °C which ensures original mechanical properties and with no stress relieving required.
- A high particle velocity produces lower surface oxidation because the less particle exposure time compared to other thermal spraying processes.
- Lower ultimate particle temperatures compared to other processes such as plasma or arc guns as these processes operate at temperatures of 16000 °C and 6000 °C as opposed to 3000 °C in HVOF.

However, there are some disadvantages of HVOF thermal spraying process. Unfortunately the noise levels are very high reaching more than 130db [8]. Another disadvantage of the HVOF process is that the application is limited to line-of-sight areas of the part. Complex shapes, threads, and bores or holes cannot be coated [9]. High capital cost is also considered to be one of the major disadvantages of the HVOF thermal spraying process. In addition the process must be housed in a full enclosure of sufficient size.

The HVOF coating of gas turbine components is unavoidable to improve the life span of the concerned parts and to reduce the maintenance costs of such parts as well as to improve reliability. The end product quality of the HVOF coating process is assessed by the mechanical tests, which are well presented in the open literature. However, the applicability of the findings available in the open literature to the specific problems faced in the gas turbine industry is limited. This is because of the coating requirements and the base material properties, which differ than those represented in the literature.

The base materials having the high toughness to mass ratio becomes demanding in the gas turbine industry. One of the candidates is Ti-6Al-4V alloy. However, Ti-6Al-4V has relatively poor surface properties against the wear and high temperature. The surface coating provides improved properties preventing the wear and high temperature effects. Moreover, the coating performance depends on the response of the coating to the applied loads such as bending, tensile, and fatigue loads. Consequently, investigation into the mechanical properties of the coating subjected to the applied loads become necessary.

In the present thesis, HVOF coating of AMDRY 9954 ($Co_{bal}.Ni_{32}Cr_{21}Al_8Y_{0.5}$) powder on to the Ti-6Al-4V alloy surface is carried out and the metallurgical as well as mechanical properties of the coating are examined experimentally.

The rest of the thesis consists of four chapters. Chapter two is a literature review for related studies that have been carried out and reported previously. In literature, considerable research studies on HVOF coatings were presented. The literature

survey is classified according to five categories. They are mechanical properties, coating powders, heat treatment, HVOF spraying parameters, and coating characterization.

In Chapter three the experimental equipment and procedures are presented. Sample fabrication and surface preparation equipment were discussed in this chapter along with the Sulzer Metco hybrid diamond jet gun and the FANUC Robot M-710i used to produce the coatings. The equipment used for mechanical properties examinations such as INSTRON 8801 and Hardness Tester are introduced along with SEM, optical microscopy, EDS and XRD equipment that are used for microstructural characterization and surface morphology are also presented in detail. Finite element method used in the simulations is also included in this chapter.

The results and discussions are presented in Chapter four. This chapter is classified according to the mechanical tests. The mechanical tests are carried out to investigate the coating-base material interface properties. The influences of heat treatment on interface properties are also examined. Finite element method (FEM) simulating the experimental conditions is carried out to predict the stress field during the bending and tensile tests and the ANSYS FEM code is used.

Finally, the conclusion that is extracted from the present study is summarized in the Chapter five. The future work pertinent to the present study is included after the conclusions.

Chapter 2- Literature Review

Considerable research studies on HVOF coatings and mechanical properties available in literature are reviewed. The literature survey is classified according to five categories. They are mechanical properties, HVOF coating powder, heat treatment, HVOF spraying parameters, and coating characterization.

2.1 MECHANICAL PROPERTIES

The mechanical properties of the HVOF coating were examined extensively and the main emphases were to determine the Young's modulus [10 – 15], the fatigue properties [16 – 27], and the microhardness [28 – 39]. Moreover, the effects of powder characteristics [32 – 43], heat treatment [44 – 50] and, spraying parameters [51 – 69] on the mechanical properties of resulting coating were examined in details. The coating characterization in relation to the mechanical properties of the coating was also investigated [71 – 95]. Although, the HVOF coating of AMDRY 9954 was reported in the open literature [10 – 95], in general, the coating was sprayed on to the nickel based super alloys and the steel substrates in conjunction with other thermal barrier coatings. The use of AMDRY 9954 powder as coating on its own on Ti-Al-4V substrate material during the spraying process was not evident in the literature.

2.1.1 Three Point Bending Test

Three point bending tests are commonly used for fracture mechanical characterization of thermal barrier coatings. The results of the following survey indicate that the three point bending test method can be used successfully to determine the Young's modulus of the coating. The general findings from the literature shows that the Young's modules of the coating is higher than that of the substrate material, which in turn improves the mechanical response of the coating under the bending loads. However, the details of the research reported in the open literature pertinent to the three-point bending of HVOF coated workpieces are given below.

Thurn [10] showed how the fracture properties of Thermal Barrier Coating (TBC) could be determined for different crack orientations in the coating. It was recommended measuring the fracture properties parallel and perpendicular to the coating surface in case to predict failure of the coating. There are different methods used to determine the Young's modulus and fracture toughness of HVOF sprayed coating. These methods include three-point bend tests, four-point bend tests, and indentation tests. Arif and Yilbas [11] investigated three point bending of HVOF sprayed Inconel 625 coating onto mild steel workpiece. The elastic modulus and predicted the stress levels in the coating were determined. It was indicated that the high stress levels were developed in the coating region of the substrate material.

Roy et al. [12] presented an analytical model to predict MCrAlY bond coat properties of thermal barrier coatings during crack propagation induced by bending. From the results presented, it was apparent that the value of elastic module "*E*" predicted for the coatings compared well with experimental results reported in the literature. The crack propagation behavior of the coatings at room temperature for as-received and oxidized conditions showed a linear growth of the cracks on the coating until the yielding point of the super alloy was reached. At 800°C, the cracks propagated only in the coating and the ductile bond-coating offered an attractive sink for the stress relaxation.

Mechanical and thermal properties of HVOF sprayed nickel-based alloys with carbides were studied by Hamatani et al. [13]. It was indicated that the thermal shock resistance depended not only on the strength of the coating, but also on the volume concentration of splats when tested at high temperatures. Mechanical and physical properties of HVOF sprayed iron aluminide coatings were examined by Totemeier et al. [14]. The residual stresses in the coating as a function of coating thickness using curvature measurements was determined. Burkle et al. [15,34] investigated the mechanical properties of Al and Fe based coating materials deposited by Air Plasma Spraying (APS), Twin Wire Arc Spraying (TWAS), and HVOF on steel substrate using a dynamic mechanical analysis in three point bending mode. It was found that the test method was very promising for determination of static and dynamic mechanical properties of the coatings. The reduction of the Young's modulus mismatch between coating and steel substrate was found to be an important influence on the coating performance. They also

studied the mechanical properties of nano-crystalline Fe-Cr-based thermal spray coatings using nanoindentation and three point bending tests. The results showed that the Young's modulus of these coatings was 10% less than bulk material modulus for HVOF coating. Li et al. [29] showed that three and four point bend tests were appropriate for measuring the overall Young's modulus of the coatings while the indentation test was found to be strictly limited in its application due to the local phase dependent characteristics of the technique.

2.1.2 Fatigue Properties

The fatigue response of the HVOF coated workpieces are influenced by the coating properties. It is observed from the literature that, in general, the total fatigue failure of the coating is resulted prior to failure of the material. This situation is associated with the coating adherence to the substrate material and, in some cases, spalling and peeling of the coating from the substrate material are reported. The details of the literature survey in relation to the fatigue response of the coating are given below.

A new fatigue failure mode termed spalling was introduced by Ahmed [16]. Spalling was observed in thermally sprayed HVOF WC-12%Co coating and attributed to the fracture toughness of the coating. It was indicated that by appropriate control of coating thickness, and tribological conditions, it was possible to achieve a fatigue life in excess of 70 million stress cycles, without

failure. The effect of residual stress on fatigue life in HVOF carbide coatings in bending of thermal spray coated aluminum was studied by McGrann et al. [17]. It was found that the fatigue life of WC-coated specimens was directly related to the level of compressive residual stress in the coating. Moreover, in some cases, the fatigue life could be increased by a factor of 35% by increasing the compressive residual stress in the coating. It was also indicated that some other mode of failures than fatigue failure occurred, for example, failure due to spalling could occur in these components.

The thermal influence on the substrate material during thermal spraying or welding will eventually effect on the fatigue life of the substrate. The effect of microstructural characteristics on high cycle fatigue properties and fatigue crack propagation behavior of welded regions of Ti-6Al-4V were investigated by Oh, et al. [20]. The welding was processed by two different methods; they were Tungsten Inert Gas (TIG), and Electron Beam (EB) welding. They indicated that the EB welds showed the lowest fatigue strength because the pores acted as fatigue crack initiation sites.

Hernandez et al. [21] investigated the fatigue properties of 4340 steel coated with a Colomony 88 deposit by HVOF spraying process. The study was based on three different conditions, which were uncoated, grit blasted with alumina, and grit blasted with aluminum oxides coated with Colmonoy 88. The results indicated that grit blasting the base steel could lead to a significant reduction in the fatigue properties of the base material. Coating the blasted specimens, will also lead to a

further reduction in the fatigue life. Such a reduction was associated with the presence of Al_2O_3 particles, which act as stress concentrators enhancing the fatigue cracks.

Padilla et al. [22] studied fatigue properties of specimens at three different conditions (as-polished, as-grit blasted, and as-coated). It was concluded that the grit blasting significantly decreased the fatigue properties of the material for the coated specimens with HVOF deposit of NiMoAl. Moreover, it was found that the coating led to a further reduction in the fatigue strength of the material. This further reduction in fatigue strength was associated with the extensive fracture and delamination of the coating from the substrate and the possible existence of tensile residual stress in the substrate. The effect of high frequency detonation gun and HVOF thermal sprayed WC-Co coatings on the high cycle fatigue behavior of aluminum alloy was studied by Ibrahim and Berndt [23]. It was found that the HVOF sprayed workpieces exhibited significantly higher fatigue lives compared to the uncoated workpieces.

Brandt [24] investigated the effects of different spraying parameters on the fatigue resistance of HVOF Aluminum and Steel specimens. The results showed that carbide coatings produced by HVOF process with porosity levels of less than 1% behaved like a homogenous material with a fixed ductility. The high modulus of elasticity allowed a higher stiffness for aluminum constructions. It was found also that the steel or aluminum substrates with HVOF coatings exhibited the negative change in endurance limit. Fadhli et al. [25] investigated the fatigue and corrosion

behavior of stainless steel coated with Inconel-625 alloy produced by HVOF process. The results indicated that the welded coated specimens under the three different conditions exhibited a similar fatigue life as compared to the plain coated specimen. However, there was a considerable reduction in the fatigue strength of the coating when subjected to four weeks aqueous corrosion medium.

Oliveria et al. [26] studied corrosion-fatigue behavior of a quenched and tempered AISI 4340 steel uncoated and coated with Colmonoy 88 alloy by HVOF process. The results indicated that the fatigue behavior of the coated material under bending condition employing a 4 wt% NaCl solution was very similar to that in air. Effects of thermal spraying procedure and thermal fatigue on microstructure and properties of NiC-AlMoFe coating were investigated by Hidalgo et al. [27]. The results showed that the flame sprayed coatings failed catastrophically after applying thermal fatigue conditions when the maximum cycle temperature was higher than 773 K.

2.1.3 Microhardness Measurements

Indentation testing is a mechanical testing process designed to determine the properties of materials by applying a force on the indentation at the surface of a substrate material. Moreover, it is reported in the open literature that the indentation tests are used successfully to determine the fracture toughness of the coating. In general, the findings indicate that the high oxygen content in the

coating lowers the fracture toughness. The detailed literature survey is given below.

Ahmed [16] measured the microhardness of thermally sprayed coatings on steel substrate rolling element cones. He found that the indentation fracture toughness of coatings was improved using HVOF compared to Air Plasma Spray (APS) thermally process. MA et al. [18] evaluated the elastic stiffness of NiCoCrAlY coating produced by plasma sprayed process. The low porosity NiCoCrAlY produced by vacuum plasma spraying has the highest Youngs' modulus and density compared to the air plasma spraying process (100-140 GPa). Fracture toughness of HVOF coatings was examined by Palo et al. [28]. The Vicker's indentation tests was used to quantify the in-plane fracture behavior of coatings and it was found that the fracture properties of coating were anisotropic. It was indicated that Vicker's indentation method was a useful and a convenient technique for fracture toughness measurement of coating.

Otsubo et al. [30] used a Vickers microhardness tester to investigated the hardness of Cr_3C_2NiCr cermet coatings sprayed onto a mild steel substrate by plasma and HVOF spraying processes. The hardness of the HVOF coating was higher than that of the plasma coating because the latter contained more unmelted Cr_3C_2 carbide particles. The hardness measured under a large load exhibited lower values as compared to that measured under a small load because of cracks generated due to the indentation load. Dent et al. [31] studied nickel-based alloy coatings that was

produced by HVOF spraying and found that the microhardness increased from 600 to 750 HV as the amorphous content of the coatings increased.

He et al. [32] predicted the microhardness of HVOF sprayed coatings using a simple method employing a mixture equation for the case of a low-volume fraction of unmelted particles. However, for the condition of a high-volume fraction of unmelted particles, the microhardness measured is much lower than the calculated ones, which was most likely due to the presence of porosity and voids formed in between the unmelted particles which were not accounted for in their equation. Horlock et al. [33] investigated the microstructure and abrasive wear behavior of HVOF sprayed Ni (Cr)-TiB_2 coatings. The coating was found to have a mean Vickers microhardness value of 8.6 GPa using 3 N load. The knoop microhardness depended on the indenter orientation and varied from 8.9 to 10 GPa with the long axis of the indenter parallel to and perpendicular to the coating substrate interface, respectively.

It was observed by Gil et al. [35] that an increase in spraying distance of HVOF increased the porosity and decreased the microhardness of the coatings. This accrued due to the fact that the number of unmelted particles was also increased. The unmelted particles could be identified by both their shape and morphology. Ahmaniemi et al. [39] also proved that the microhardness increases as the porosity decreased in thermal barrier coatings. Liu et al. [36] investigated the mechanical properties, microstructure, and tribological performance of HVOF deposited WC-18 coating. The results showed that the hardness of the coatings increased with the

temperature of the particle after the deposition. Coating deposited with propylene fuel gas had higher hardness than coatings produced with hydrogen fuel. The results also showed that the sliding wear resistance increased linearly with the hardness however it was decreased when the microstructure exhibited the presence of cracks at splat interfaces. Abrasion wear showed the same dependence on the hardness for the sliding wear situation.

Oliver and Pharr [37] investigated the effect of HVOF thermal spray conditions on the hardness Cr_3C_2-NiCr coatings. The results showed that the coating hardness increased with an increase in propane flow. However, the influence of oxygen flow on coating hardness was not significant. The influence of fuel/oxygen ratio in HVOF spraying on the deposition of Cr_3C_2 coatings was investigated by Kim et al. [38]. The microhardness of as-sprayed coatings ranged from 1099 to 1140 HV with fuel/oxygen ratio (3.2, 3.0, and 2.8) used during the spraying process. After heat treatment at 1000°C, the hardness was increased up to 1660 HV due to the formation of Cr_2O_3 and densification of the coating layer during the heat treatment.

2.2 HVOF Coating Powder

The splat (particle) size, oxygen content, and molten state of the powder are found to have a significant effect on the mechanical properties of the coating. The semi-molten state and high oxygen content with large size splats (in the coating) reduce

the mechanical properties of the coating such as tensile strength and fatigue life. The details of the findings in the open literature are given below.

He et al. [32] investigated the particle melting behavior during HVOF using Inconel 625 powders. The results indicated that the volume fraction of unmelted particles in the coating was dependent on the proportion of powder within a specified size range which was 30 to 50 μm in the experiment. It was found that the particle temperature significantly decreased as particle size increased. The large particles did not melt during the spraying process because the maximum temperature the large particles experienced was just over their melting temperature. Li et al. [40] studied the effect of sprayed powder particle size on the oxidation behavior of MCrAlY powders during HVOF deposition. The results showed that the oxygen contents in the collected powder and coatings depended on the particle size. With decreasing particle size the oxygen content in the collected powder increased exponentially. The oxygen content inside the coating was approximately equal to that in the collected powders for the mean particle size of <50 μm. For large particles >50 μm there was a clear difference in the oxygen contents inside the coating and in the collected powders. This difference was attributed to the post impact oxidation of a splat.

Nuutinan et al. [41] compared the microstructural of HVOF and Vacuum Plasma Spraying (VPS) sprayed MCrAlY coatings. The results showed that the selection of appropriate particle size of the spray powder had marked importance in the HVOF process. Presence of fine powder particles produced oxides in the coatings

and caused clogging of the nozzle in the HVOF gun. It was found also that the coating structure remained unchanged after the heat treatment.

Two NiAl intermetallic powders which had been reaction sintered and inert gas atomized were investigated by Hearley et al. [42] to study the effect of spray parameters on the HVOF coating process. They found that the gas mixing ratio and powder size were critical in determining the coating properties. A spherical inert gas atomized powder with a narrow particle size range between 15–45 μm and small percentage of particles >50 μm were the preferred for spraying at high oxygen to fuel ratio. The experimental investigation to evaluate coating crack resistance in bending, low cycle fatigue was carried out by Pejryd et al. [43]. The results showed that a strong correlation existed between the coating performance and residual stress in coating.

2.3 Heat Treatment

Heat treatment improves the residual state of the coated workpieces via stress relaxation. However, the miss-matching of the elastic modulus of the coating and the substrate material deteriorates the interfacial properties of the coating. It is reported in the open literature that this situation is commonly observed and the stress developed due to miss-matching at the coating-substrate interface lowers the coating adherence to the substrate material. This, in turn, results in negative effect

on the mechanical properties of the coating. However, in some cases, this affect is not observed and the change in the mechanical properties is not noted. The details of the literature survey are given below in this regard.

Poza et al. [19] studied the microstructure of vacuum plasma sprayed CoNiCrAlY coating on Ni-base superally after heat treatment and isothermal oxidation. The solidification of the coating droplets took place at different cooling rates during deposition and led to an inhomogenous microstructure. Diffusion from the substrate and within the coating took place during heat treatment and as a consequence, the coating adherence was improved and the grain coarsened led to a more homogenous in microstructure. Li et al. [44] studied the properties of heat treated calcium phosphate coatings deposited by HVOF spray. It was found that on annealing heat treatment at 750°C was beneficial for the improvement of adhesive and shear strengths as well as fracture toughness.

The effect of heat treatment on characteristics of HVOF coatings was studied by Okada [45]. The tensile strength of coating was increased after heat treatment due to the low surface void ratio resulting from the heat treatment. Natalia-Sora et al. [47] studied the structural changes of Cr_3C_2/NiCr coating while varying the annealing temperature in the range of 300−1073 K. The results showed that the annealing treatments caused an enhancement of the oxide contents and the crystallite size as well.

Stewart et al. [48] analyzed the microstructure of WC-17 wt% Co powder that was sprayed by HVOF and found that the heat treatment above 600°C led to significant microstructure changes within the coatings. However, heat treatment at all temperatures resulted in changes in the integrity and residual stress state of the coating due to thermal expansion coefficient mismatch between the coating and substrate. Hamashima et al. [49] examined HVOF sprayed Mo-Ni-B ternary borides and Ni-Mo alloy powders. It was found that the bonding strength of this layer was relatively high and heat treatment could further enhance the bonding strength. Eskner [50] studied the mechanical and fracture behavior of a NiAl coating produced by a pack cementation process and plasma spraying. It was found that the heat treatment led to a rapid internal and external oxidation which led also to an increase in the elastic modulus.

2.4 HVOF Spraying Parameters

HVOF spraying parameters influence the resulting coating structure and the mechanical properties of the coating. The findings from the open literature show that the spraying parameters, such as stand-off distance, feed rate, jet temperature, and the powder speed, have significant effect on the coating structural integrity, splat size, voids distribution, porosity, and oxygen content in the coating. The detailed literature survey in relation to the spraying parameters are given below.

The influence of thermal process selection and corresponding bond-coat surface roughness on thermal barrier coating performance was investigated by Knight et al. [51]. The bond coat CoNiCrAlY deposited by Low Pressure Plasma Spry (LPPS), Shrouded Air Plasma Spray (SPS), and HVOF and found that the surface roughness had significant effect on the coating adhesive strength. The effect of off-angle spraying on the structure and properties of HVOF WC/CoCr coatings was studied by Strock et al. [52]. It was found that coatings sprayed at 90° exhibited the highest microhardness and compressive residual stress which is considered favorable for good wear response.

Chang et al. [53] presented a numerical simulation of the HVOF spraying process. The results showed that the transient solution using the stochastic particle model provided important insights into the statistical variations in particle temperature, velocity, and degree of melting. Knotek et al. [54] used numerical simulation to study the influences of HVOF spraying parameters on coating properties. The calculated velocities for WC-Co coating was compared for different distances with measured velocities. The impact of particles and resulting coating formation process have been modeled. It was found that the results of the numerical modeling of the HVOF process were consistent with the experimental results.

Tuurna et al. [55] studied the microstructure of CoNiCrAlY (Co-based powder) and NiCoCrAlY (Ni-based powder) coatings produced by HVOF spraying. It was found that the oxygen flow and spray distance could influence the mechanical

properties of the coating. The coating thickness and surface roughness decreased as the oxygen flow increased. It was also shown that increasing spraying distance slightly would increase the coating thickness and decrease the surface roughness. In the case of NiCoCrAlY coating, the coating thickness increased as the oxygen flow rate is increased while surface roughness decreased at the same time. The results showed also that it is possible to produce MCrAlY coatings using the HVOF process followed by heat treatment. by comparing the HVOF and vacuum plasma spraying process (VPS), it was fond that the microstructure of HVOF sprayed coating with optimized spraying parameters to be similar to the corresponding VPS sprayed coating.

The sliding wear behavior of plasma sprayed coatings deposited using different pressure conditions was examined by Staia et al. [56]. The highest sliding wear resistance was obtained for samples processed at a pressure of 1200 mbar, a spraying distance of 120 mm and substrate temperature of 600°C. An increase in spraying distance from 120 to 140 mm while keeping all other parameters constant produced an increase in the wear volume of 33%. However, cooling the substrate resulted in increased wear by volume of 112%. Zhao et al. [57] investigated the influence of the spray parameters on the oxidation of coatings during spraying of NiCoCrAlY and intermetallic NiAl-TaCr using the HVOF process. It was found that both the Oxygen to Hydrogen fuel ratio and spray distance could significantly influence the oxygen content of the coatings. The microstructures of the coatings were studied in as-sprayed as well as heat-treated conditions. The as-sprayed

NiCoCrAlY coating showed a homogeneous two-phase structure than heat-treated coatings.

Lugscheider et al. [58] studied the influences of HVOF process parameters on the microstructure and oxygen content of MCrAlY coatings. The major parameters were subjected to estimate both single and inter-acting effects. It was found that spray distance, fuel/oxygen ratio, and powder feed rate exert a major influence on microstructure and oxygen contents whereas powder feed gas rate did not have a significant effect. Hamatani et al. [59] investigated the optimization of electron beam remelting process parameters of HVOF sprayed alloys and carbides. It was found that not only electron beam conditions, but also the thickness of substrate and plate affected the penetration depth and the remelted width at the interfaces between the Ni plate and coating. The results showed that in order to reduce the number of pores and uneven surface morphology, low fusing speed and homogeneous heating were preferable.

The influence of the spray velocity on arc-sprayed coating structures was investigated by Steffens et al. [60]. It was found that the influence of spray velocity on the coating structure was mainly on the coating porosity. Moreover, increasing surface velocity reduced the self-densifying process of the impacting particles. Chromium steel required a surface velocity in the range between 35 to 40 m/min for optimum porosity because of low heat conductivity. However, slow surface velocity (5 m/min) provided dense NiCr coatings because of higher heat conductivity.

Dobler et al. [61] assessed and characterized various spray parameters for the JP-5000 and DJ hybrid system. The results revealed that coating oxygen contents of less than 1 wt% could be more easily attained with the JP-5000 whereas tighten control of parameters is required for DJ hybrid system. It was found also that the low particle temperatures necessary for low-oxygen content coatings might impair bond and cohesive strength. The effects of process parameters on molten particle speed and surface temperature and the properties of HVOF chromium-carbide/nickel-chrome coatings were investigated by Lih et al. [62]. The results showed that the major control factors affecting the particle surface temperature were powder feed rate, stand-off distance, and gun barrel length. The porosity content of coatings deposited by molten particles heated to a range of 1650°C–1725°C showed relatively lower porosity content. Coatings deposited by higher particle speed exhibited relatively better abrasion wear resistance and that a weak dependence existed between particle speed and coating wear.

Edris et al. [64] studied the HVOF spraying process to deposit coatings of Inconel 625 onto mild steel substrates and the structure of the sprayed coatings were related to the processing conditions employed. Three processing variables were examined, namely oxygen to fuel gas ratio, total gas flow rate in the gun and combustion chamber length. All were found to significantly influence the oxide contents of coatings as measured by XRD methods. Higuera et al. [65] studied the effects of thermal spraying and thermal fatigue on microstructure and properties of NiCrAlMoFe coating. It was found that the oxide content depended on both the

maximum temperature attained and the interaction time between the powders and the air during the in flight time. Porosity was also related to the spraying procedure in terms of the average temperature and velocity attained by the particles when they impacted on the cold substrate surface.

Johi et al. [66] investigated the particle behavior during the HVOF spraying process using a comprehensive prediction model which allowed realistic estimation of the temperature and velocity of a particle transversing through the oxygen/ fuel combustion flame. The results showed that the nature of the powder material had a considerable influence on particle heat-up and acceleration during the spraying process. A theoretical model was used by Ait-Messaoudene et al. [67] to evaluate the velocity and temperature of a spherical particle during its flight in a HVOF thermal spraying system. the coupled momentum and energy equations governing the particle movement were solved as independent variables after considering the gas velocity and temperature.

Sturgeon [68] investigated the high-velocity oxygen-fuel spraying processes. The results showed that it could produce coatings of low porosity and low oxidation level when process parameters were controlled properly. It was shown also that under optimum spraying conditions the adhesion to the substrates was excellent with bond strength of over 70 MPa for WC-Co coating. Li et al. [69] investigated the effect of spray conditions on the properties of HVOF Cr_3C_2-NiCr coatings. The results showed that the properties of the coatings were greatly influenced by oxygen and propane gas flow.

Kim et al. [38] investigated the influence of fuel/oxygen ratio in HVOF spraying on the deposition of Cr_3C_2 coatings. The results showed that the porosity of the coating was the lowest at fuel to oxygen ratio equals to three and linearly decreased with increasing heat treating temperature. Reduction of the porosity was due to densification of the coating resulting form a sintering effect by heat treatment. Fadhli [5] investigated the performance of HVOF thermal spray coating using Inconel-625 powder. The influence of various powders feed rates and spraying distance was examined. It was found that high powder feed rate was associated with increased porosity content and lowered coating hardness. Moreover, coatings produced at long spraying distance for a given feed rate exhibited high oxidation content and low hardness.

2.5 Coating Characterization

Coating characterization is an essential element for measuring the coating properties. The proper knowledge on the coating characteristics is the key issue for successful assessment of the mechanical properties of the coating. The assessment techniques reported in the open literature include the analytical tools and methods such as microscopic examination, compound analysis, and elemental distribution in the coating. These tools and methods are extensively reported in the open

literature. The details of the literature survey associated with the coating characterization are given below.

The effects of surface oxidation during HVOF coating process were studied by Tang et al. [71]. It was found that the surface oxide that formed on a CoNiCrAlY coating during HVOF process could significantly affect its subsequent mechanical behavior. The oxidation behavior of MCrAlY HVOF coating due to different particle sizes was examined by Li et al. [40]. It was indicated that when large particles were used, oxidation of particles in flight prior to impacting to substrate surface had a significant effect on the oxygen content in the coating. Microstructure analysis of HVOF coating deposited onto steel was investigated by Edris et al. [64]. The oxide contents of coatings were measured using X-Ray diffraction method.

Zhangxiong et al. [73] explored the effect of bond coat processes and surface characteristics on the failure mechanism of thermal barrier coatings which consisted of ZrO_2-8Y2O_3 and CoNiCrAlY which were deposited using low pressure plasma spray and HVOF. Results showed that deposition process and surface characteristics had significant effects on the thermal cycling lifetime and failure mechanism. In general all the coatings were dense with porosity under 1%, and the coating deposited by the LPPS process possessed the lowest porosity. TBC with shrouded air plasma SAPS coatings exhibited the worst thermal cycling lifetimes. In the failure due to thermal cycling the coating surface roughness had a

significant effect on the crack propagation. Some degree of surface roughness between Ra=70 and Ra=47 was clearly desirable in order to produce TBC with long lifetimes. Microstructural analysis of two types of coating was carried out by Neville et al. [74]. It was indicated that HVOF coating was susceptible to corrosion and laminated structure of coating was resulted. Itoh et al. [75] examined the characteristics of MCrAlY coatings sprayed by HVOF system. The results showed that the residual stress of HVOF coating was reduced by the shot-peening effect comparable to that of a plasma spray system in open air. Teratani, et al. [76] studied the reaction diffusion behavior of thermally sprayed MCrAlY coatings on Ni-based super alloys. It was found that CoNiCrAlY coating by Atmospheric Plasma Spray (APS) inhibited the reaction diffusion at the interface of the coating and the base material. It was also confirmed that the protective dense layer of aluminum oxide, against hot corrosion, was formed in the surface of CoNiCrAlY coatings.

Schmitt et al. [78] compared thermal barrier coatings produced with low pressure plasma spraying and HVOF in terms of their porosity, roughness, and oxidation behavior. The porosity was proportional to the roughness of the HVOF coatings. HVOF CoNiCrAlY coating showed oxidation behavior similar to coatings produced by LPPS. The influence of the thermal spraying process (Air Plasma Spraying APS, HVOF, and Vacuum Plasma Spraying VPS) on the microstructure and mechanical properties of copper coating was examined by Gassot et al. [79]. It was found that the VPS copper coating had a crystallographic structure and its mechanical properties were very close to bulk copper, whereas APS and HVOF

copper coatings had splat morphology and their mechanical properties were different from bulk copper.

Tang et al. [80] investigated the effect of surface oxidation during HVOF processing on the oxidation behavior of cryomilled CoNiCrAlY coating. It was found that the oxide scales that formed on the as-sprayed and polished coatings after 1 and 24 hours oxidation were different, i.e. while pure alumina scale formed on the polished coating, a scale of spinal type oxide formed on the as sprayed coatings. Gray et al. [81] determined the critical oxide thickness required to initiate spallation from a low-pressure plasma spray CoNiCrAlY overlay coating during cooling from 1100°C to room temperature. The results showed that the thickness of oxide layer varied in between 2.5 to 3.2 μm. Sobolev et al. [82] studied the heat transfer process during formation of HVOF sprayed WC-Co coatings on smooth and grit blasted copper substrates. The results showed that the substrate coating adhesion and the development of the coating can be predicted.

Wang et al. [83] investigated the microstructure and density of the NiCrAlY coatings at different stages including diffused, plastic deformed, and aged after the shot peening plastic deformation. The results showed that both increment of density and precipitation of NiAl phase during aging treatment for shot peening coating NiCrAlY resulted in the improvement of resistance to oxidation at elevated temperature. It was found also that the shot peening technology improved the microstructure and physical properties of the coatings.

Scrivani et al. [84, 85] compared three coating processes (HVOF, Vacuum plasma Spraying (VPS), Axial plasma spraying AXPS) for the deposition of CoNiCrAlY. It was found that VPS process produced very dense and oxide-free coatings. However AXPS showed a considerably better efficiency than other methods in terms of fraction of powder used. HVOF produced low porosity coating but the oxide content was high as compared to VPS. The characterization of NiAl and WC/Mo coatings deposited by HVOF process was also investigated. It was found that WC-CoCr carbide coatings had high erosion resistance due to their high microhardness. WC/Mo showed also good resistance to an erosive environment because of its carbide content. It was recommended replacing Inconel 625 coating with WC/Mo compound coating in petrochemical environment for corrosion resistance.

Tang et al. [80] investigated the influence of grain size on the oxidation behavior of two HVOF sprayed CoNiCrAlY coatings made from cryomilled powder and commercially available gas atomized powder. The samples were exposed to air at 1000°C for 1, 24, and 330 hours. The results indicated that while a fine grain microstructure could promote the formation of a pure alumina layer on the coating by increasing the Al diffusion rate toward the surface, it could also accelerate the Al depletion by increasing the Al diffusion rate toward the substrate, which resulted in the formation of non-alumina oxides after long-term oxidation. Schwtzke et al. [86] studied the phase transformations of two different powders, WC-Co and WC-CoCr. The results showed that the powder exhibited various

degrees of phase transformation depending on type of powder, spraying system, and spraying parameters.

Mohanty et al. [87] investigated the effects of wear test variables on HVOF sprayed Cr_3C_2/NiCr coatings using a pin-on-disk tribometer. Room temperature sliding friction and wear behavior of coatings were discussed with respect to load, relative velocity, and counter-body material. It was found that the tribological behavior of HVOF sprayed Cr_3C_2/NiCr coating was significantly affected by its microstructural constituents, such as splats, porosity and dispersion of second phases formed. It was also shown that changes in imposed sliding wear test conditions varied the friction and wear behavior of thermally sprayed coating considerably.

Sobolev et al. [88] developed a mathematical modeling of coating structure and adhesion during high-velocity oxygen-fuel (HVOF) spraying of WC-Co powder on a copper substrate. The results showed that during formation of coating some structural changes in the substrate material occurred because of heating and rapid cooling. It was also found that mechanical and thermal interactions of the substrate coating significantly influence the development of the coating adhesion during thermal spraying. Lau et al. [89] described a mathematical model predicting the particle behavior of nanocrystalline Ni powder during HVOF spraying. The equations described the momentum and energy transport between the impinging particles and the gas flow with a modified geometric ratio were used to account for the size and morphological effects at nanometric agglomerates. Particle velocities

and temperatures as estimated by numerical calculations showed that fractions of nanoparticles agglomerates did not melt during the HVOF spraying process in agreement with the experimental results.

The performance of Inconel alloy 617 in actual and simulated gas turbine environments was investigated by Ganesan et al. [90]. The results showed that the outstanding oxidation and carburization resistance as well as thermal stability of alloy 617 was superior to other alloys, such as INCO® alloy HX, Haynes alloys HS188®, 214®, and 230®. Rairden et al. [91] explored the metallurgical characteristics of several alloy combinations prepared by low-pressure plasma spraying. It was demonstrated that several nickel and copper-based alloys could be deposited onto oxygen free high conductivity copper OFHC and Inconel 718 substrates with almost oxide-free coatings and nearly 100% dense.

Neville at el. [74] studied two types of thermal sprayed cermet coatings applied to a super duplex stainless steel substrate. Both coatings (86WC-10Co-4Cr and 50WC-50Ni-Cr-B-Si) were applied using a HVOF process. It was found that the HVOF coated specimens possessed good adhesion to the substrate, no gross porosity, and only minor occurrence of defects. Sakakibara, et al. [92] studied the shielding controlled plasma spraying process. As the oxygen concentration in the shielding nozzle was maintained as low as 0.5%, the metal oxide contents volume of CoNiCrAlY coating and the porosity of the coating reduced to 0.2% and 0.3% respectively under optimal spray particle size.

Tuominen et al. [72] studied laser remelting of sprayed coatings to overcome the drawbacks of sprayed structure and to improve the coating properties. The coating material was Inconel 625 which contained chromium and molybdenum as the main alloying agents. The coating was sprayed by HVOF spraying onto a mild steel substrate. The tests performed in the study showed that the resistance of the coating to corrosion and high temperature oxidation was still inferior compared to the corresponding bulk material despite the use of one of the most advanced HVOF processes. Pores were found in some of the remelted samples. Yilbas et al. [93] studied the HVOF coating process. It was shown that the powder sprayed impacted onto the substrate where forming a mechanical coating across the coating layer. Moreover on inhomogeneous structure across the coating layer was observed.

Khalid et al, [94] examined the effect of internal defect structures on the growth morphology of oxidation in Inconel 625 coating, which was exposed at different temperatures in CO_2. The results showed that the changing of the topography of oxide formed in deformed and undeformed specimens. The porous oxide surface was evident in both specimens. the presence of fine geometrical shaped particles in the deformed specimen as compared to the undeformed specimen might be associated with the formation of complex spinals in the undeformed specimen. The deformed specimen had abnormal grain sizes as compared to the undeformed specimen that showed coarse grain sized structure. Singheiser et al. [95] described the thermal barrier coating microstructure and mechanical properties for MCrAlY coatings. The stress strain behavior of air plasma sprayed coatings showed typical pore size distribution for porous and dense air plasma spraying by measuring

mercury immersion testing. Using this technique, pores below 0.5μm can be measured. These small pores cannot be seen by optical microscopy but make a significant contribution to the overall porosity.

2.6 Numerical Simulation

The numerical simulation studies on coating and substrate material subjected to the mechanical forces were carried out in the open literature [77, 97-99, 103]. In the simulations, mainly the Finite Element Method (FEM) is used to predict the strain and stress levels in the coating system. However, the predictions provided useful qualitative information on the strain stress states of the coating other than AMDRY 9954 and the base material other than Ti-6Al-4V alloy when subjected to the mechanical loading.

In this regard, Panov et al. [77] developed a physically based model with accommodating the material parameters, which are capable of capturing the tensile failure in aluminum alloys. It was demonstrated from the predictions of the numerical analysis that the model developed could predict the tensile damage and failure through the spalling. Kawashita et al. [97] modeled the tensile stress-strain behavior of the mandrel peel arm for measurement of the adhesion fracture toughness of epoxy metal laminate. It was indicated that the tensile stress-strain behavior was not easily described by bilinear or power low function. Tang el al. [98] considered the finite element analysis of a strain hardening layered structure

under the normal loading by a rigid and a deformable indenter. The finite element method (FEM) was used to investigate the normal indentation problem of a deformable indenter in contact with a strain hardening substrate coated with an elastic–perfectly plastic layer. It was shown that the use of a strain hardening substrate alleviated the maximum radial tensile stress just out side the coating edge.

The influence of bi-modal and lamellar microstructures on the behaviour of small cracks emanating from notches in $\alpha + \beta$ titanium Ti-6Al-4V alloy was evaluated by Benedetti and Fortanari [99]. The stress distribution was assessed by finite element modeling of test using ANSYS numerical code. The importance of the bi-modal and lamellar microstructures on the material damage was highlighted. Moreover, the influence of the finite element mesh size on the structural stress value determined by a linear extrapolation method was analyzed by Matic and Domazet [103]. The possibility of using existing design S–N curves for cases of bending induced by a force on the welded stiffener was examined. It was demonstrated that the smallest possible number of element layers should be used for modeling the thicker plates when they cannot be modeled with a single layer, but with an increased number of elements in front of the weld toe.

Summary of Literature Survey

In literature, considerable research studies have been performed on HVOF coatings but the information provided was limited to specific applications. In the gas turbine industry, Ti-6Al-4V alloy is used for specific components (hot path components) due to its high toughness to mass ratio. The available literature show that much research has been reported with various types of HVOF deposited coatings on Ni base substrates. These coatings in general have been used as thermal barrier coatings. There are evidences that HVOF deposited AMDRY 9954 have also been used as a protective coating on Ni-based alloy substrate. However, in these cases AMDRY 9954 was used as a secondary coating to provide corrosion protection. To the author's knowledge, there has no been any work reported in which AMDRY 9954 has been used as a thermal barrier coating on its own specifically, on Ti-based alloys. Since the information presented in the open literature do not cover the details of the specific properties of the AMDRY 9954 coating on Ti-6Al-4V alloy, which is produced by HVOF, the present study is carried out to examine the mechanical properties of such coating in detail in relation to the practical applications in the gas turbine industry. The literature survey is classified according to five categories. They are mechanical properties, coating powders, heat treatment, HVOF spraying parameters, coating characterization, and numerical simulation.

Chapter 3- Experimental Equipment & Procedures

Experiments are carried out to examine metallurgical and mechanical properties of HVOF thermally sprayed AMDRY 9954 coatings on Ti-6AI-4V alloy. The experiments carried out include sample preparation, HVOF coating, heat treatment, three point bending test, tensile test, fatigue test, and microhardness test.

The mechanical tests are applied on as received uncoated heat treated and un-heat treated Ti-6Al-4V alloy substrate specimens as well as coated heat treated and un-heat treated specimens. Three-point bending tests are carried out to investigate the coating-base material interface properties and the influence of heat treatment on interface properties as well. In the tensile test, the strain caused by the applied load to the specimen is plotted to evaluate the adhesion of the thermally sprayed coating to the substrate. Fatigue tests are conducted to study the fatigue resistance behavior of the substrate martial after coating under fluctuating load. The microhardness test is carried out to measure the hardness and estimate the plane fracture toughness of the coating. The microstructural characterization and surface morphology prior and after mechanical testing are carried out using SEM and optical microscopy while EDS and XRD are carried out for metallurgical examinations.

3.1 SPECIMEN DESIGN

Ti-6AI-4V alloy is selected due to its excellent tensile and fatigue strength and corrosion resistance and high toughness to mass ratio and as it is widely used in gas turbines. The substrate workpieces are titanium alloy Ti-6AI-4V which prepared in accordance with the ASTM D790 (flexural properties) [106] and ASTM E-466 standard (axial fatigue test of metallic materials) [108].

The plain workpieces are of the geometry of continuous radius between ends to be used for tensile and fatigue tests and rectangular bar to be used for three point bending test as shown in Figure 3.1. The cutting machine (Shaanxi Haven Equipment & Trading Co., Ltd.) [96] as shown in Figure 3.2 was used to fabricate the specimens as the substrate that was received initially in a flat plate with one meter square.

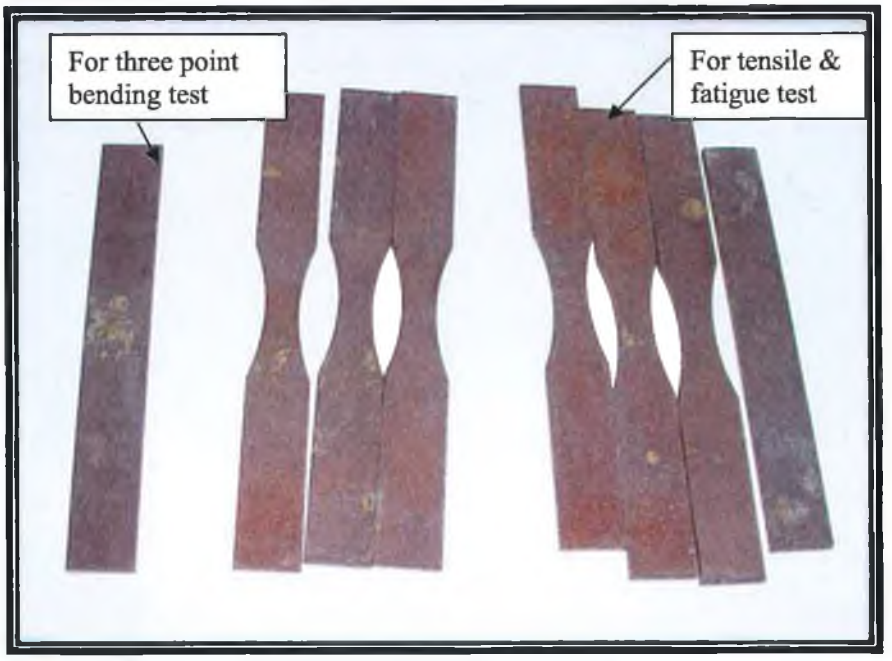

Figure 3.1 Three point bending, Fatigue and Tensile testing Specimen prior to coating

Figure 3.2 Cutting machine used for fabricating substrate specimens. [96]

3.2 SURFACE PREPARATION

3.2.1 Grit Blasting

Grit blasting is the most frequently used surface preparation procedure. The roughening cleans the surface of contamination that may inhibit bonding and creates an irregular profile of minute surface irregularities. This enhances the adhesion of the coating. The substrate specimens were grit blasted with 80 mesh Al_2O_3 particles at 620 kPa to roughen the surface and then cleaned by compressed air prior to HVOF thermal spraying. As shown in Figure 3.3 and 3.4, the grit blasting process was performed by Zero Pulsar grit blasting machine manufactured by BCS Company, Inc. of Thompson, CT, USA.

Figure 3.3 Zero Pulsar grit blasting machine

Figure 3.4 Photograph of grit blasting chamber

3.2.2 Heat Treatment

In order to resemble the harsh environments and investigate the effect of the oxidation on the mechanical properties of coatings, coated workpieces were heat treated at annealing temperature. The heat treatment of workpieces was carried out at 735 °C for one hour in argon ambient. Since the combusted gas leaving the combustor of the gas turbine consists CO_2, CO, H_2O, N_2, and NO_x , it is difficult to accommodate the same constitutes of the gases in the furnace during the annealing treatment. Consequently, argon is selected (as an inert gas) as the heat treatment ambient. Annealing heat treatment process is applied to the Ti-6Al-4V to increase its fracture toughness and ductility and improves dimensional stability and creep resistance. A Lindberg Model 51662 high temperature furnace was used during the heat treatment process as shown in Figure 3.5. The natural cooling of workpieces from the heat treatment temperature to room temperature was accommodated in the furnace.

Figure 3.5 Lindberg heat treatment furnace Model 51662

3.3 HVOF THERMAL SPRAYING PROCESS

3.3.1 HVOF Coating Powder

Sulzer Metco AMDRY 9954 powder was applied as coating on a flat titanium super alloy (Ti-6AI-4V) substrate. The Metco powder (CoNiCrAlY) is a cobalt-nickel based alloy with particle size between 20-35 μm with spherical morphology with some small and local satellite attachments to the main body of the powder as in Figure 3.6. AMDRY 9954 powder is used for protective coatings in hot corrosive or oxidizing environments up to approximately 850°C. The powder has excellent high temperature oxidation and corrosion properties [105].

Table 3.1 Chemical composition of AMDRY 9954 powder (wt %)

Powder material	Chemical composition				
AMDRY 9954	Co	Ni	Cr	Al	Yt
	Bal.	32	21	8	0.5

Figure 3.6 – SEM micrographs of AMDRY 9954 powders used in HVOF spraying.

3.3.2 HVOF Equipment

Sulzer Metco HVOF hybrid diamond jet has controlled by a FANUC Robot M-710i was used to produce premium quality hard, dense coatings exhibiting high adhesion to the substrate (Figure3.7).

The HVOF spray system used for this study consisted of powder feeder, control unit, gas cylinders, spray gun, and water pump. The system is operated with propane as fuel gas and water is used as a coolant. Fuel and oxygen (O_2) are adjusted in the control unit to produce the required combustion reaction with the specified temperature. Powder is injected into the gun using Praxair Model 1264 powder feeder as shown in Figure 3.8. Nitrogen is used as the powder carrier gas to transport the powder from the feeder to the gun. The spraying properties are given in Table 3.2. The effects of spraying parameters on the coating characteristics were carried out previously [5, 51-69] and in the light of the previous studies, the optimum coating conditions were assessed through the oxygen content, microstructure of coating.

Table 3.2 Process parameters of HVOF thermal spray Hybrid Diamond Jet as spraying practice for Saudi Aramco.

Oxygen Pressure (kPa)	Fuel Pressure (kPa)	Air Pressure (kPa)	Powder Feed Rate (m^3/h)	Spray Rate (Kg/h)	Spray Distance (m)
1023	590	720	0.85	6.5	0.31

Figure 3.7 Sulzer Metco Hybrid Diamond Jet gun controlled by FANUC Robot M-710i

Figure 3.8 Powder Feeder Model 1264

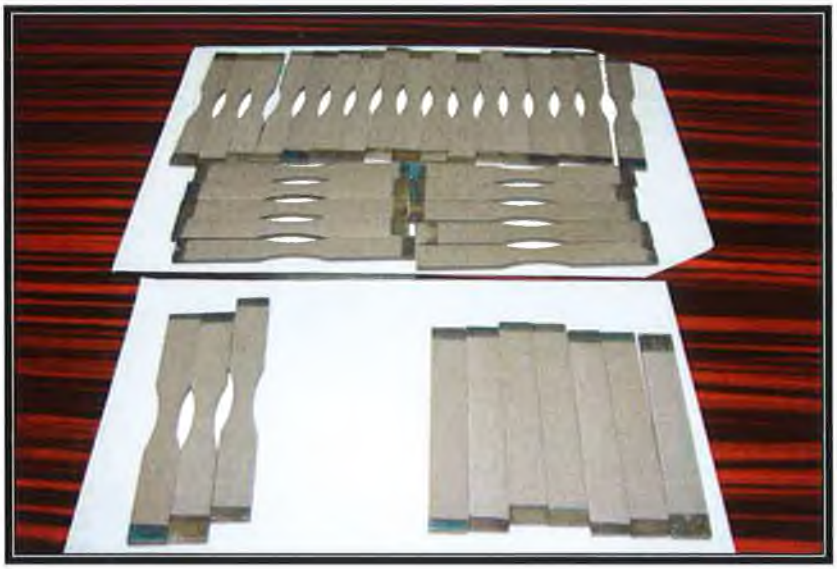

Figure 3.9 Specimens after Coating for three point bending, tensile, and fatigue tests.

3.4 EXPERIMENTAL MECHANICAL TESTS

The mechanical properties of coated Ti-6AI-4V alloy were determined by three-point bending, tensile, fatigue tests and indentation tests. The bending, tensile and fatigue tests were performed on an INSTRON 8801 hydraulic mechanical static testing machine as shown in Figure 3.10 and its specifications is described in Table 3.3. The Instron 8801 material testing system is a closed loop servo-hydraulic, dynamic, single axis fatigue testing system. The machine is equipped with a hydraulically actuated self-aligning gripping system. To ensure the vertical alignment of the specimen specially machined metal inserts are used during the tests. Any preloading induced during clamping is adjusted to zero prior to testing by balancing of the load cell after clamping.

There are three controlling modes such as Position, Load and Strain. The Capacity of the Machine is ± 100 KN. Displacement is ± 75 mm. Strain is ± 25%. The maximum frequency applied is 100 Hz.

Coated and uncoated fatigue test specimens are used. Results of the fatigue tests are typically presented as a plot of applied stress (S) against number (N) of cycles to failure. The ordinate is generally the stress or strain amplitude or the maximum stress or strain in a cycle and is plotted on a linear scale. The abscissa is the number of cycles to failure for a fixed stress cycle and is plotted on a logarithmic scale. The stress levels chosen for fatigue testing will be based on the design stress.

A PC interfaced with the testing frame is used for test data acquisition. The software provides position and corresponding load of the test with a constant position increment till fracture at the ultimate tensile strength which is logged along with the final position before fracture. Tensile tests are carried out by using software called Blue Hill and fatigue tests are carried out using Wave Maker, FLAPS Software, which provided complete machine control, data acquisition, data reduction and analysis capability. Tensile tests are carried out under position control. The software logged position and corresponding load of the test with a constant position increment until fracture occurred at the ultimate tensile strength. The elastic modulus is calculated using the load and position data obtained throughout the test. The final stress value just before the fracture is selected as the tensile strength and the final actuator position gave the corresponding strain.

Table 3.3 Equipment specification for INSTRON 8801

Model	Dynamic Loading Machine Instron 8801
Manufacturer	Instron Ltd. Co.
Specification	Load cell 100 kN , Hydralic grips, Standard 50 mm extensometer
Application	Monitoring the tensile strength, strain, stress and fatigue of metals

Figure 3.10 Mechanical Testing Machine (Instron 8801)

3.4.1 Three Point Bending Tests

Three point bending tests are conducted using an INSTRON 8801 mechanical testing machine where the specimen rests on two supports and is loaded by means

of a loading nose midway between the supports. The specimen is deflected until rupture occurs in the outer surface of the test specimen or until a maximum strain of 5% is reached [ASTM D-790] [106].

Rectangular coated and uncoated samples are placed on a three-point support fixture, during the tests, the load and displacement characteristics are recorded. The tests are terminated when the coating failed or it reaches the 5% of its flexural strain. The load (P) for each test is recorded, and the bending strength (σ_b) of the coated and uncoated was calculated by the formula given below[106]:

$$\sigma_b = \frac{3PL}{2bd^2} \tag{3.1}$$

where P = break load, L = span, b = sample width, and d = sample thickness.

The photographs of three-point testing unit is shown in Figure 3.11 and a workpiece after the bending test is shown in Figure 3.12.

Figure 3.11 – A photograph of three-point bending test set up.

Figure 3.12 – A photograph of workpiece after the three-point bending test.

3.4.1.1 Determining Young's Modulus by Three Point-Bending

The formulation of Young's modulus is detailed in the following study [29], therefore, only the governing equations will be presented. After assuming the symmetry during the three bending test in relation to Figure (3.13), Young's modulus can be determined. The formulation of Young's modulus is given in the Appendix. The resulting equation for the Young's modulus can be written as:

$$E_c I_c + E_s I_s = \frac{Pl^3}{48d} \tag{3.2}$$

or

$$E_c = \frac{Pl^3}{(48d)I_c} - E_s \frac{I_s}{I_c} \tag{3.3}$$

where I_s and I_c are the second moment of area of the substrate material and the coating, P is the applied load, l is the distance between the supports, and d is the displacement of the substrate material and coating during the bending tests. The second moment of area of the base material and the coating are:

$$I_s = \int_{-h_s/2}^{h_s/2} y^2 b dy \quad \text{and} \quad I_c = \int_{hs/2}^{(h_s/2)+h_c} y^2 b dy \tag{3.4}$$

where b is the width of the substrate material and the coating. Equation 3.3 and Table 3.4 are used to determine the Young's modulus of the coating. The Young modules of the substrate material is taken as 113 GPa [29]. It should be noted that the coating was applied to one side of the specimen, which, in turn, results in a non-symmetric situation along the central plane of the specimen. Therefore, a shift of $\frac{h_c}{2}$ occurs in the symmetry axis. In the calculations, this small shift is omitted, which is results into a small error in the calculations. The error estimation is given in the Appendix.

The error related to the load displacement characteristics (Figure (4.1) and Table 3.4) obtained from the three point measurement is in the order of 3%. The measurement errors are based on the data obtained from the five repeats of the experiments.

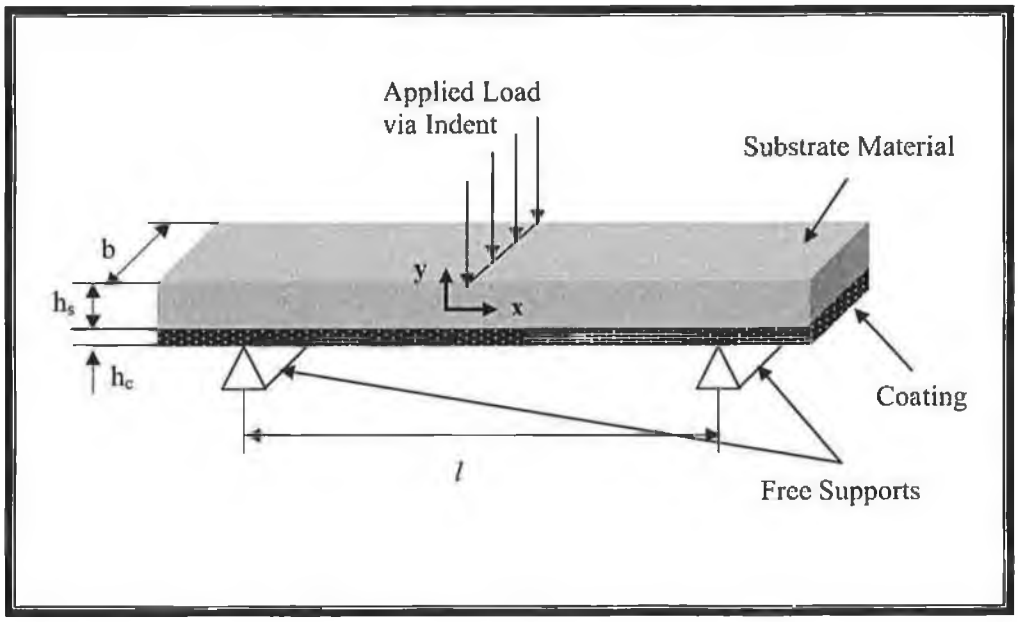

Figure 3.13 – A schematic view of three-point bending testing and relevant dimensions.

Table 3.4 Data used in calculating of Young's modulus from three-point bending tests.

	Specimens Dimension				**From experimental measurements**	
	l (m)	b (m)	h_s (m)	h_c (m)	d (m)	P (N)
As Received coating	0.048	0.0135	0.003	0.00025	0.0019	3400
Heat Treated coating	0.048	0.012	0.003	0.00025	0.002	2800

The Young modules of the base material is 113 GPa. Young's modules determined from the three point bending are given in Table 4.3.

3.4.2 Tensile Tests

The tensile test is the most fundamental type of mechanical test that can be performed on a material. Tensile tests are simple, relatively inexpensive, and fully standardized. By pulling on something, it can be determined how the material will react to forces being applied in tension. As the material is being pulled, its strength along with how much it will elongate can be determined. Data from test are used to determine the elastic limit, elongation, modulus of elasticity, proportional limit, reduction in area, tensile strength, yield point, yield strength and other tensile properties. Procedures for tensile tests of metals are given in ASTM E-8 [107]. This standard procedure is for tension testing of metallic material under uniaxial tensile stress at room temperature, specifically, the methods for determination of yield strength, yield point elongation, tensile strength, elongation, and reduction of area.

Tensile testing was performed on an Instron 8801 testing system which is capable of doing a wide variety of mechanical tests. Instrument control (including standard and customizable methods) and data collection and analysis are performed through Instron's Bluehill software. The setup is equipped with an environmental chamber that allows testing over a wide range of highly controlled temperatures for conducting tensile tests.

The test specimen is placed in between the upper and lower self aligning mechanical grips. The elastic modulus is obtained by getting the load and position

data throughout the test. The maximum stress value just before fracture is selected as the tensile strength and the final actuator position gave the fracture point. The tensile tests were conducted at a cross head speed of 2 mm/min. Minimum of 3 specimens were tested for each condition.

The apparent or the ultimate tensile strength is calculated as following:

$$\sigma_a = P/ (A_m) \quad (3.5)$$

where, P is the Maximum load and A_m is the Minimum Cross sectional area. The experimental error based on the three repeat is in the order of 4%.

3.4.3 Fatigue Tests

ASTM E466 [108] describes the procedure for the performance of high cycle axial fatigue tests (cyclic load of tension and compression in the axial direction only) to obtain the fatigue strength of metallic materials in the fatigue regime where the strains are predominately elastic both upon initial loading and throughout the test. The method is limited to the fatigue testing of axial unnotched as well as notched specimens subjected to constant amplitude, periodic forcing function in air at room temperature.

The fatigue tested workpieces were categorized into four groups. These are as received, which is a base substrate material, as received coated, which was HVOF coated, as received heat treated, in which the base material was heat treated, and coated and heat treated, in which coated workpieces were heat treated. ASTM E-739 [109] standard which is the practice for statistical analysis of linear or linearized stress life (S-N) and strain life (ε-N) fatigue data is employed to secure the reliable fatigue data, for example, a replication of 85% is accommodated in tests.

To perform the fatigue test, initially it is ramped to mean load level and then a sinusoidal loading with a frequency of 20 Hz at a stress ratio R = 0.1. The maximum cyclic stress ranged approximately from 40% to 80% of tensile strength of the specimens that was obtained from the tensile tests. As received and coated as well as heat treated and coated heat treated samples were tested at different maximum alternating stresses, which depend upon the yield strength of the workpieces. Therefore, 80%, 70%, 65%, 40% of the ultimate tensile stress (as obtained from the tensile experiment) was used as maximum alternating stress in the fatigue tests. In this case, the maximum stresses for as received workpieces ranged 859 – 553 MPa, for as received and coated workpieces ranged 788 – 394 MPa, for as received heat treated ranged 805 – 537 MPa, and for coated and heat treated ranged 493 – 394 MPa. It should be noted that tensile stress is determined from load over the cross-sectional area of the workpiece, in which coating area was included.

However, Alternating stress (S) and cycle of failure (N) can be related through Basquin relation [22]:

$$S = AN^{-m} \tag{3.6}$$

where A and m are constants for each workpiece material.

Equation 3.6 can be used to estimate the percentage of reduction fatigue life [22]. In this case, equation determining the fatigue life reduction in percentage is:

$$R = \frac{N^{coated} - N^{substrate}}{N^{substrate}} \tag{3.7}$$

where N^{coated} is the cycle of failure of coated workpieces (whether heat treated coated or coated only) and $N^{substrate}$ is the cycle of failure of substrate material. Equations 3.6 and 3.7 are used to determine the fatigue life reduction in percentage for heat treated and untreated coated workpieces.

The experimental error estimated is based on the three repeats is in the order of 4.5%.

3.4.4 Vicker's Indentation Test

The Vicker's indentation tests are carried out to estimate the plane fracture toughness of the coating as well as Young's modulus. Indentation testing is a mechanical testing process designed to determine the properties of materials by applying the indenter at the surface of a sample. Surface indentation has long been the domain of hardness testing. Vickers is traditional indentation hardness test that is carried out to estimate the plane fracture toughness of the coating.

The test is preformed by Indentation Hardness Tester manufactured by BUEHLER Com. (Figure 3.14). The fraction toughness of the surface is measured using the indenter test data for microhardness (Vickers) and crack inhibiting. In this case, microhardness in HV and the crack length generated due to indentation at the surface is measured using 20N load on mounted cross sections of the coated samples. Moreover, in order to visualize the cracks formed around the indention mark, top surface of coating was grinded. The specification of the indentation hardness tester is shown in Table 3.5.

Table 3.5 Specification of Indentation Hardness Tester

Model	Manufacturer	specifications
5112	BUEHLER®	• Force range of 2N to 200N • Two Objectives and a Vickers Indenter Mounted on a Motorized Turret • Large Easy-To-Use LCD Console for Tester Control and Hardness Readout • Precision Digital Filar with 0.1μm Resolution • Powerful Halogen Illuminator

Figure 3.14 Indentation Hardness Tester BUEHLER® [100]

3.4.4.1 Determining Young's Modulus by Indentation Test

The elastic response of the surface when subjected to indention test needs to be considered in order that the Young's modulus can be determined. After considering Figure (3.15a), the Young's modules can be formulated as [29]:

$$E^{*} = (\frac{9}{16})^{0.5} P.h^{-1.5}.R^{-0.5} \qquad (3.8)$$

Where P is the applied load, h is the elastic penetration of the indenter, and R is the equivalent radius of the indenter, which can be calculated as $D_{eq} = 4A/P$ where A

is area and P is the perimeter of the indented mark, and the radius will be as R = $D_{eq}/2$. However, the formulation of the equal diameter used in equation 3.8 is tested for the Inconel 625 HVOF sprayed coating. The Young's modules resulted from equation 3.8 differs 5% from the data (209 GPa) reported in the open literature [11].

The coating true modulus of elasticity can be determined using the indenter properties [29,101]:

$$E = \frac{1-\upsilon^2}{\frac{1}{E^*} - \frac{(1-\upsilon_i^2)}{E_i}} \tag{3.9}$$

Where E_i and ν_i are the Young's modulus and Poisson's ratio of indenter, respectively. In the calculations E_i = 1141 GPa and ν_i = 0.07 (diamond indenter), and ν = 0.24 were taken [101].

The fracture toughness of the surface is measured using the indenter test data for microhardness (Vickers) and crack inhibiting (Figure (3.15b)). In this case, microhardness in HV and the crack length generated due to indentation at the surface are measured. The fracture toughness (K) is calculated using the equation given below [29]:

$$K = 0.016\left(\frac{E}{H}\right)^{0.5}.P.C^{-1.5} \qquad (3.10)$$

where H is the coating hardness (Vickers), P is the applied load on indenter, C is the crack length. The data used for the calculations are given in Table 3.6. Moreover, in order to visualize the cracks formed around the indention mark, top surface of coating is grinded slightly.

The experimental error is estimated using the data obtained from the five repeats of the tests. The error estimated is in the order of 6%.

Table 3.6 – Data obtained after indenting tests for the coating.

	E (GPa)	E* (GPa)	H (HV)	P (N)	C (μm)	R (μm)	h (μm)
As Received coated	341	280	500 (4904 MPa)	20	40	60	2.5
Heat Treated coated	148	141	480 (4707 MPa)	20	40	75	4.5

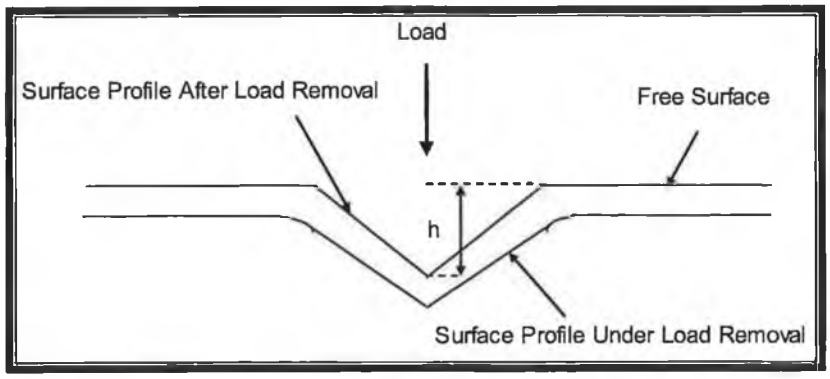

Figure 3.15a – A schematic view of indention and relevant dimensions adapted from [29].

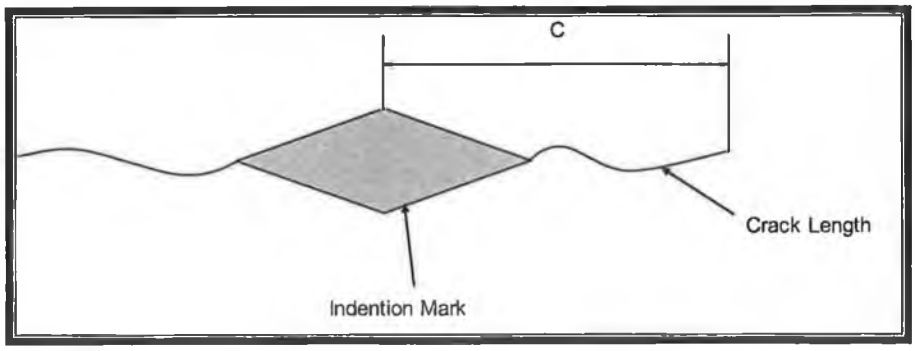

Figure 3.15b – Geometric configuration of indention mark and crack length in relation to fracture toughness measurement adapted from [29].

3.5 CHARACTERIZATION TESTS

3.5.1 SEM & EDS AND OPTICAL MICROSCOPE

The microstructural and elemental characterization of the powder and cross sections of the deposited coatings are investigated using scanning electron microscopy (SEM) equipped with energy dispersive spectroscopy (EDS) and using optical microscope. The tests are performed using JEOL JSM 6460 LV with specifications of resolution 3.0 nm, accelerating voltage 0.3 to 30 kV, and magnification ×5 to 300,000 as shown in Figure 3.16.

The optical microscope equipment that used in this study is manufactured by Olympus as shown in Figure 3.17. it is Olympus BX 60 optical microscope with Polaroid digital microscope camera (DMC) attached to it. It is used for microscopic observations and to obtain optical micrographs of the surfaces. The microscope has a revolving nosepiece with 5 objective lenses of various magnifications attached to it. The magnification levels are, 50X, 100X, 200X, 500X and 1000X.

Figure 3.16 Scanning Electron Microscope model JEOL JSM 6460 LV

Figure 3.17 Olympus Optical microscopy set-up

3.5.2 X-Ray Diffraction (XRD)

X-ray Diffraction (XRD) is an efficient analytical technique used to characterize and identify the coatings based on their characteristic diffraction behavior under X-ray irradiation of a known wavelength, for example, each structure or phase will only diffract an incident X-ray at a specific set of incident angles, which can be measured. Bruker XRD machine model AXD8 is used in XRD examination. Its specifications and picture are shown in Table 3.7 and Figure 3.18 respectively.

Table 3.7 X-Ray Diffraction machine specifications

Model	AXS D8 Bruker Inc.
Sample Positioning & Rotation	Goniometer; Eulerian Cradle; Theta-Theta, Theta-2Theta
X-Ray Source & Optics	Collimator or slits to reduce angular divergence in the incident beam
Performance Specifications	• 2-Theta Angular Range (degrees) -110 to 168 • Peak Count Rate (cps) 2.00E6 • Max Sample Dia (mm) 600 • Computer based interface and display; Other digital or analog interface or display; Ability to process and analyze the diffraction data

3.5.3 Samples Mounting

The metallographic samples for coating structure evaluation are cut from section of specimens and mounted using automatic mounting press manufactured by BUEHLER as shown in Figure 3.19.

Figure 3.18 X-Ray Diffraction machine model AXS D8 Bruker Inc.

Figure 3.19 Automatic Mounting Press (BUEHLER® SimpliMet® 3000) [100]

3.6 FINITE ELEMENT MODELING

Finite element method (FEM) is a powerful technique originally developed for numerical solution of complex problems in structural mechanics, and it remains the method of choice for complex systems. In the FEM, the structural system is modeled by a set of appropriate finite elements interconnected at points called nodes. Elements may have physical properties such as thickness, coefficient of thermal expansion, density, Young's modulus, shear modulus and Poisson's ratio. To develop a finite element procedure for the stress computation, the principle of virtual work is used. With virtual prototyping techniques, users can iterate various scenarios to optimize the product long before the manufacturing is started. This enables a reduction in the level of risk, and in the cost of ineffective designs [102].

According to this principle, the equilibrium of any body under loading requires that for any compatible small virtual displacements imposed on the body in its state of equilibrium, the total virtual internal work or strain energy (δU) is equal to the total virtual external work due to the applied thermal loads (δV), i.e. $\delta U = \delta V$. The virtual displacements are zero at the boundary points and surfaces. For the static analysis of problems having linear geometry and thermo-elastic material behavior, one can derive the following equation using the standard procedure as

$$\int_V (\delta\varepsilon^T D\varepsilon - \delta\varepsilon^T D\varepsilon^t)\, dV = \int_V \delta\mathbf{u}^T\mathbf{f}^B\, dV + \int_S \delta\mathbf{u}^T\mathbf{f}^S\, dS + \delta\mathbf{u}^T\mathbf{f}^C \qquad (3.11)$$

where V and S denote the volume and surface, $\mathbf{f}^B$, $\mathbf{f}^S$ and $\mathbf{f}^C$ stand for the vectors of body, surface and concentrated forces, respectively.

The elemental displacement vector $\mathbf{d}_e$ is related to the nodal displacement vector $\mathbf{d}_i$ by:

$$\mathbf{d}_e = N\,\mathbf{d}_i \tag{3.12}$$

where N is the matrix of shape or interpolation functions. The elemental strain vector ε_e is written as

$$\varepsilon_e = L\,\mathbf{d}_e \tag{3.13}$$

where L is a differential operator matrix. Consequently, the strain vector ε_e is related to the nodal displacement vector $\mathbf{d}_i$ by:

$$\varepsilon_e = L\,N\,\mathbf{d}_i = B\,\mathbf{d}_i \tag{3.14}$$

where B (= L N) is the strain displacement gradient matrix. As a result, the equation 3.11 is reduced to the following matrix form (after the assemblage):

$$K\bar{\mathbf{d}}\ \mathbf{F}^t = \mathbf{F}^b + \mathbf{F}^s + \mathbf{F}^c \tag{3.15}$$

where $\mathbf{d}$ is the global displacement vector and the elemental matrices and vectors are given as:

$K_e = \int_V B^T D B\, dV$ = elemental stiffness matrix,

$\mathbf{F}^t = \int_V B^T D \varepsilon^t\, dV$ = elemental thermal load vector,

$\mathbf{F}^b = \int_V N^T \mathbf{f}^B\, dV$ = elemental body force vector,

$\mathbf{F}^s = \int_S N^T \mathbf{f}^S \, dS$ = elemental surface force vector and

$\mathbf{F}^c = N^T \mathbf{f}^C$ = elemental concentrated force vector.

Equation (3.14) is now expressed as

$$\mathbf{K}\mathbf{d} = \mathbf{F}^t + \mathbf{F}^b + \mathbf{F}^s + \mathbf{F}^c = \mathbf{F} \qquad (3.16)$$

where **F** is the global force vector. Solution of the above set of simultaneous algebraic equations yields the unknown nodal displacements and reaction forces. Once the displacement field due to temperature rise in the substrate is known, then the corresponding strains and stresses can be calculated.

A number of material-related factors can cause the structure's stiffness to change during the course of an analysis. Nonlinear stress-strain relationships of plastic cause a structure's stiffness to change at different load levels. These changes are incorporated into an ANSYS analysis through using the appropriate element types.

ANSYS provides a cost-effective way to explore the performance of products or processes in a virtual environment. This type of product development is termed virtual prototyping. ANSYS is general-purpose finite element analysis software package.

Tests specimens were simulated using the commercial finite element package ANSYS 8.0. The substrate and coating were modeled as elastic-plastic material using the Multi-linear Isotropic Hardening (MISO) option of ANSYS. MISO uses

the von-Mises yield criteria coupled with an isotropic work hardening assumption. This option is often preferred for large strain analyses [102].

Due to the symmetrical nature of the problem, first the half of the beam with coating was modeled using VISCO107 elements. VISCO107 is used for 3-D modeling of solid structures. It is defined by eight nodes having three degrees of freedom at each node: translations in the nodal x, y and z directions. The element is designed to solve both isochoric (volume preserving) rate-independent and rate-dependent large strain plasticity problems. Meshing was done using 3000 elements, grid refinement being used near the loading plane. One end of the workpiece was considered as fixed while load was applied to the one end of the workpiece to resemble the loading used in experimental. Displacement in the vertical direction (UY) was constrained at the left end of the beam. Figure 3.20a and Figure 3.20b show the workpieces used in the FEM simulations for three point bending and tensile test. The 3-D view of the mesh used in simulations of three point bend and tensile tests are also shown in Figure 3.21a and 3.21b. Moreover, the 2-D view of the mesh used for the three point bending is shown in Figure 3.22a while the close view of the meshes in the central region of the workpiece is shown in Figure 3.22b.

Considering the cross-sectional dimensions of the test pieces and from the analysis of 3D model results, a plane strain 2D model using VISCO108 was assumed to be sufficient to simulate beam bending with or without coating. VISCO108 is used for 2-D modeling of solid structures and is defined by ten nodes having up to three

degrees of freedom at each node: translations in the nodal x, y, and z directions. Meshing was done using 1500 elements to model without coating. With coating, the number of elements increases to 3000.

The geometric simulation condition is shown in Figure 20.a. In the simulations, the workpiece is assumed to be free from any stresses and there is no defect for the coating base material adherence. The coating side of the workpiece is located at the opposite side of the applied load. The size of the workpiece used in the simulation is given in Table 3.4. In order to simulate the experimental conditions, the elastic modules of the coating determined from the three point bending tests are used in the simulations. The modules of elasticity of the base material is taken as 113 GPa in the simulations. The initial and boundary conditions for the workpiece for the FEM simulations are:

- Initially, it is assumed that coating and the base substrate are free from any stresses, for example, no residual stress condition is assumed initially (prior to bending).
- Two supports opposite to the loading surface are located with a span similar to that is used in the experiment.
- The glue function is introduced between the coating and the substrate material. This provides no slip condition at the coating-base material interface during the bending simulations.
- The applied force-displacement characteristics similar to that observed in the experiment are adopted.

- No mechanical constraints at free surfaces of the workpiece are assumed; in which case, the bending takes place due to the applied load only and no external compression/tension forces as well as external resisting surfaces are considered in the bending simulations.

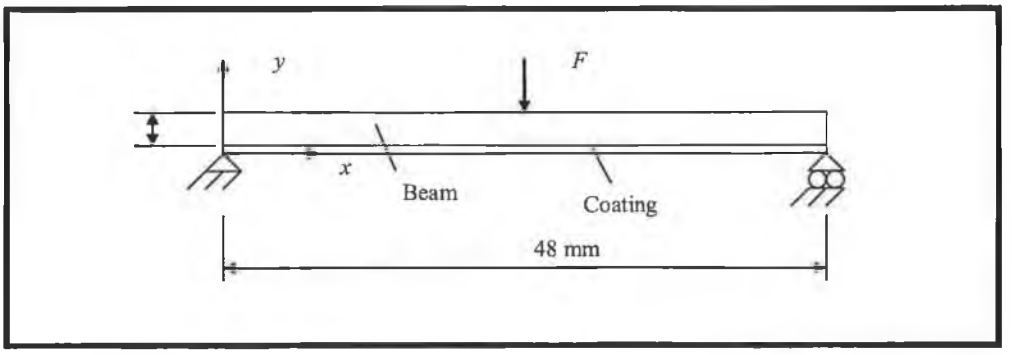

Figure 3.20a – Three-dimensional view of workpiece used in the simulations of the three point bending test. The coating and the substrate material are free from the stresses prior to the bending.

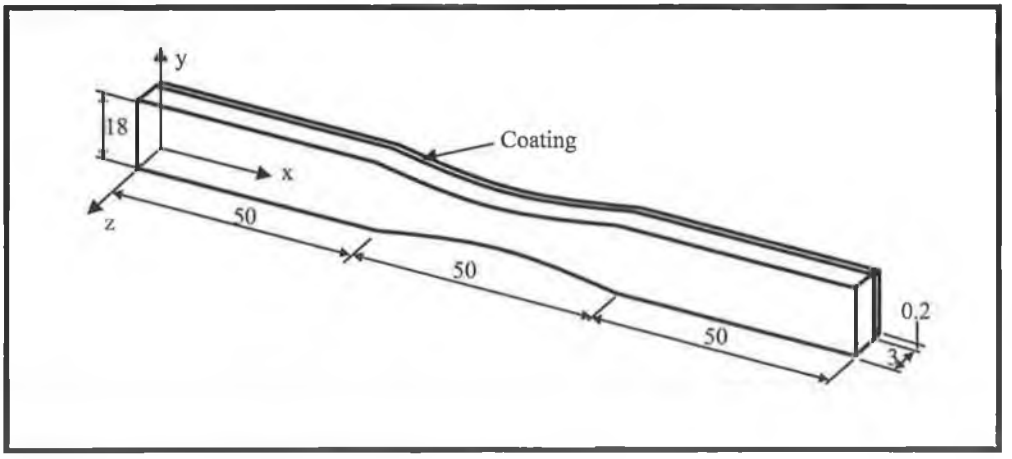

Figure 3.20b – Three-dimensional view of workpiece used in the simulations of tensile test.

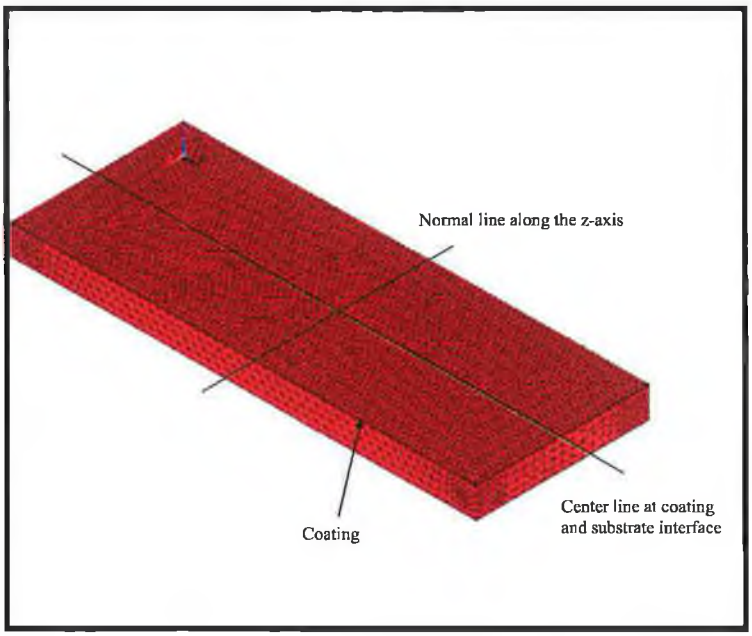

Figure 3.21a 3-D view of the mesh used in simulations of three point bending test simulations.

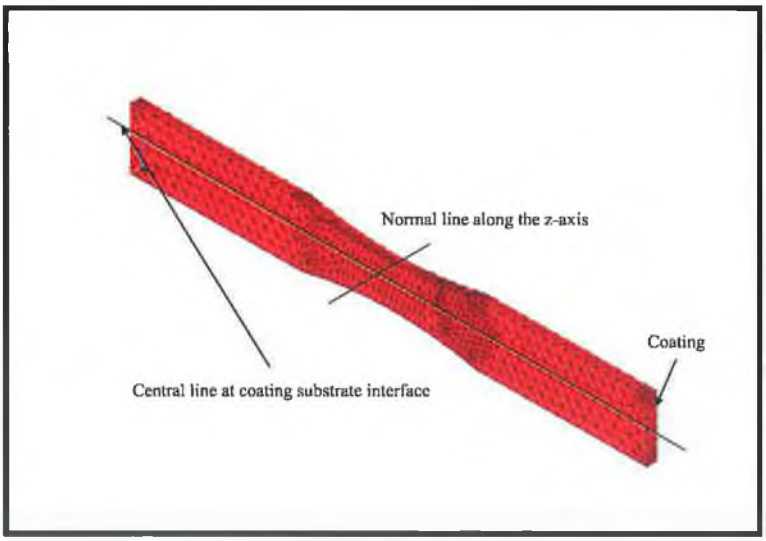

Figure 3.21b 3-D view of the mesh used in simulations of tensile test simulations.

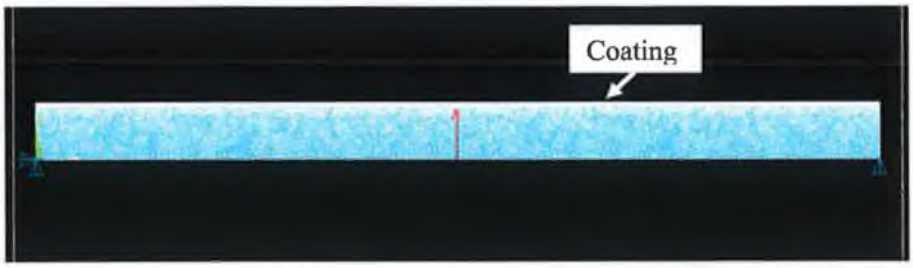

Figure 3.22a, 2-D view of the mesh used in the three point bending test simulations. The mesh corresponds to cross-sectional view along the x-axis of the workpiece.

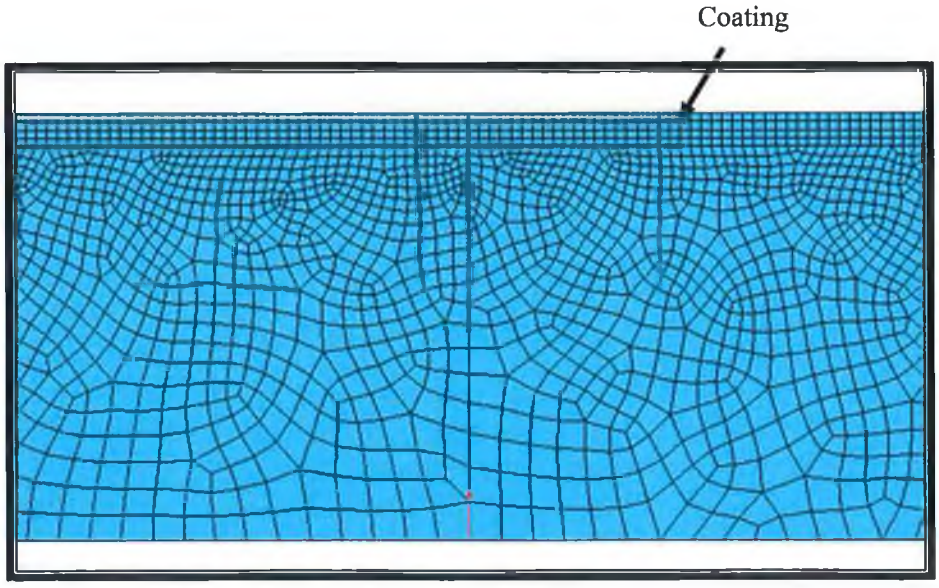

Figure 3.22b, 2-D close view of the mesh in the central region of the workpiece, which is used for the three point bending test simulations. The top surface is the coating.

Chapter 4 - Results and Discussion

The results and discussions are classified according to the mechanical tests carried out in the present work. Therefore, the discussions of the findings are given under the appropriate headings.

4.1 Three-Point Bending Tests:

Three-point bending tests are carried out to investigate the coating-base material interface properties of HVOF coating of AMDRY 9954 powders on Ti-6Al-4V alloy. The influences of heat treatment on interface properties are also examined. Finite element method (FEM) simulating the experimental conditions is carried out to predict the stress field during the bending tests.

The elasto-plastic behavior of the workpiece with coating and without coating as well as with heat treatment is shown in Figure 4.1. The data is obtained from the three-point bend tests, which were carried out at constant strain rate. As-received uncoated and coated workpieces show similar elasto-plastic behavior while heat treated coated workpieces and heat treated uncoated differ slightly in behavior. The similar behavior of the load characteristics (up to the load of ~ 3.4 kN and displacement of ~ 1.9 mm) of the as received coated and as received uncoated specimens is because of the temperature build up in the coating during the spraying

process. The temperature of the coating is monitored immediately after the completion of the coating by using optical pyrometer, it is exceeding 735 ^{o}C. Due to the heat transfer from coating to the substrate material, alpha-phase (α) coarsening and beta-phase (β) enhancement were occurred in the substrate material where the heat transfer takes place (partial annealing of the substrate material). The heat transfer and phase transformation were limited within a small distance (depth) in the neighborhood of the coating in the substrate material. This increases slightly the ductility and lowers slightly the load holding capacity of the coated specimen. In this case, the coated specimen and as received specimen (uncoated specimen) behave almost similar. The plastic region for heat treated and heat treated uncoated samples initiate at lower load level (~ 2.8 kN) and longer displacement (~ 2.0 mm) as compared to the as received and as received coated workpieces. This indicates that heat treatment has an effect on the coating, since coated and as-received uncoated workpieces behave similarly, i.e., toughness of the coating changes slightly after the heat treatment. Moreover, the abnormal behaviors in the curves are not observed. This suggests that the gradual deformation of interface of the substrate material could relieve the stress levels at the interface and this has a contributing effect on stress relaxation. Moreover, the compressive stress generated at the top surface of the workpiece does not generate failure, such as peeling due to elastic strain energy stored in the coating.

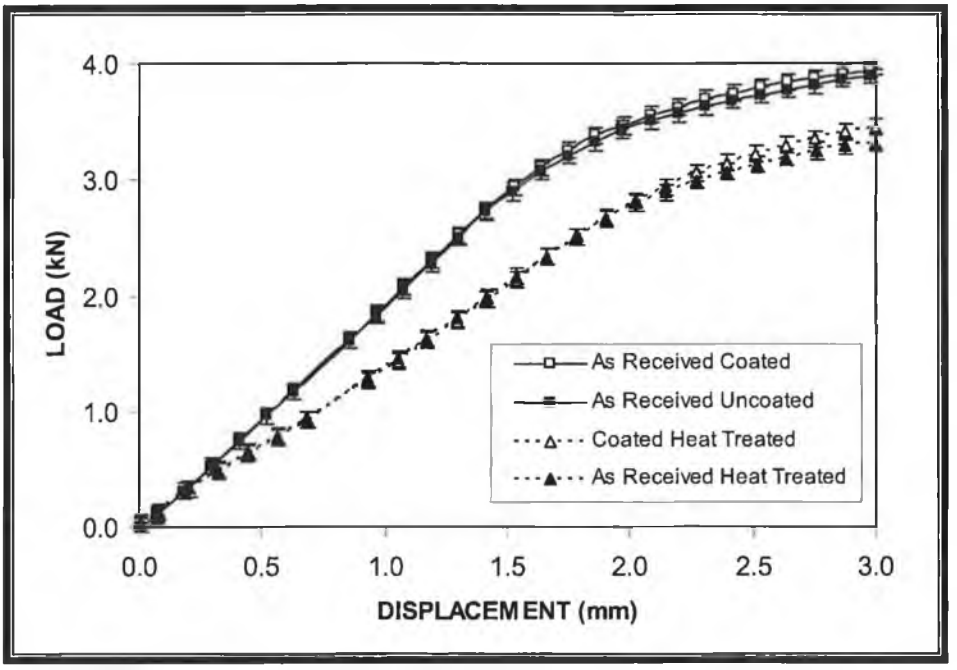

Figure 4.1 – Load and displacement characteristics of the workpiece after three-point bending tests.

Since the coated surface is placed in the bottom (opposite) side where the three-point bend indented is applied, the coating section of the workpiece is subjected to tensile-shear force only. Consequently, the main failure in the coating occurs because of the tensile-shear deformation, particularly coating-substrate material interface. This situation can be seen from the SEM micrographs (figure (4.3)). The crack in the coating is formed due to the tensile load and initiated at the free surface of the coating as well as oxide sites in the coatings. Under the tensile-shear loading, delamination above the plastically deformed region is occurred. This can be observed from figure (4.3). It should be noted that during the thermal spraying process, formation of oxidation is expectedly high in the free surface of the

coating. This, in turn, results in differences in stiffness in the coating layer. Consequently, high oxide content in the surface region of the coating triggers early crack initiation and propagation along the coating and the substrate material interface (figure (4.3)). The development of internal stress, due to tensile-shearing force, creates local stress concentrations, particularly at defect sites (micro voids, irregular micro cavities, high oxide content splats, and splats with the un-molten state during the spraying) in the region of coating-substrate interface. In this case, the defect site has a significant effect on the failure mechanism. It should be noted that stress concentrations at defect sites are, in general, higher than the mean internal stresses. When the critical stress for crack propagation is reached in defect sites at the interface, the entire coating fails and peels off from the substrate material. If the crack propagation is limited to local region, the fracture of the coating is resulted. In this case, internal stress in the coating is relaxed around the crack sites. If the energy used to propagate the crack is dissipated, the crack cannot extend beyond the substrate material, for example, it terminates at the free surface of the substrate material.

Figure 4.2 shows SEM micrographs of coating prior and after the heat treatment process. The coating cross-section reveals that the coating consists of lamellar structure with existence of some small voids between the splats. However, the voids are distributed randomly resulting in overall 3% porosity in the coating. Oxidation around some splats is evident due to the oxidation during in-flight duration of the splat before impacting the substrate surface. In addition, some

stringers like dark inclusions are also observed. These are the brittle oxide particles in the coating.

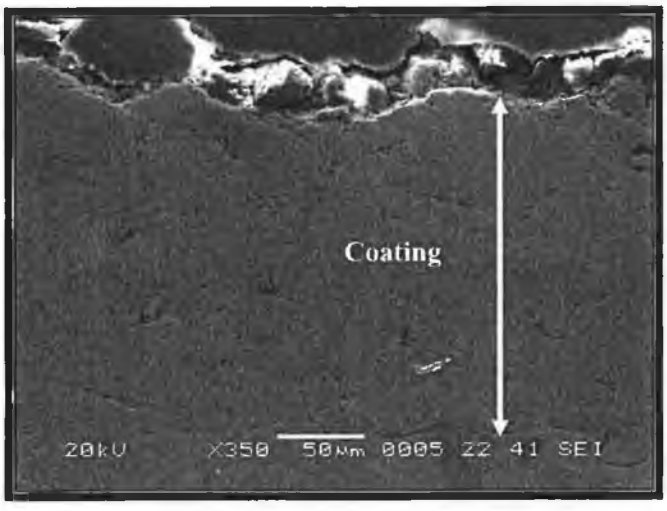

SEM micrograph prior to heat treatment.

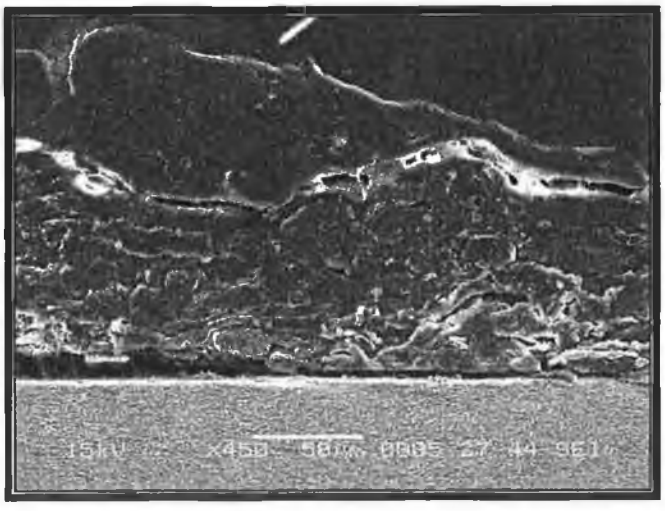

SEM Micrograph after heat treatment.

Figure 4.2. Coating cross-section prior and after the heat treatment process.

Figure 4.3 shows SEM micrographs of the tensile surface as well as the cross-section of the workpiece after the bending tests. Multi-crack deformation in the coating is evident, which shows that coating does not conform to the plastic deformation in the substrate material. In some regions, crack spacing is small indicating that the sliding and splitting deformation occurs in the coating. However, in general, crack spacing is large and in some regions total elimination of coating is resulted (peeling off from the substrate surface) due to shear deformation at coating-substrate interface. In addition, the coating fracture was brittle and no sign of plastification was observed. The metallic particles (splats) de-bond mainly through their oxide interfaces. The elongated particles, particularly oxided brittle particles, promote a high stress concentration and crack initiation. Moreover, adhesion failure was also observed resulting in separation between the substrate and the coating. In the case of heat treated workpieces, thermal stresses generated along the coating-substrate interface, owing to differences in thermal expansion of both materials, influences significantly adherence of coating to the substrate material, despite the fact that gradual cooling in air ambient was carried out. Figure 4.4 shows load-displacement curves obtained from the experiment and simulation. It can be observed that both curves have the same trend, provided that some discrepancies of the both curves are evident (the maximum difference in the forces for the fixed displacement is in the order of 30% in the elastic region). This is because of the residual stresses developed in the coating during the experiments, which is omitted in the FEM simulations. The porosity and the local brittleness due to oxide formation in the coating are neglected in the simulations. The Young's modulus of the coating is assumed to be uniform in the FEM simulations, which is

not strictly correct in the actual coating, since three point bending tests provide mean value of the Young's modulus in the coating. In addition, the coating is formed through the mechanical anchoring of the splats, which in turn results in non-uniform structure unlike the metallic alloys. However, in the simulations, uniform structure with homogenous properties is considered. Nevertheless, the simulations provide insight into the strain and stress levels in the workpiece during the bending tests.

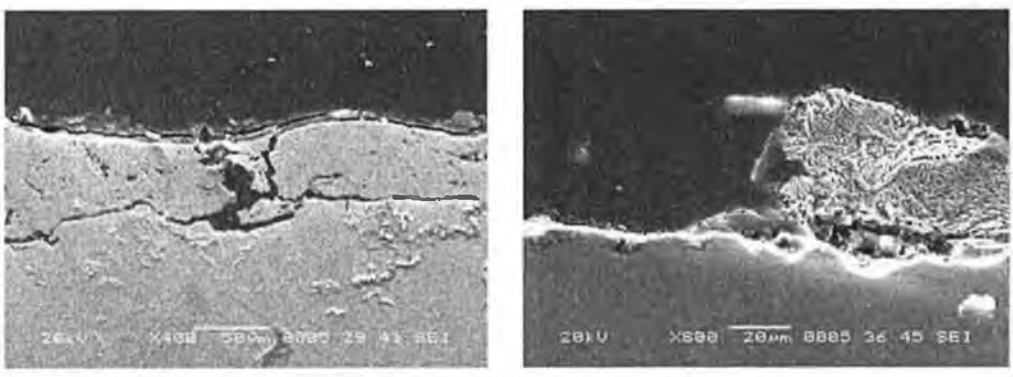

SEM micrograph of cross section of coating in the region close to top surface.

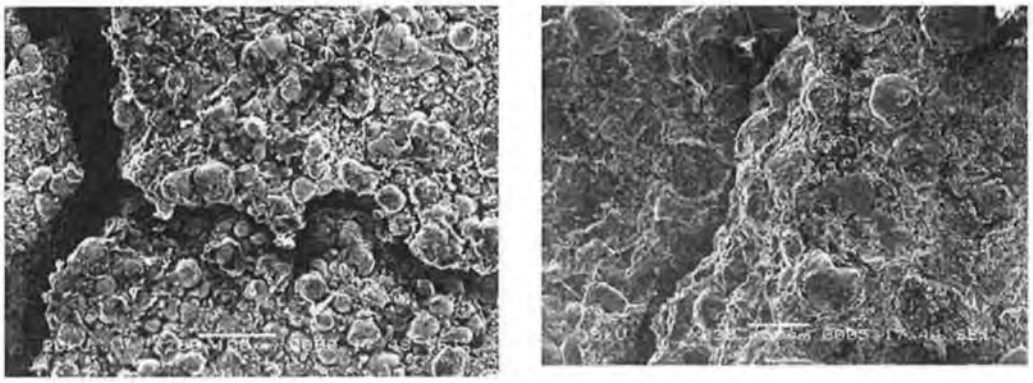

SEM micrograph of fractured surface (view is taken from the top surface).

Figure 4.3. Coating cross-section and top view of coated surface after three-point bending tests.

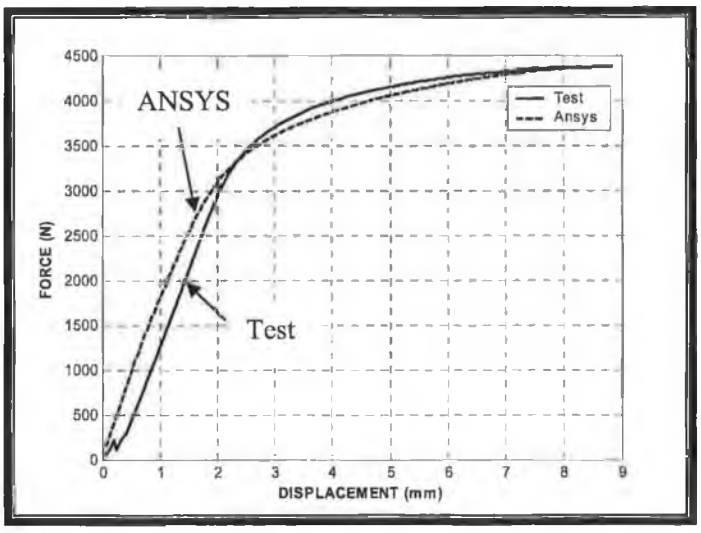

Figure 4.4 – Force versus displacement behavior obtained from three point experiment and used in the FEM (ANSYS) simulations.

Figure 4.5a shows von-Mises stresses corresponding to three load conditions at coating substrate interface while Figure 4.5b shows the von-Mises stress contours in the coating. It should be noted that the first load condition corresponding to the elastic region while second and third load levels are in the elasto-plastic and plastic regions. In the elastic region, the magnitude of the von-Mises stress (440 MPa) is considerably less than the elastic limit of the coating and substrate material (880 MPa [104]). It should be noted that the tensile stress corresponding to load of 3,000 N is in the order of 400 MPa, if it is only tensile as determined from the tensile experiment. In the case of high load level (4250 N), the maximum magnitude of von-Mises stress extends along the horizontal direction with its magnitude exceeding the elastic limit of the coating and base material. This, in turn, results in multi-cracking of the coating within the region of maximum

deflection. This situation can also be observed from Figure 4.3. As the load level increases, von-Mises stress increases sharply (to 880 MPa) in the region of maximum deflection while extension of high magnitude of von-Mises stress at coating interface continues. This causes elongated cracks to be formed in the coating in the deflection region. Although stress relaxation at coating interface is resulted due to elongated cracks, continuation of bending load results in severe damage in the coatings such that partial peeling-off coating from the base material surface is resulted. In the case of Figure 4.5b, it is evident that the high stress concentration is within the bending region of the workpiece. This situation is also observed from figure 4.5c, in which close view of the contour plots in the bending region are shown. However, the region of high stress concentration extends further into the coating as well as the substrate material. It is also evident from figure 4.5c that there is a miss-fit von Mises strain and von Mises stress across the coating and the base substrate material for load levels of 3,000 and 4,250 N. It should be noted that FEM predictions provide qualitative information on the strain and stress levels during the three point bending tests. The predictions and the experimental findings differ because of the assumptions made in the analysis and the experimental errors involved in the measurements. In the simulations, it is assumed that the workpiece is free from any stresses and the coating base material adherence is in perfect conditions. In the real situations, the residual stress is developed in the coating and the coating adherence to the base material is not perfect; in which case, the local cavities and voids are formed at the coating-base substrate interface (Figure (4.2)). In addition, the coating in the actual situation does not have a structural homogeneity due to the formation of voids and local oxide layers around the splats

across the coating. The locally scattered brittle sites (mainly high oxide content splats as observed from the EDS line scans, Figure (4.23)) cause early deformation of the coating through the crack formations. These sites are particularly observed in the region close to the coating free surface.

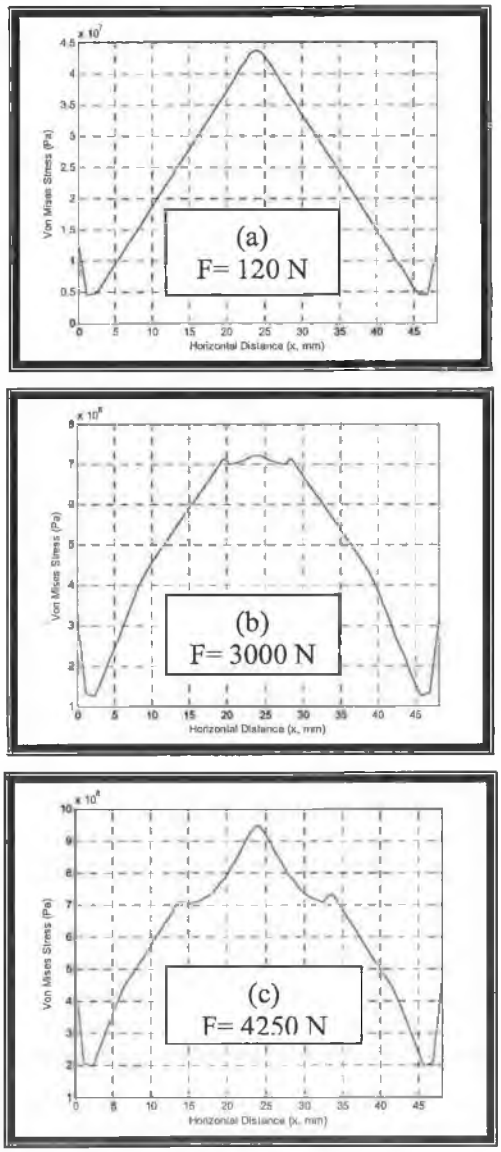

Figure 4.5a – von-Mises stress at three load conditions [(a) at 120 N, (b) at 3000 N, and (c) at 4250 N].

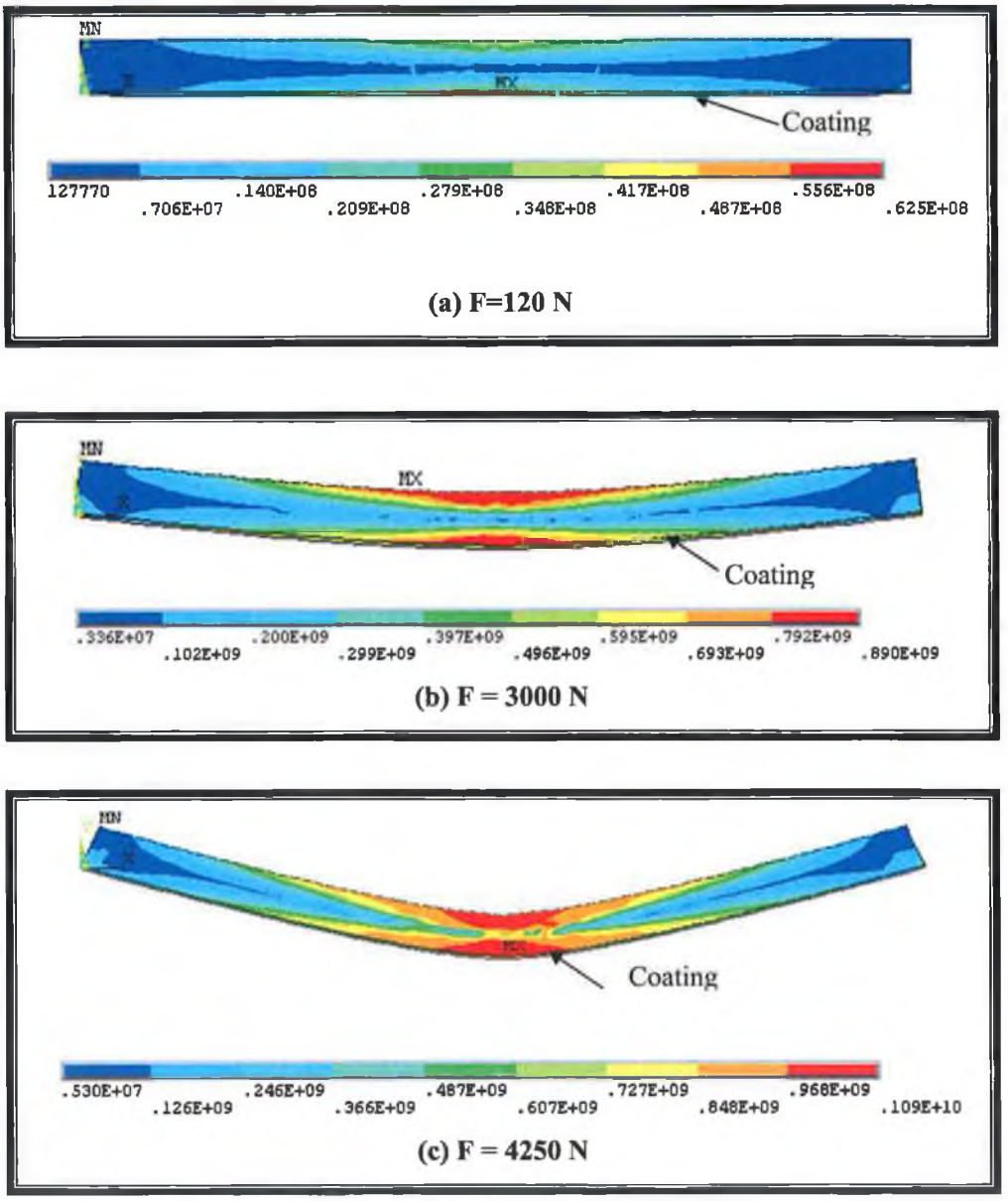

Figure 4.5b Contour plots of von-Mises stress at three load conditions. The stress unit is in Pa. [(a) at 120 N, (b) at 3000 N, and (c) at 4250 N].

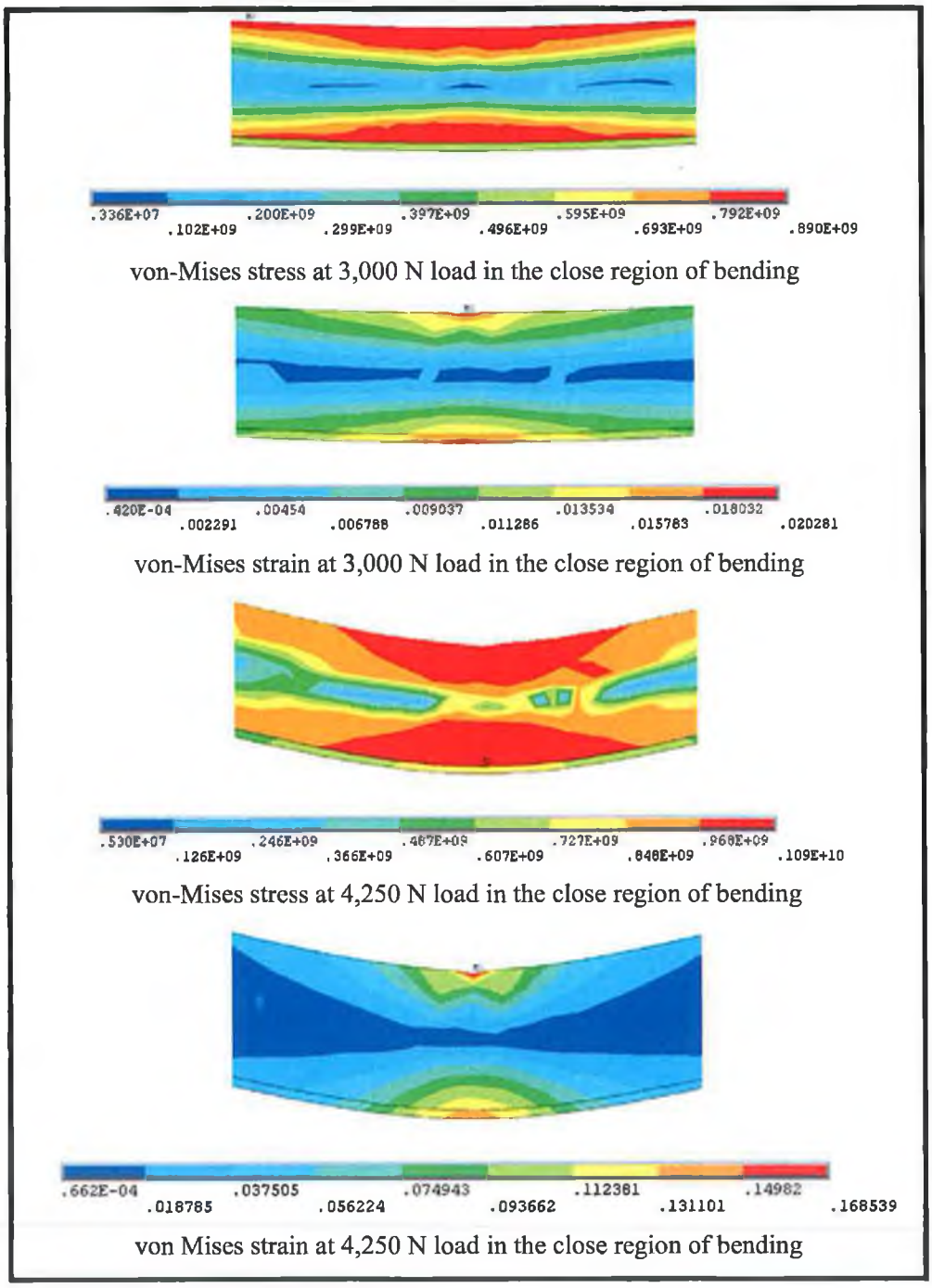

Figure 4.5c Contour plots of von-Mises stress and strain at two load conditions. The stress unit is in Pa. [at 3,000 N, and at 4,250 N].

Figure 4.6a shows total strain at three loading conditions at coating-base material interface while Figure 4.6b shows the contour plot of total strain at three loading conditions. At low loading situation (in the elastic deflection region) total strain (4.2×10^{-4}) is highest at the region of deflection. The axial extension of the total strain is limited with the maximum deflection region. As the load level increases (in elasto-plastic region), total strain extends along the interface in the horizontal direction, provided that maximum total strain (0.0165) occurs in the location of maximum deflection. This indicates that plastic deformation only occurs in the region limited with the maximum deflection. As the load level increases further the magnitude of strain reduces and the total strain reaches its peak value (0.13) at the point of deflection. This suggests that formation of elongated crack in the coating relieves the stress level in the deflection region and the crack formed is not confined to the base material. This situation is also observed from the SEM micrograph Figure 4.3. In the case of Figure 4.6b, total strain attains high values in the region of the maximum deflection. Increasing applied load during the bending results in local increase in the total strain, particularly, in the region of the maximum displacement. The extension of total strain in the radial direction shows the plastic deformation of the substrate material in this region. In addition, the axial extension of the total strain in the region of the maximum displacement is associated with the large area of coating suffering from the plastic deformation in this region. Consequently, the multiple cracks extending in the large of the coating are formed in the region of the maximum deflection. This situation can also be seen from Figure (3.12).

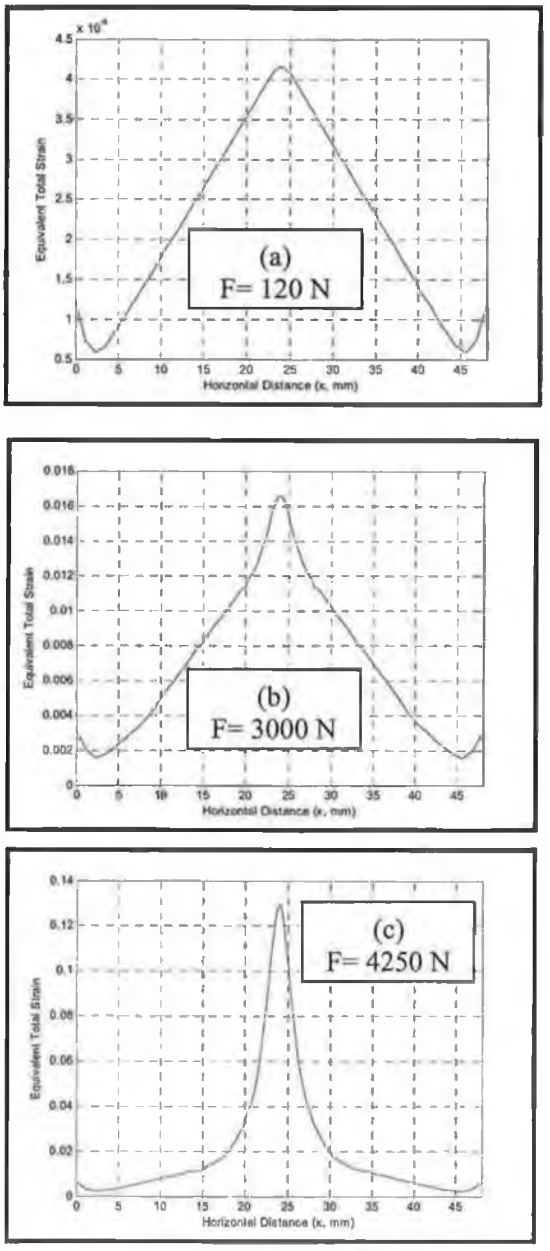

Figure 4.6a Equivalent total strains at three loading conditions at coating-base material interface [(a) at 120 N, (b) at 3000N, and (c) at 4250N]

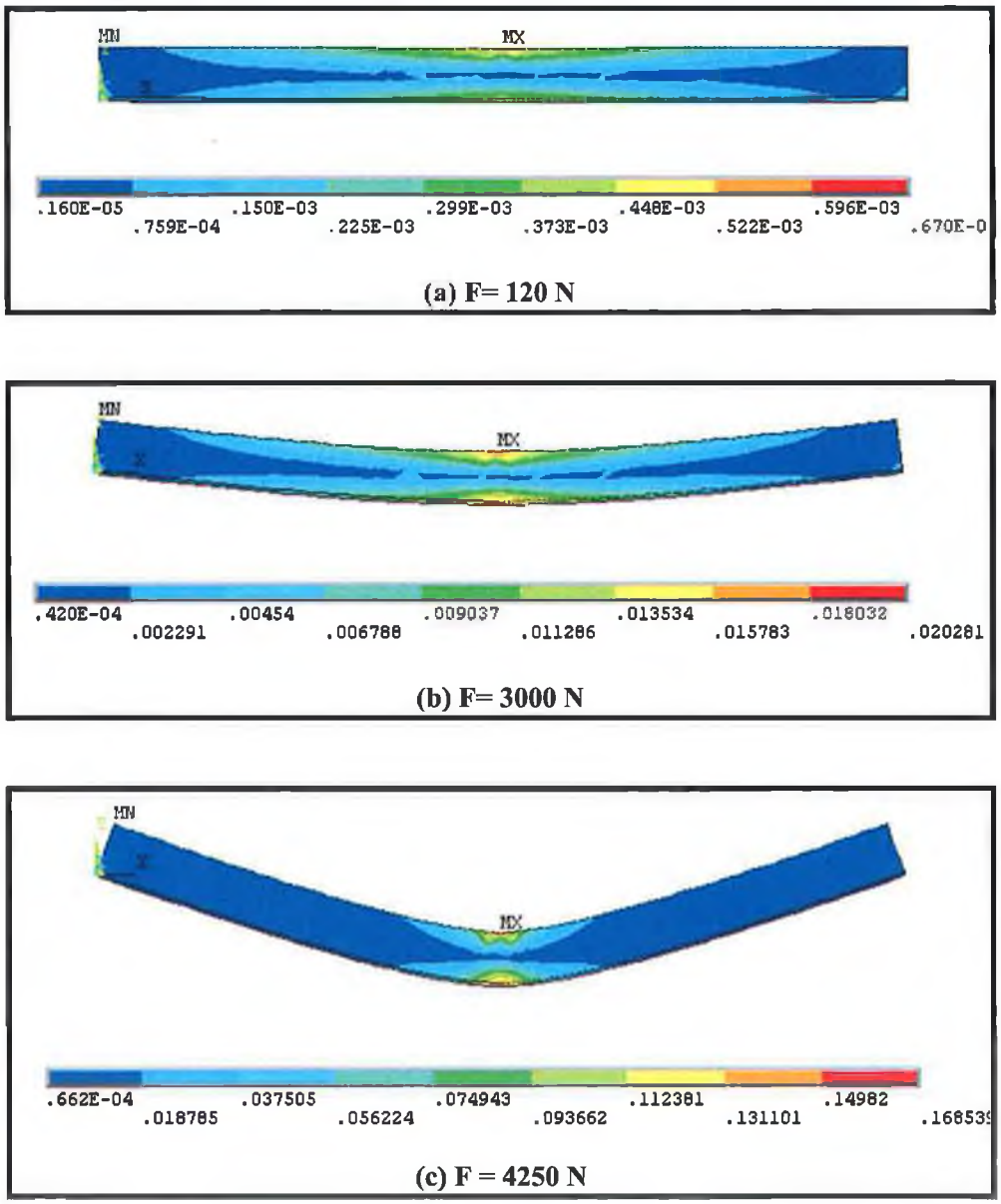

Figure 4.6b Contours plot of total strains at three loading conditions at coating-base material interface [(a) at 120 N, (b) at 3000N, and (c) at 4250N].

Figure 4.6c shows von-Mises along the thickness of the workpiece for three loading conditions. The axial location is the middle point where 24 mm from the free support. The coating is located between 0.0 and 0.25 mm along the thickness in the Figure 4.6c. von-Mises stress reduces gradually towards half thickness of the workpiece and, then, increases towards the top surface where the load is applied. The gradual decrease and increase of von-Mises stress is because of the tensile and compression contribution of the stress field in the workpiece. In the coating region, the stress filed is tensile and it is compressive the in the loading region. Therefore, in region of the half of the workpiece thickness, the magnitude of the stress is small. As the applied load increases (3,000 N), von-Mises stress reaches maximum at some depth below the surface (close to the coating interface) of the substrate material. However, the magnitude of von-Mises stress is not the maximum at the coating-substrate interface. This indicates that the plastic deformation starts not at the coating-substrate interface, but in the substrate (0.5 mm below the surface) close to the interface. Moreover, sharp change in von Mises stress across the coating and the substrate material is observed. This is due to the miss-fit of the stress at the interface. The non-symmetric appearance of the curve along the thickness is because of the coating at the surface of the workpiece. Consequently, the coating modifies significantly the elasto-plastic response of the workpiece after the bending load of 3,000 N, despite the fact that the coating thickness is 0.250 mm. Moreover, the coating is still in the elastic limit of the workpiece (880 MPa) at the applied load of 3,000 N and von-Mises stress increases gradually across the coating thickness towards the coating-base substrate interface. As the bending load increases further, the workpiece undergoes a plastic

deformation in the coating as well as applied load regions. The stress level remains high in the substrate material in the region 0.5 mm below the surface, noted that the stress levels in the coating and at the coating-substrate interface exceed the elastic limit of the substrate material. Moreover, at high applied load (4250 N), the behavior of von-Mises stress along the thickness becomes almost symmetric about the mid-thickness, i.e. the trend of the rise of von-Mises stress from the coating surface and the trend of the decay of von-Mises stress from the applied load surface become similar. Consequently, the influence of the coating on the elastic-plastic behavior of the workpiece becomes less at high load level (4250 N). This is because of the plastic deformation of the coating. It is observed from the experimentally tested workpieces that multiple cracks are formed in the coating once the elastic limit is exceeded. This minimizes the influence of coating on the elasto-plastic behavior of the workpiece.

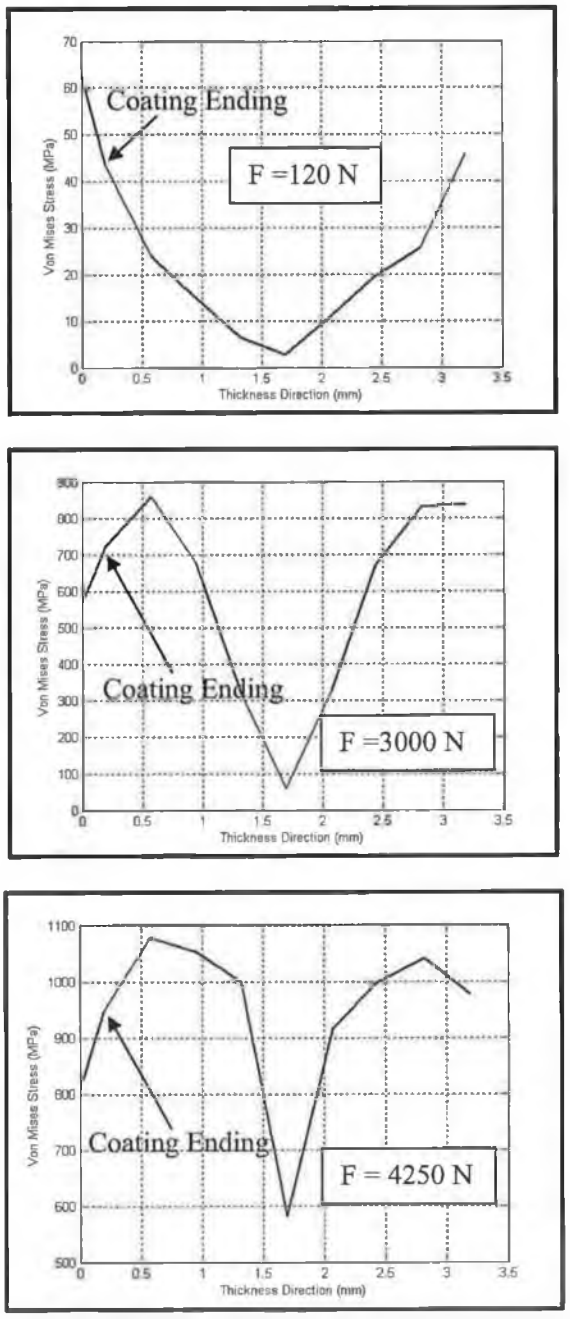

Figure 4.6c von-Mises stress along the thickness (cross-section of the workpiece) and axial location is the middle point (24 mm from the support). Coating is between 0.0 and 0.25 mm along the thickness.

4.2 Fatigue Tests:

Fatigue properties of HVOF spraying of AMDRY 9954 powder sprayed on to Ti-6 Al-4V alloy prior and after heat treatment are examined. Figure 4.7a & b shows SEM micrograph of coating cross-section. The coating thickness within the range of 250 μm is achieved. Lamella structure is observed due to multi-pass spraying process. Partially melted particles are evident appearing as rounded shapes and their distribution is random in the coating. Moreover, partially scattered small pores are observed and the porosity of the coating varies within 2%-4%. Due to high temperature spraying process, oxidation of some splats occurs in-flight to impacting to surface. This is because of the content of the powder particles which contain chromium. Dark inclusions in the coating are the oxide compounds, particularly stringers like oxides are observed in between the splats. High oxygen content is also evident from EDS analysis and given in Table 4.1. In coating, the scattered oxide particles de-bond through their interfaces in the coating.

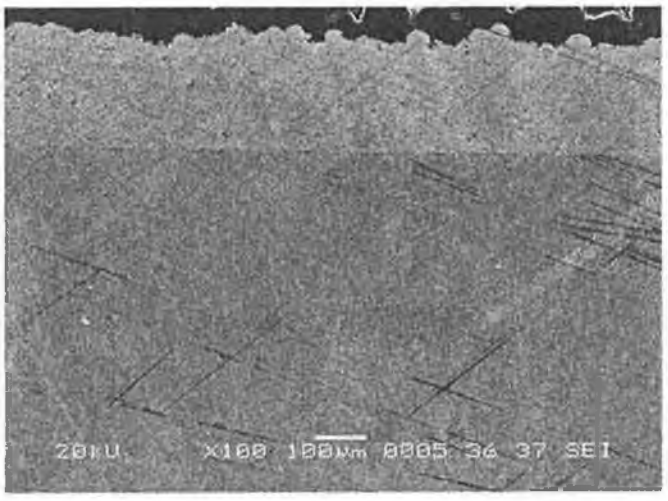

Untreated Coating

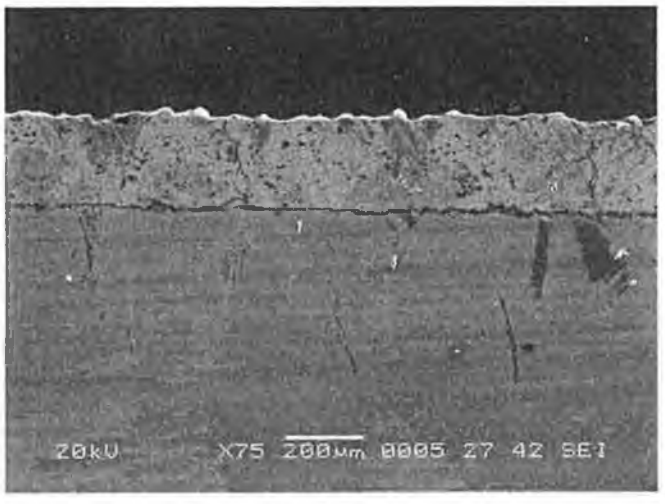

Heat Treated Coating

Figure 4.7.a – SEM micrographs of coating cross-section prior and after heat treatment.

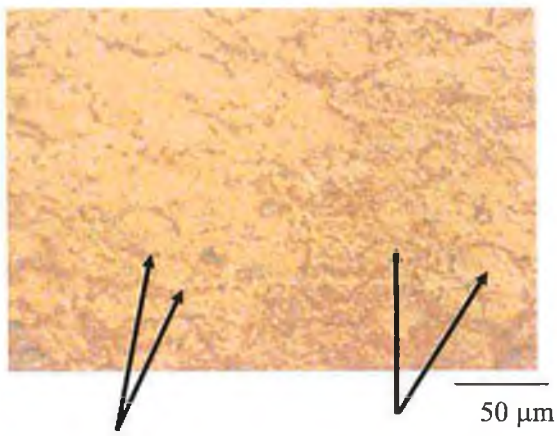

Optical photograph

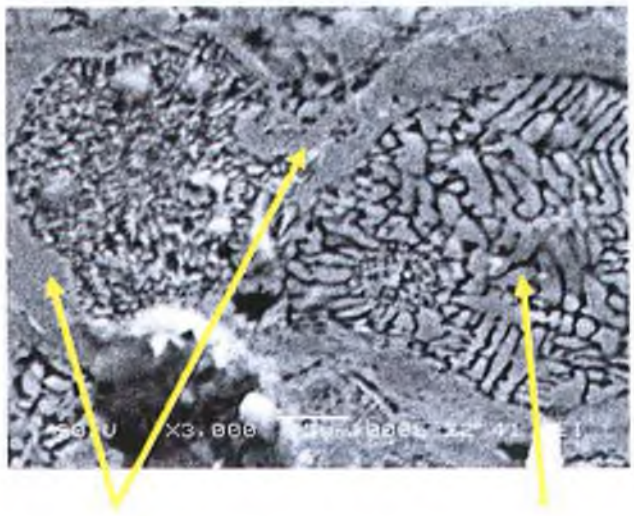

SEM micrograph

Figure 4.7-b Optical photograph and SEM micrograph of coating cross sectional showing splats and oxide formation around the splats.

This situation occurs mainly in chromium oxides. Consequently, elongated brittle oxides (stringers like oxides) enhance stress concentration and crack initiation [46]. Since the coated workpieces are annealed in the furnace at 735°C, small thickness of the oxide scale is formed at the free surface of the coating. This situation can be seen from Figure 4.8 in which XRD results are shown. Cr_2O_3 formation is evident from the corresponding peaks in XRD plot. Cr_2O_3 formation can be attributed to the oxide formation during coating prior to heat treatment, since the peak appears in both heat treated and untreated coatings. However, after the heat treatment process, Cr_2O_3 peaks become stronger. This indicates that Cr_2O_3 formation is enriched in the surface region during the heat treatment process. The α and θ aluminum oxide (Al_2O_3) peaks are also evident. Since the heights of the peak of aluminum oxide in the XRD spectrum corresponding to heat treatment and prior to heat treatment are the same, aluminum oxide formation during the heat treatment is less likely. Consequently, the existence of aluminum oxide is mainly because of the alumina particles left over from grit blasting prior to coating process.

Table 4.1 – EDS Analysis Results for the Coating Prior and After the Heat Treatment (wt%).

	C	O	Al	Ti	Cr	Co	Ni
Untreated	0.52	0.1	8.2	0.5	21,34	38.04	31,30
Heat Treated	0.51	4.2	5.93	0.6	21.29	35.83	31.64

Figure 4.9 shows *S-N* curve, alternating stress with number of cycles prior to fracture, for coated and uncoated as well as heat-treated coated and uncoated workpieces. Annealing heat treatment of Ti-6 Al-4V alloy results in low strength and high ductility and some improvement in fracture toughness occurs after heat treatment [22]. The life cycle of the heat-treated and uncoated workpiece is less than its counterpart corresponding to as-received workpiece. In this case, as received uncoated workpiece fails at 860 MPa for 40,000 cycles and as received and coated workpiece fails at 650 MPa for the same cycle. In addition, heat treated uncoated workpiece fails at 580 MPa for 40,000 cycles and heat treated coated workpiece fails at 443 MPa for the same cycle.

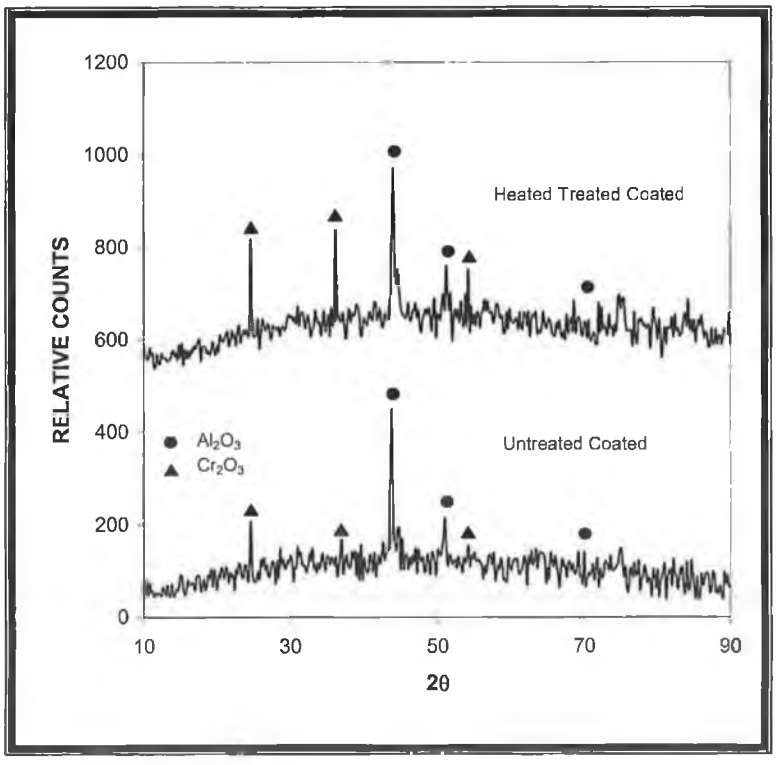

Figure 4.8- XRD results obtained for heat treated and untreated coated workpieces.

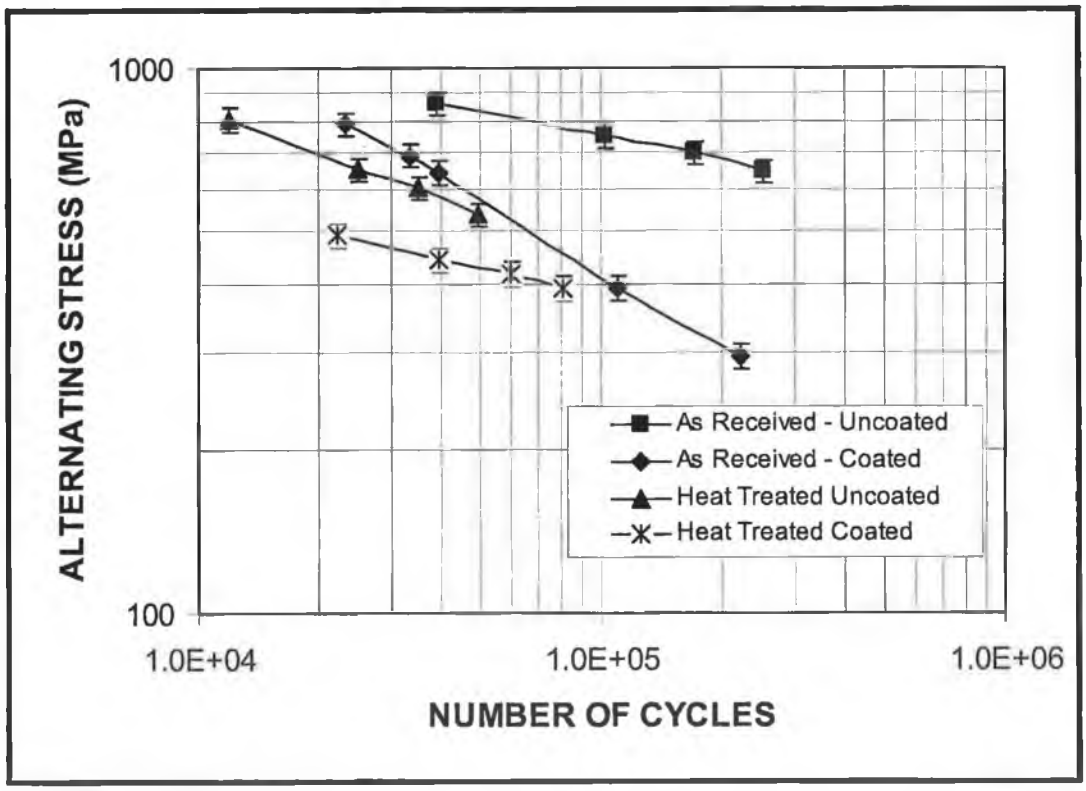

Figure 4.9 Logarithmic scale of alternating stress with number of cycles for different fatigue tested workpieces.

In this case, oxide formation in the surface vicinity of the annealed workpiece gives rise to brittle structure in the surface region. In addition, due to differences in thermal expansion coefficient of coating and the base substrate, thermally induced residual stress is formed at coating-base substrate interface. These are the main sources for early failure of the annealed workpiece. In general, the coating on the surface of the alloy enhances the fatigue life of the workpiece. Moreover, any cracking and coating failure due to local delamination results in reduction in the area of load carrying segments. This situation enhances the low fatigue life of the heat treated workpieces. As-received and coated workpiece results in highest fatigue strengths. This may be attributed to strong bonding between the coating and the substrate material. In this case, grit blasting modifies the substrate surface such that surface hardness improves and plastic deformation that takes place in the substrate surface vicinity. Similar observation was reported in the early studies [24] and [46]. Moreover, the particle impacting force and particle size most likely result in locally distributed compressive residual stresses concentrations in the surface region. Since the substrate surface was cleaned prior to thermal spray process, impurities left over after grit blasting . Therefore, the effect of impurities, captured between the coating and the substrate material, on the fatigue response of the coated workpiece is minimized. Moreover, as-received material (Ti-6Al-4V) is an α-phase colony structure composed of prime β grains. After annealing, the transformation results in the formation of β-phase and precipitation of α-phase [70]. However, the fatigue cracking starts at prior β-grain boundaries and/or colony boundaries as well as α/β interface [110]. The fatigue crack propagation rate of the annealed substrate having fine prior β-grains is faster than that of coarse β-grains (as as-received substrate). Consequently, fatigue failure of heat-treated workpiece is expected to be faster than the as-received workpieces. In addition

due to the differences in thermal expansion coefficient of the coating and substrate material, high concentration of residual stresses develop at the interface of the substrate material and coating after the heat treatment process. This gives rise to total failure of coating through delaminating or peeling off from the substrate surface during fatigue testing.

Table 4.2 gives the values of A and m, which are determined from Equation 3.5. The values of A is related to the fatigue strength coefficient of the workpiece while m represents fatigue strength exponent. It should be noted that A is associated with the true fracture stress due to static tensile test while m is the slope of the fatigue curve, which is associated with the fatigue life of the workpiece. Figure 4.10 shows the percentage of reduction in fatigue life for as received coated and coated heat treated workpieces as obtained from Equation 3.7. It is evident that heat treatment lowers significantly the fatigue life of the workpieces.

Table 4.2. The slope and coefficient obtained from equation 3.6 for each workpiece.

	A (GPa)	m
As Received - Uncoated	4.261981	0.1515
As Received - Coated	0.070845	0.4458
Heat Treated - Coated	2.669081	0.169
Heat Treated - Uncoated	11.24287	0.2809

Figure 4.11 shows SEM micrographs of cross-section of fractured surface of coating while Figure 4.12 shows optical photographs of top view of fractured workpieces. It is evident from SEM micrographs that partial elongated crack

occurs at fractured surface; in which case, coating is partially delaminated from the surface (Figure 4.11-b). This may be caused due to the presence of Cr_2O_3 in the coating, particularly in the surface region. The delamination of the coating takes place particularly in the surface region where oxide compounds locally scattered. In the case of heat-treated workpieces, multiple fracturing of coating as well as total failure of coating through peeling off from the substrate surface are evident Figure 4.11-c. This situation can be seen from optical photographs of the fractured surfaces (Figure 4.12). Therefore, heat treatment lowers the coating adherence to substrate material because of the residual thermal stresses developed due to mismatching of thermal expansion coefficients of coating and underneath substrate material. Cracks formed in the coating do not conform to the base material. Once the cracking is formed, the internal stresses are relaxed and the region of failure becomes limited. These results in the crack propagation in lateral direction normal to the direction of load applied during the tests. Moreover, oxygen diffusion in the free surface of coating during the heat treatment process results in high oxygen content in the surface region, which acts like a barrier preventing diffusion of oxygen further into the coating. Consequently, brittle structure mainly occurs in the region of the free surface of coating. Therefore, it is mostly likely that once the crack is initiated at the surface it expands in coating through splitting separation of brittle plates containing oxygen rich compounds. Once the crack is formed within the coating, crack extends towards the free surface of the coating due to formation of oxygen rich brittle structure in this region.

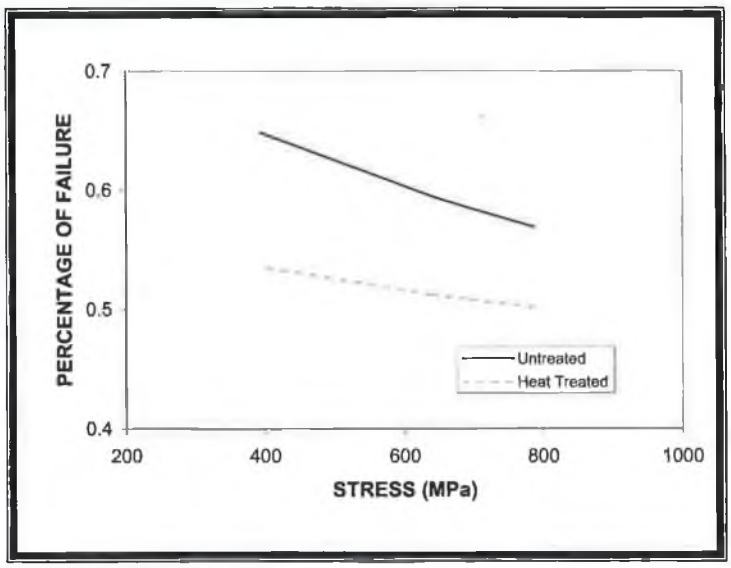

Figure 4.10. Percentage of fatigue failure with alternating stress for heat treated and untreated coated workpieces.

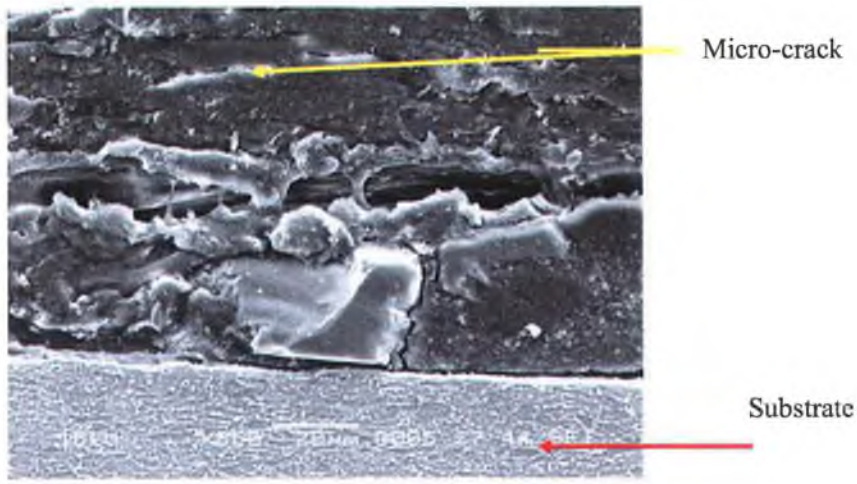

Figure 4.11a. SEM micrograph of cross-section of fractured coating after fatigue testing of untreated workpiece.

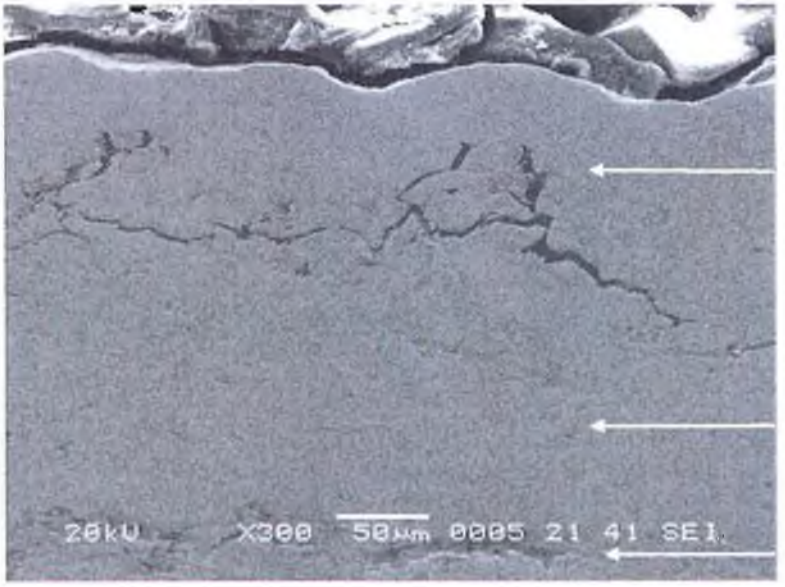

Figure 4.11-b SEM micrograph of cross-section of fractured coating after fatigue testing of heat treated workpiece.

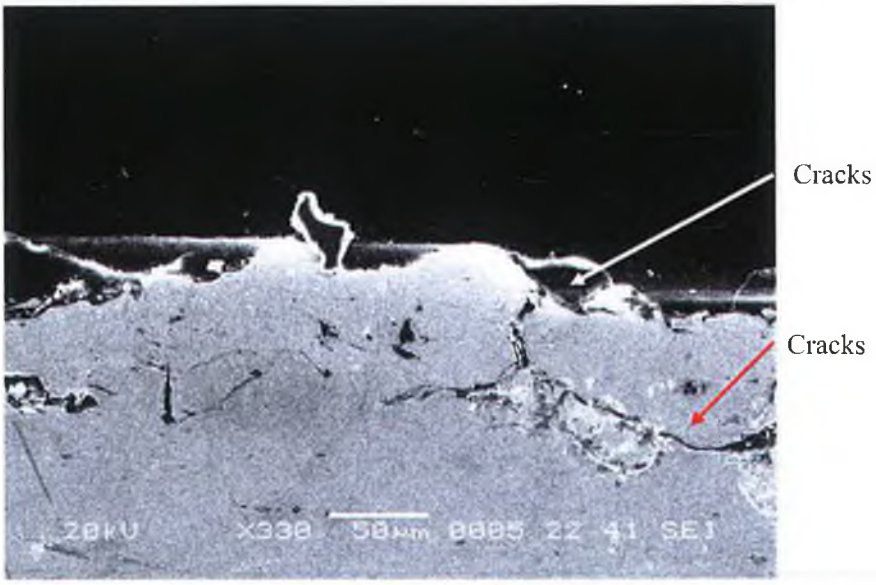

Figure 4.11-c SEM micrograph of cross-section of fractured coating after fatigue testing of heat treated workpiece. Fractured of coating in the surface region is evident.

Untreated coated workpiece.

Peeling of coating at the substrate surface

Figure 4.12. Optical photographs of fatigue tested workpieces.

4.3 Tensile Tests:

HVOF thermal spraying of AMDRY 995 onto Ti-6Al-4V alloy was carried out and tensile properties of coated and uncoated workpieces are examined. Some of the workpieces are heat treated at 735°C and tensile properties are compared with the untreated ones. Figure 4.7a shows micrographs of coated workpiece cross-sections before and after the heat treatment. In general, lamella-like structure is observed indicating the splats are in molten phase prior to impacting onto the workpiece surface. Moreover, some local near spherical shape particles are also evident. This shows locally distributed partially melted stacking particles in the coating. Stringers formation in the coating is the indication of highly oxided particles, which is particularly true for small size particles. In this case, small particles in-

flight gain considerable amount of oxygen before impacting onto the workpiece surface. This shows that the powder size has significant effect on the oxygen content in the coating, similar observation was reported earlier [40]. Oxygen content of the coating increases slightly in the surface region of the coating and this becomes small in the region across the coating and the workpiece interface. This occurs because of the oxygen diffusion into coating; in which case, once the oxygen content increased in the surface region, it forms like a barrier for further oxygen diffusion into the coating. Consequently, diffusional transport of oxygen is suppressed by the high oxygen content in the surface region.

Figure 4.13 shows tensile test results for coated workpieces as well as heat treated ones. In general, stiffness reduces slightly and elastic limit reduces for the coated workpieces subjected to the heat treatment (845 MPa). This is more pronounced for as the heat treated uncoated workpieces (815 MPa). In this case, heat treated workpieces results in longer elongation at high loads than that of as received as well as as received coated workpieces. The elastic limit of the as received workpiece is about 880 MPa (which is in agreement with the ASM data sheet [104]) while it is 890 MPa for the as received coated workpiece. It should be noted that small increase of oxygen content in the surface region after heat treatment results in modifying the elastic modulus of the coating; in which case, coating structure becomes brittle in the surface region. Consequently, elastic limit is reached at low applied tensile loads. The smooth appearance of the curves indicate that no crack initiation within the elastic limit of the coating occurs, i.e.,

local stress relieving due to poor coating, loose substrate interface, or coating defects in the surface region do not occur. It should be noted that when coating is fractured under the tensile load, internal stresses in the coating and at coating workpiece interface relaxes. If the energy used to disseminate the cracks is dissipated, secondary crack initiation and crack propagation cease. This, in turn, enhances the magnitude of rupture stress. Figure 4.14 shows micrographs of fractured workpiece cross-sections after the tensile tests. Delamination of coating from the crack site with partially attachment to the workpiece surface is observed. This indicates that tensile stress in the surface region of coating results in crack formation and delamination of the coating in this region.

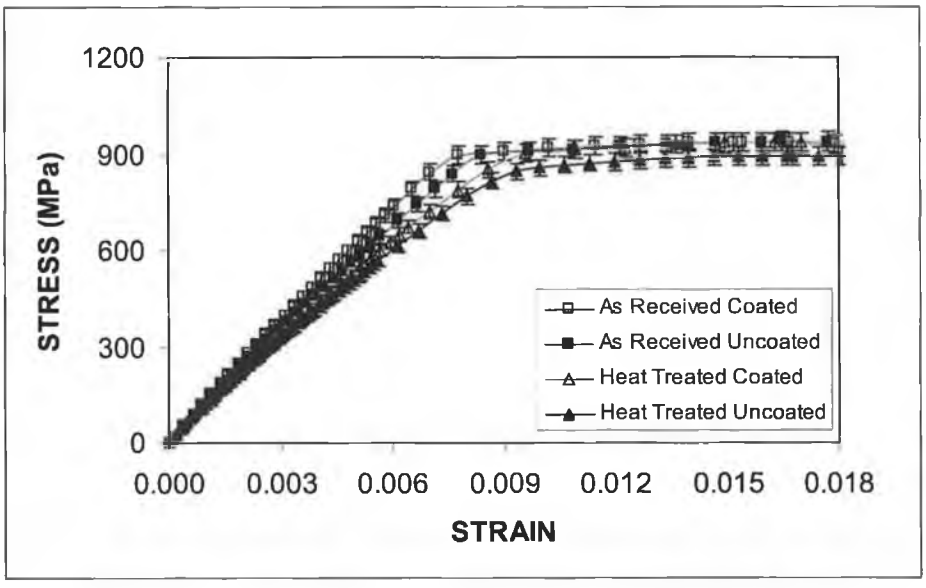

Figure 4.13 Tensile test results for as received uncoated, as received coated, heat treated uncoated and heat treated coated workpieces.

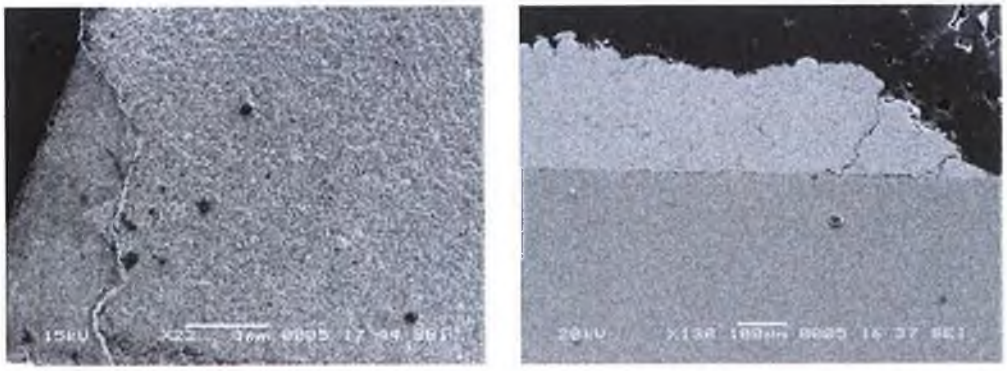

Top view of fractured coat

Cross-section of fractured coating.

untreated workpiece

heat treated workpiece

Figure 4.14 – View of fractured surfaces after the tensile tests.

Since the oxygen content of the coating is high in this region, brittleness of this region is responsible for crack initiation and delamination. In the case of heat-treated workpiece, total failure of coating is observed. This is mainly due to the differences between the coating and substrate material elastic modules, which are modified by the heat treatment process. Consequently, coat peels off from the surface once the elastic limit of the coating is reached during the tensile testing. Moreover, if coating is fractured and failed, internal stresses are relaxed and the region of failure does not extend into the coating in the direction of load applied in the tests. The multiple local crack formation in the vicinity of the coating surface is observed for some workpiece. This indicates that the coating splitting separation between layered columns in the coating occurs due to non-conforming the plastic deformation produced along the crack sites. Figure 4.14 shows optical photographs of fracture sites. It is clearly observed that total failure of coating occurs, particularly heat treated workpieces.

Figure 4.15 shows load displacement characteristics obtained from the tensile tests, which are used in the ANSYS simulations. It should be noted that the tensile curves are produced along the centerline between the coating and base material. It can be observed that both figures have the same trend in elastic and plastic regions, provided the maximum difference in loads corresponding the experiment and simulation for the same displacement is in the order of 10%. This maximum difference reduces to 5% in the plastic region. The elastic limit for the experiment is about 31 kN while it is 29 kN for the simulations. It should be noted in the simulation, the coating is considered as structurally homogenous with one unique

Young's modulus. In addition, the perfect adherence of coating to the base substrate material is assumed in the simulations. However, in the actual situation, the coating structure is non-uniform and the coating is formed through mechanical anchoring of the splats. The non-uniform oxygen content, voids, and micro-cavities at coating interface as well as non-uniform coating structure modifies the Young's modulus and tensile properties of the workpiece. This, in turn, results in differences in the tensile response of the workpice predicted from the FEM analysis and the experiment. Figure 4.16 shows von-Mises stress along x-axis (horizontal distance), y-location is centerline and z-location is at the workpiece-coating interface. von-Mises stress reaches maximum at the central region of the workpiece and decays sharply in the region next to the workpiece center. The maximum magnitude of von-Mises stress reaches close to the elastic limit of the substrate material. The flat top of the stress is evident of plastic deformation of the substrate material. Figure 4.17 shows von-Mises stress along the y-axis, x-axis location is workpiece center (x = 75 mm) and z-axis location is workpiece-coating interface. Similarly, flat top of von-Mises stress is evident of plastic deformation of the workpiece. Figure 4.18 shows von-Mises stress along z-axis (along thickness), x- and y-axes locations are the center of the workpiece. von-Mises stress rises sharply across the workpiece-coating interface, although the magnitude of stress is slightly less than that corresponding to workpiece. This results in rapid change of total strain in this region (Figure 4.19). Therefore, any residual stress formed during the coating process results in failure of the coating. This situation is observed during the tensile tests.

Figures 4.20a, 4.20b, 4.20c show contour plots of von-Mises stress inside as well as at the top and side surfaces of the workpiece. The top and side views are magnified and taken from the central region of the workpiece. Figures 4.21a, 4.21b, 4.21c shows total strain contours for the locations similar to von_Mises stress contours while Figures 4.21d, 4.21e, 4.21f shows the total plastic strain contours. It is evident that magnitude of von-Mises stress and total strain are maximum in the central region of the workpiece. The high magnitude of von-Mises stress extends in the axial (along the axis of the pulling force) and tangential (along the workpiece thickness) directions at an applied load of 30,400 N. In addition, total plastic strain is high in the central region of the workpiece. This indicates that early initiation of plastic deformation of the coating and workpiece material are unavoidable in this region. Moreover, the plastic deformation is regional rather than a local point on the workpiece. Once the early plastic deformation is initiated at low applied loads, the deformation takes place in a large section in the central region of the workpiece. Consequently, the coating failure results in multiple cracks as observed from the SEM micrographs (Figure (4.14)).

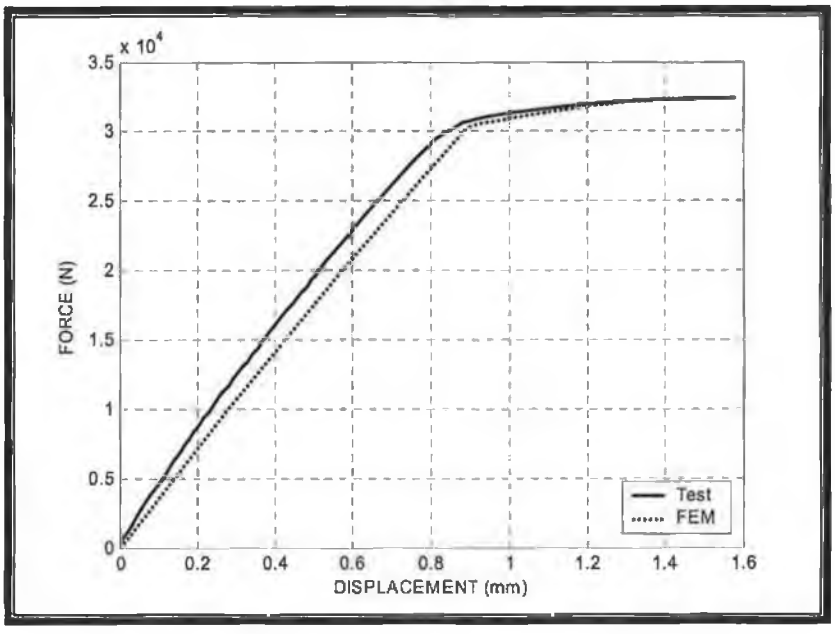

Figure 4.15 Load displacement characteristics obtained from tensile testing and used in FEM simulations.

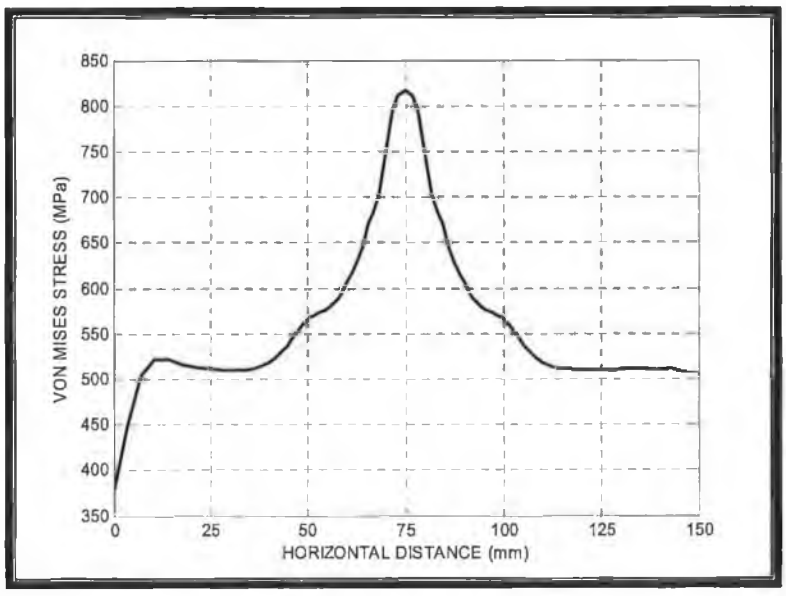

Figure 4.16 von-Mises stress along the x-axis (horizontal distance) at coating workpiece interface (Force = 30,400 N).

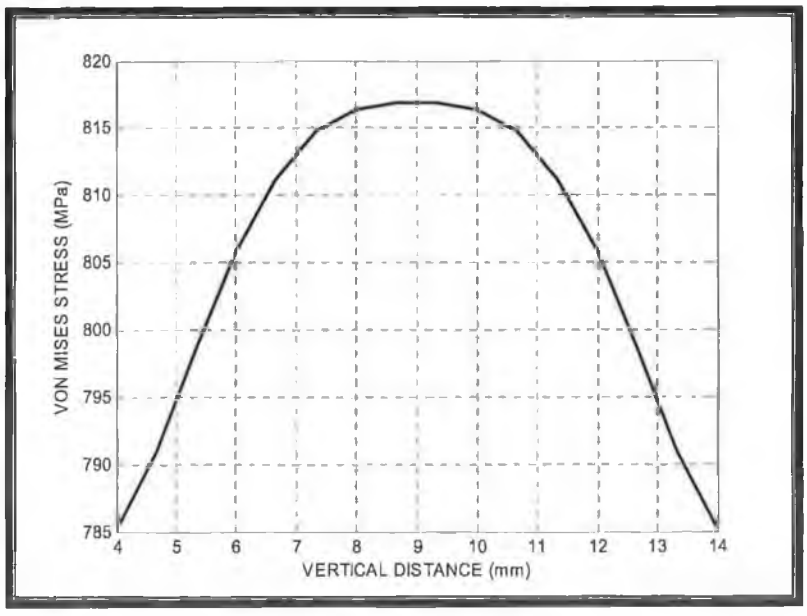

Figure 4.17. von-Mises stress along the y-axis (vertical distance) at coating workpiece interface (Force = 30,400 N).

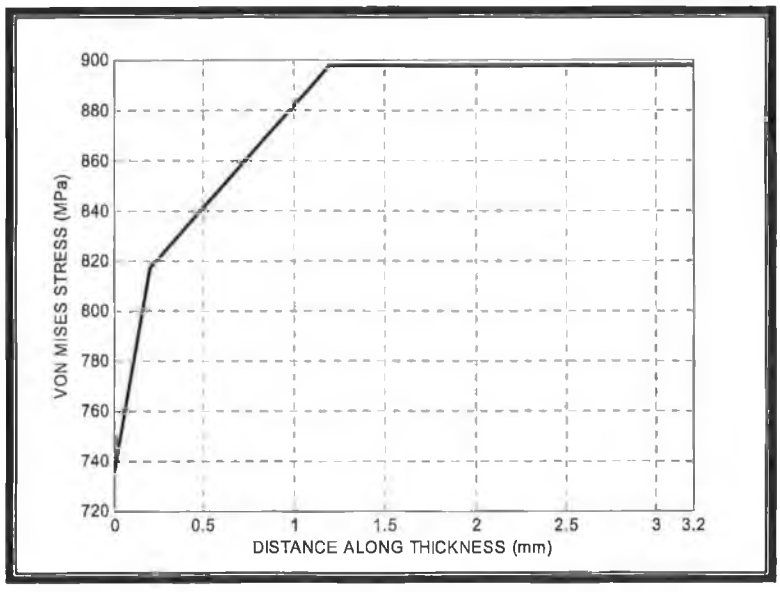

Figure 4.18 von-Mises stress along the z-axis (distance along thickness) across the coating and workpiece (Force = 30,400 N).

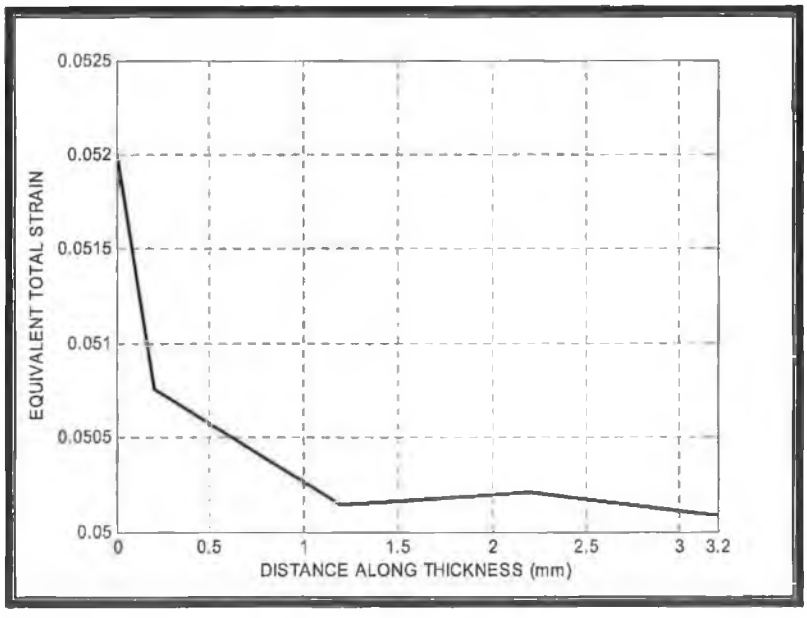

Figure 4.19 Equivalent total strain along the z-axis (distance along thickness) across the coating and workpiece (Force = 30,400 N).

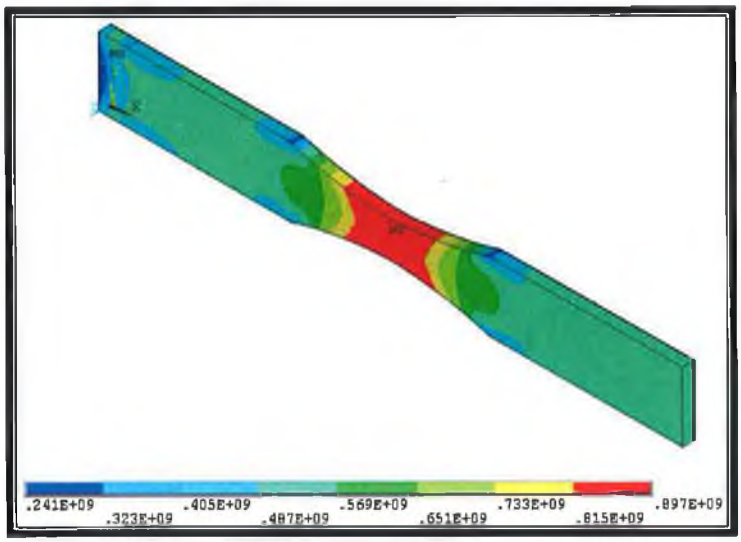

Figure 4.20a Three-dimensional contour plot of von-Mises stress in the workpiece (Force = 30,400 N). Stress unit is in Pa.

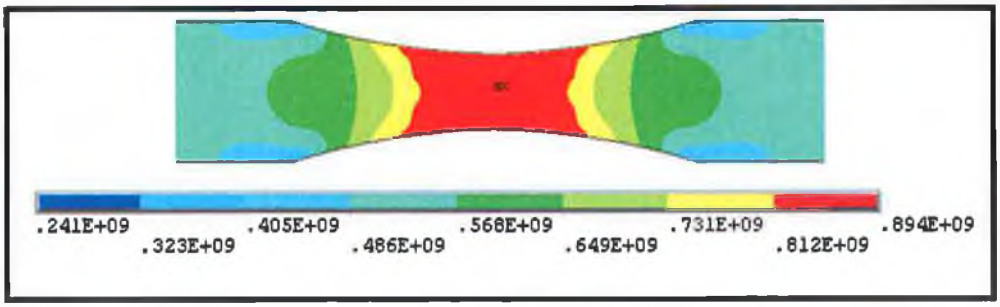

Figure 4.20b Two-dimensional contour plot of von-Mises stress (at the top view of the workpiece surface) (Force = 30,400 N). Stress unit is in Pa.

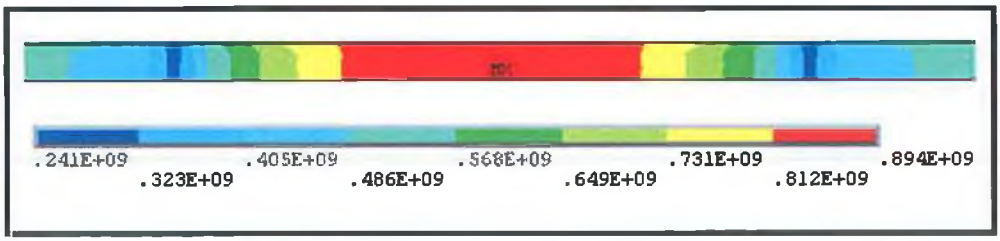

Figure 4.20c Two-dimensional contour plot of von-Mises stress (at the side view of the workpiece surface) (Force = 30,400 N). Stress unit is in Pa.

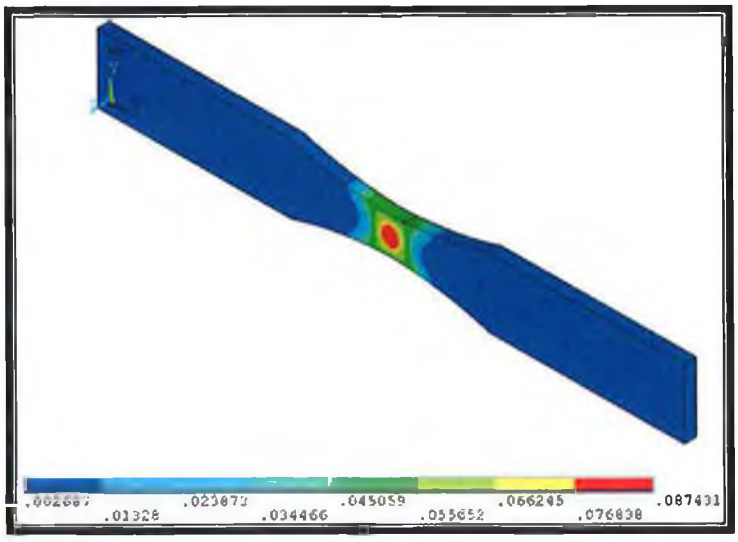

Figure 4.21a Three-dimensional contour plot of equivalent total strain in the workpiece (Force = 30,400 N).

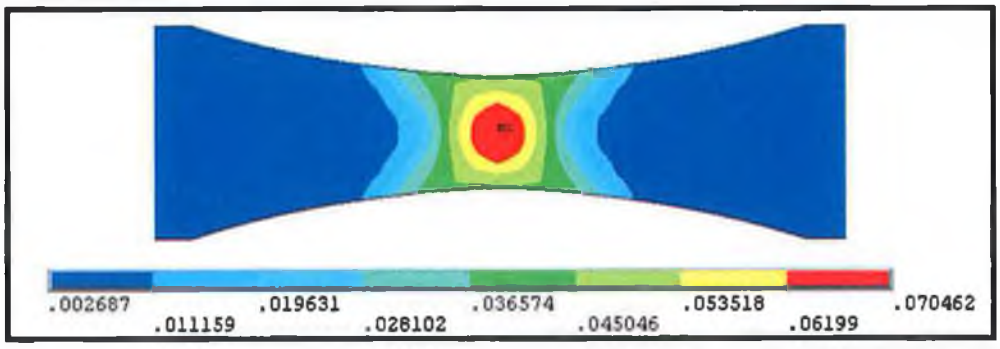

Figure 4.21b Two-dimensional contour plot of equivalent total strain (at the top view of the workpiece surface) (Force = 30,400 N).

Figure 4.21c Two-dimensional contour plot of equivalent total strain (at the side view of the workpiece surface) (Force = 30,400 N).

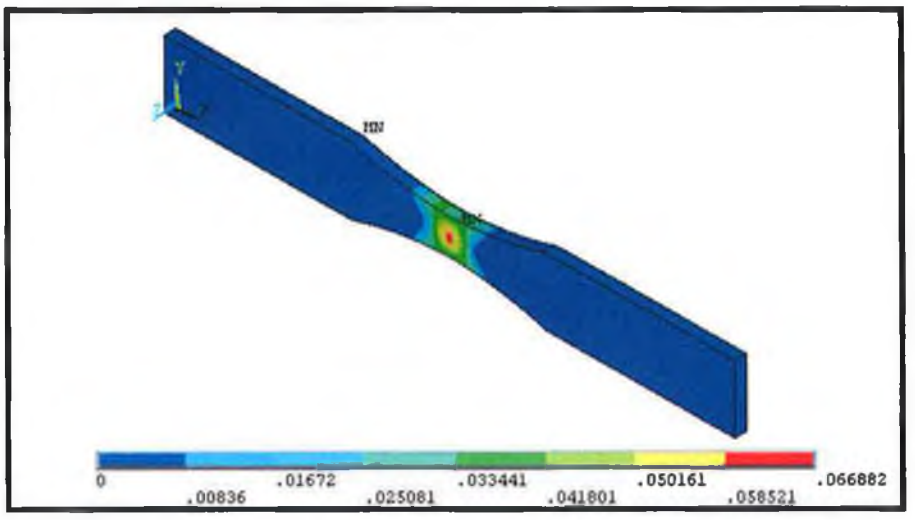

Figure 4.21d Three-dimensional contour plot of equivalent plastic strain in the workpiece (Force = 30,400 N).

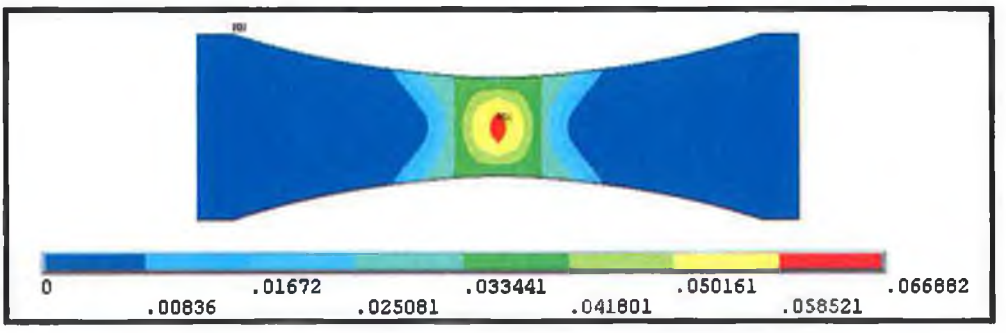

Figure 4.21e Two-dimensional contour plot of equivalent plastic strain (at the top view of the workpiece surface) (Force = 30,400 N).

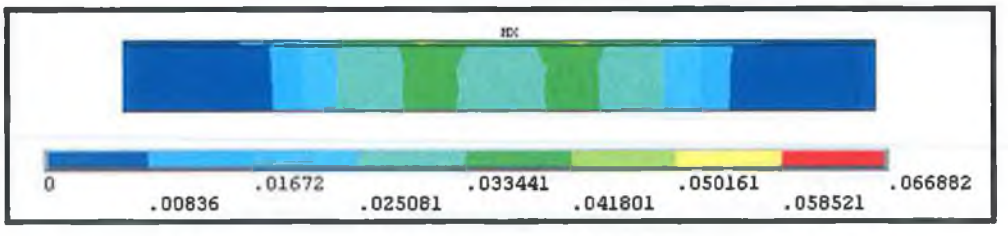

Figure 4.21f Two-dimensional contour plot of equivalent plastic strain (at the side view of the workpiece surface) (Force = 30,400 N).

4.4 Fracture Toughness Measurement

HVOF coating of AMDRY 995 on Ti-6Al-4V alloy is carried out and Young's modulus as well as fracture toughness of coating is measured using three point bending and indentation tests. The workpieces coated was heat treated at annealing temperature of the base material for one hour prior to indenting tests.

Figure 4.22 shows the micrographs of coating before and after the heat treatment process. In general, lamella-like structure is observed and existence of some round shaped splats in coating indicates that some of the splats are in partial molten state prior to impacting at the surface. Oxidation of splats is evident particularly at the location close to the surface region of the coating, which is more pronounced for heat treated surface. This situation can be observed from Table 4.1, in which the elemental composition of the coating prior and after the heat treatment is given as reference to Figure 4.22. In this case, oxygen diffusion enhances the oxygen content in the coating. Moreover, once the oxygen content in the coating surface region becomes high, then, oxygen diffusion further into the coating reduces due to saturation of oxygen content in the surface region. EDS line scan around the splat boundary (Figure 2.23) shows that enrichment of oxygen, chromium, and aluminum occurs within the splat boundary. Consequently, oxidation mainly takes place within the surface region of the splat which was also indicated in the previous study [40]. Chromium and aluminum enrichment at splat boundary indicates the formation of chromium and aluminum oxides.

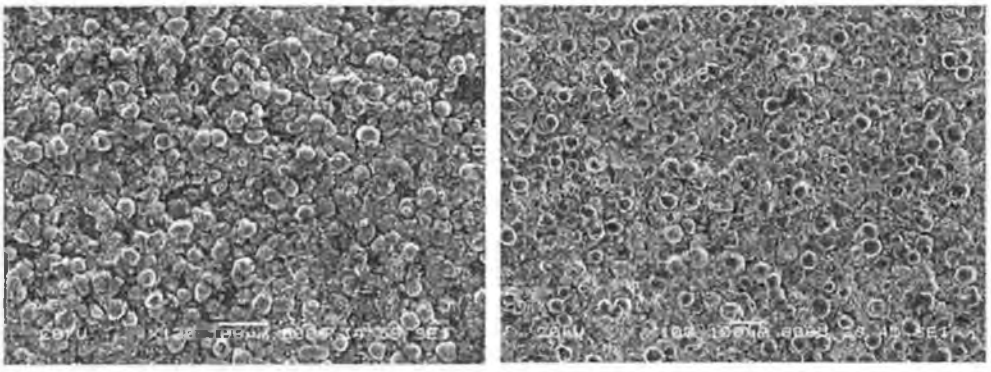

Before heat treatment. After heat treatment.

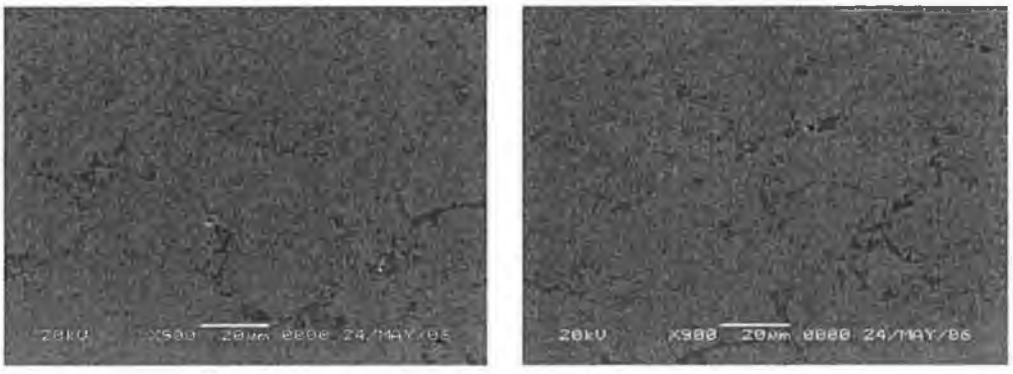

Before heat treatment. After heat treatment.

Figure 4.22. Top and cross-sectional views of coating before and after heat treatment.

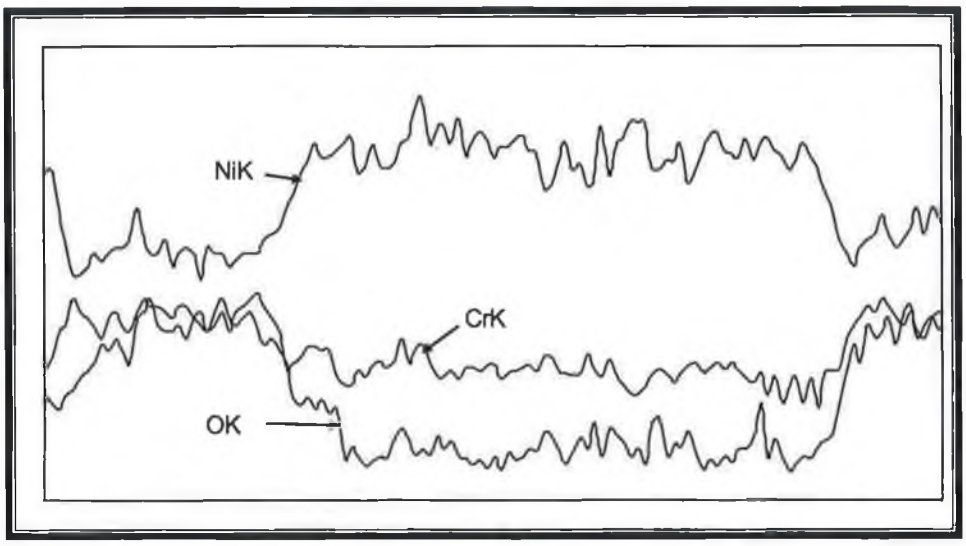

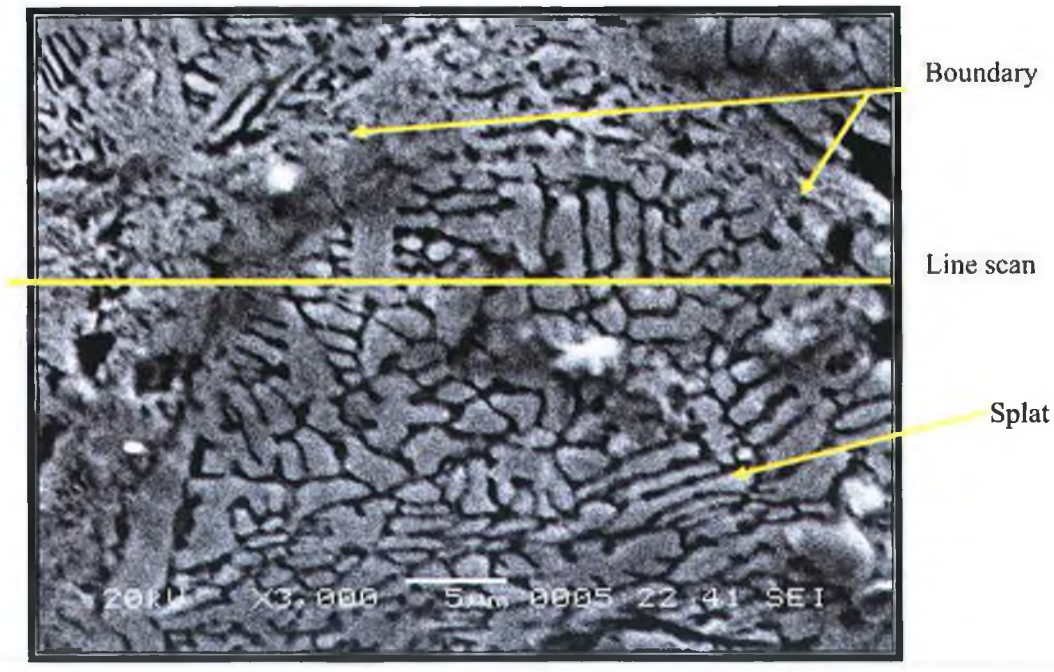

Figure 4.23 – EDS line scan across the splat and its boundary.

Table 4.3 gives the Young's modulus and fracture toughness of the AMDRY 9954 coatings prior and after the heat treatment. The Young's modulus obtained from three-point bending tests for uncoated substrate and data obtained from literature [105] are in good agreement. Moreover, Young's modulus of the coatings determined from three-point bending tests and indention tests are in good agreement. However, heat treatment modifies the Young's modulus, in which case it reduces. Untreated substrate material, which is Ti-6Al-4V, is an α-phase colouring structure composed of prime β grains. Moreover, β-phase formation and α-phase precipitation is resulted due to the annealing process. In bending tests, β-phase transformation lowers the toughness of the workpiece and load displacement characteristics, which differ than that of untreated material. This situation is seen from Figure 4.1, in which three-point bending test results are shown. In addition, thermal stresses developed during the heat treatment process results in brittle structure in the surface region of the coating due to high rate of oxygen diffusion taking place in this region. Consequently, the crack formation initiates in the surface region and extends towards the coating. However, the multiple crack initiation in the surface region of the coating relaxes the stresses in this region. Once the crack formed extends in the coating, particularly, reaching the interface of coating-base material, the coating integrity fails and it peels off from the base material surface (Figure 4.24), i.e., total failure is resulted. The indentation marks are shown in Figure (4.25), where the multiple crack sites are evident. The fracture toughness obtained for the coatings subjected to the heat treatment is less than that of untreated coatings. This is because of the high oxide content in the surface region of the coating, which in turn results in a brittle structure. In addition, low

Young's modulus of the coating is also responsible for less fracture toughness of heat treated workpieces.

Table 4.3. Young's Modulus of the coatings obtained from Three Point Bending and Indention Tests.

	Three Point Bending Tests (GPa)	Indention Tests (GPa)	Fracture toughness ($N/m^{3/2}$)
As Received coated	346	341	$1.36x10^7$
Heat Treated coated	125	142	$6.51x10^6$

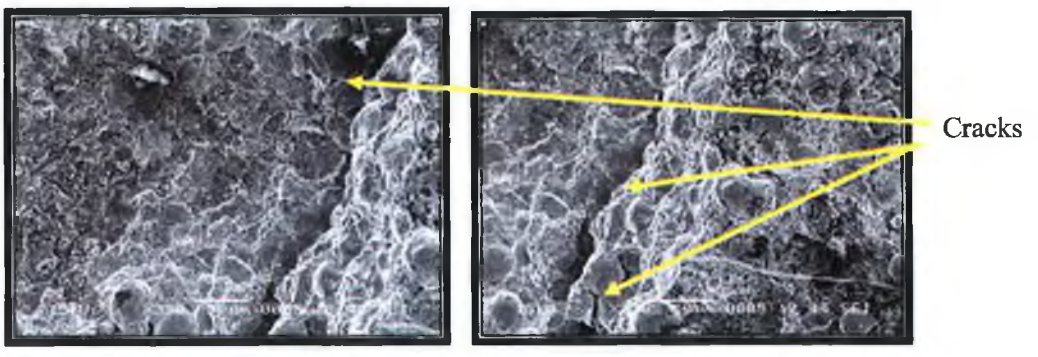

a)Top view of coating after tests b)Top view of heat treated coating after tests

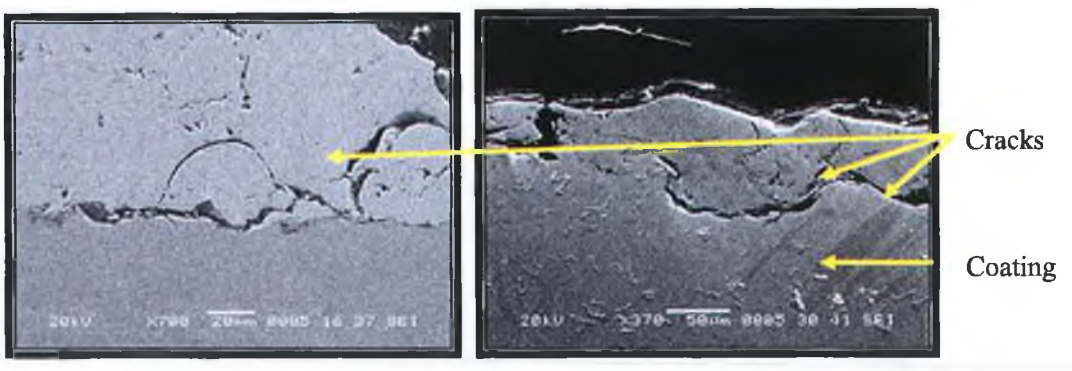

c)Cross-section of coating after tests d)Cross-section of heat treated after tests

Figure 4.24 SEM micrographs of cracks formed in the coating after the bending tests. Cracks are in the surface region for heat treated coatings due to brittleness.

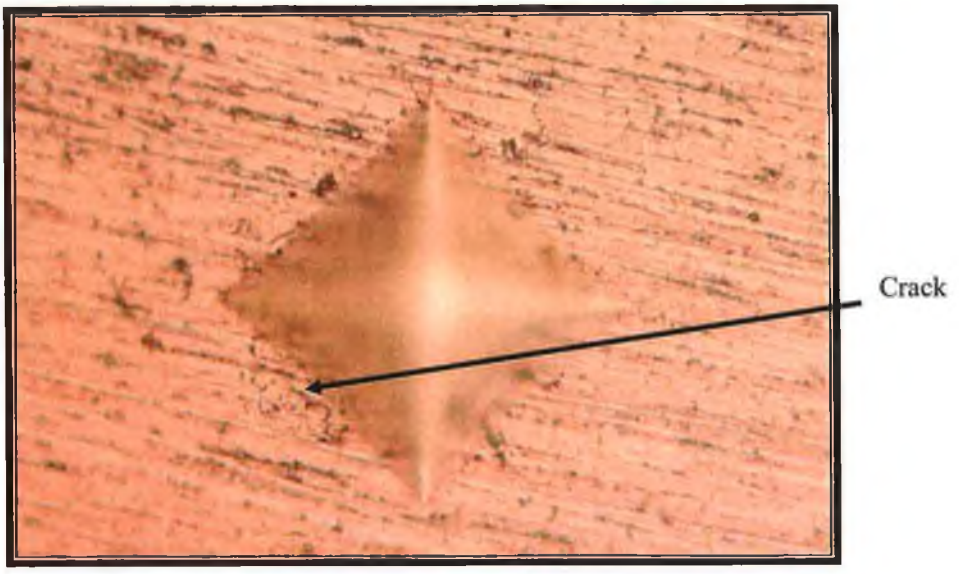

As Received Coating

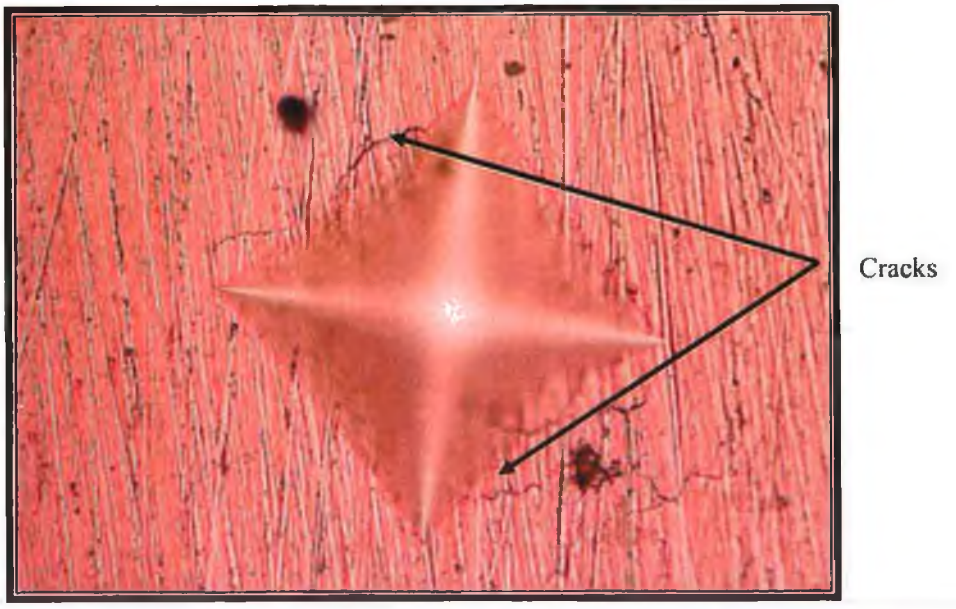

Heat Treated Coating

Figure 4.25 Indention marks on the surface of the coating prior and after heat treatment

Chapter 5 - Conclusions and Future Work

In the present study, HVOF coating of AMDRY 9954 ($Co_{Bal.}Ni_{32}Cr_{21}Al_8Y_{0.5}$) powders on Ti-6Al-4V alloy is considered. Mechanical properties of coating interface are examined through three-point bending, tensile, fatigue, and indentation tests. The bending and tensile test conditions are simulated using the finite element method (FEM) and stress fields in the coatings as well as across the coating-base substrate material are predicted numerically. In order to investigate the metallurgical changes before and after the mechanical tests, SEM is carried out. The study is extended to include post-heat treatment; in which case, the changes in mechanical and metallurgical properties in coating are investigated due to post-thermal processing prior to bending tests. The conclusions are classified according to the tests carried out in the present work. Therefore, the findings are given under the following test headings

Three Point Bending Test

Three-point bending tests are carried out to examine the tensile-shear response of the coating under the bending load. The study is extended to include the heat treatment of the workpieces after the coating process prior to three-point bending tests. It is found that coating with small porosity and voids is achieved. Elongated

cracks are developed in the coating in the region of deflection of the workpiece during the bending tests. This, in turn, results in partial attachment of the coat onto the base material without complete peeling off from the substrate surface due to stress relaxation at coating interface. This situation is also observed from optical photographs. However, the coating with severe crack formation and total peeling off from the substrate surface are also observed, which is more pronounced for heat treated workpieces.

High stress concentration occurs within the bending region of the workpiece. von-Mises stress in excess of elastic limit at coating-base material interface extends in the horizontal direction, which indicates that the crack formation in coating is unavoidable. As the load level increases, elongated cracks are formed in the coating, particularly in the region of maximum deflection. Once the cracks are formed, stress relaxation at coating interface occurs, which reduces the strain in this region and the cracks do not propagate into the base material. In the simulations, it is assumed that the workpiece is free from any stresses and the coating base material adherence is in perfect conditions. In the real situations, the residual stress is developed in the coating and the coating adherence to the base material is not perfect. Consequently, FEM predictions provide the qualitative information on the strain and stress field during the bending.

Fatigue Test

Fatigue testing is carried out prior and after heat treatment process. It is found that coated workpieces without heat treatment result in higher fatigue life than heat treated workpieces without coating. This is attributed to the strong adherence of coating to the substrate material and grit blasting prior to coating. In this case, grit blasting cause local residual stress centers which improve the fatigue strength of the workpiece. It should be noted that HVOF coating does not always enhance the fatigue life. Moreover, heat treatment process lowers the fatigue strength of both as-received and coated workpieces. This is mainly because of the formation of β-phase and precipitation of α-phase inside the β-phase; in which case, fatigue crack initiation and propagation start early periods of testing. Heat treatment process enhances oxygen content in the surface vicinity of coating, which in turn increases the brittleness of coating in this region. Consequently, failure of coating initiates either at oxide compounds boundaries in the coating or Al_2O_3 particles left over from the grit blasting at coating-substrate interface prior to coating.

Due to the differences in thermal expansion coefficients of coating and the underneath substrate material, thermally-induced residual stresses are developed at coating-substrate interface after the heat treatment process. This situation causes total failure of coating through peeling and spalling of coatings from the substrate surface during the testing. In the case of coated workpieces, without heat treatment, cracks are initiated in the brittle sites, such as Cr_2O_3 within the coating.

This, in turn, results in partial delamination of coating with part of the coating remaining on the substrate surface.

Tensile Test

Tensile properties of the coated workpieces is examined and in order to simulate the working conditions of gas turbine, some of the coated workpieces are heat treated at 735°C prior to tensile tests. It is found that coating with small scattered porosity is achieved. Lamellae structure in coating suggests the almost molten state of powder is reached prior to impacting onto substrate surface.

Oxygen content in the coating changes after the heat treatment. In this case, oxygen content in the surface region of the coating enhances due to oxygen diffusion during the heat treatment. However, oxygen content in the coating in the region close to the coating workpiece interface does not change significantly after the heat treatment process. Tensile test results reveal that stiffness of heat treated workpieces reduces slightly resulting in low load and long elongation in the elastic limit. Early crack initiation is not observed from tensile response of the coating. Since the oxygen content is high in the region of coating surface, delamination of coating with some coating adherence to workpiece surface is observed. In the case of heat treated workpieces total failure of coating is resulted despite the fact that the oxygen content at coating substrate material interface is not influenced by the heat treatment process. Consequently, heat treatment modifies the elastic modulus

of the coating so that total internal stress developed at coating workpiece interface results in total failure of the coating after the tensile tests.

The results of ANSYS simulations reveal that stress level changes drastically across the workpiece-coating interface, which in turn results in failure of coating at interface. This situation is also observed during the tensile experiments. However, due to the assumptions made in the FEM simulations, such as perfect adherence of the coating to the base substrate, uniform elastic modulus, and structural integrity and uniformity, the predictions provide qualitative information on the strain and stress fields during the tensile testing.

Fracture Toughness Measurement

Indentation and three-point bending tests are carried out to determine the fracture toughness of the coatings prior and after the heat treatment process. It is found that the heat treatment influences significantly the load-displacement characteristics of the coated workpieces. In this case, β-phase transformation and α-phase precipitation in the base material after the heat treatment lowers the Young's modulus. Young's modulus determined from bending tests and indention tests are in good agreement. In addition, oxygen diffusion in the surface region of coating after the heat treatment enhances chromium and aluminum oxide formations in this region. The brittle oxides act as the crack initiation sites under the bending load.

Consequently, multiple crack initiation at the surface is resulted and once the crack reaches the interface of coating-base material, total failure occurs. Fracture toughness of coating reduces after the heat treatment process due to high level of oxidation in the surface region of the coating.

FUTURE WORK

In this work, mechanical properties of the AMDRY 9954 HVOV coated onto a Ti-6Al-4V substrate were examined in details. However, the heat transfer from the coating to the substrate material (Ti-6Al-4V) during the thermal spraying process limits the mechanical response of the coated workpieces. This is because of the low annealing temperature of Ti-6Al-4V alloy (735 ^{o}C). This situation can be improved through gradual spraying (stepwise by time) of coating onto the substrate material; in which case, after one pass of HVOF spraying, thin layer of coating is left for cooling. The spraying can, then, be repeated onto the initially formed thin coating layer. The process continues until the desired thickness of coating is achieved. This stepwise spraying process may result in non-homogeneous structure formed in the coating. Therefore, metallurgical and mechanical response of the stepwise sprayed coating needs to be examined for possible adaptation of the spraying process in the field applications. In addition, in the case of the large voids and porosity formation in the coating due to the stepwise spraying, the thermal integration of the coating through control melting can be applied. This reduces the

structural defects such as porosity and in homogeneity in the splat size and distribution in the coating as well as improves the compactness of the coating. Therefore, investigation into the thermal integration of such coating becomes important. However, the control melting of the coating is possible through using a scanning laser beam source. High power laser irradiation provides high speed processing with controlled melting. Consequently, in the future work, the model studies determining the melt depth in terms of the laser process parameters become essential. The predictions as well as the measurement of residual stresses prior and after the laser processing give useful information about the effect of laser control melting on the coating stress levels. In addition, metallurgical examination of the laser treated coating will provide insight into the structural changes in the coating after the laser treatment process. The mechanical properties of laser treated coating can be assessed through tensile, three-point bending, and fatigue tests.

REFERENCES

[1] ASM handbook, volume 6 hard facing, Weld Cladding, and Dissimilar Metal thermal spraying by Joining J.R. Davis, Davis & Associates, 1993.

[2] www.hvof.com/, NATIONAL THERMOSPRAY, INC. 5120 Oak Ave, Pasadena, Texas 77503, 2007

[3] www.sulzermetco.com/en/desktopdefault.aspx/tabid-2008//3390_read-5302,2007

[4] http://www.gordonengland.co.uk/hvof.htm, 2007

[5] H. Y. Al-Fadhli, Performance evaluation of (HVOF) thermal sprays coating using Inconel-625 powder. 2003, MSc. Thesis, Mechanical Engineering Department, King Fahd University of Petroleum and Minerals, Saudi Arabia.

[6] Thermal spraying technical paper, www.airproducts.com, 2007

[7] J. Stokes, The theory and application of HVOF thermal spray process, http://webpages.dcu.ie/~stokesjt/ThermalSpraying/Book, 2007

[8] DYNAMIC-CERAMIC LTD Crewe Hall, Weston Road, Crewe, CW1 6UA England, http://www.dynacer.com/coatings.htm#High, 2007

[9] Pollution Prevention in the Plating Process, Metal Finishing Industry, Illinois Waste Management and Research Center, One Hazelwood Dr.Champaign, IL 61820, http://www.wmrc.uiuc.edu/main_sections/

[10] G. Thurn, G. A. Schneider, H. A. Bahr, and F. Aldinger, Toughness anisotorpy and damage behavior of plasma sprayed ZrO_2 thermal barrier coarings, *Surface and Coatings Technology*, **123**, 2000, pp.147-158.

[11] A.F.M. Arif, and B.S. Yilbas, The three-point bend testing of HVOF inconel 625 coating: FEM simulation and experimental investigation, surface and coating technology, 201, 2006, 1873-1879.

[12] N. Roy, K. M. Godiwalla, S. Chaudhuri, and A. K. Ray, Simulation of bond coat proprties of thermal barrier coatings during bending, High Temp. Mater. Process , **20**(2), 2001, pp.103-116.

[13] H. Hamatani, Y. Ichiyama, and J. Kobayashi, Mechanical and Thermal Properties of HVOF Sprayed Ni-based Alloys with Carbide, *Science and Technology of Advanced Materials*, **3**(4), 2002, 319-326.

[14] T. C. Totemeier, R. N. Wright, and W. D. Swank, Mechanical and Physical Properties of High-Velocity Oxy-Fuel-Sprayed Iron Aluminide Coatings, *Physical Metallurgy and Materials Science, Transactions of Metallurgical and Materials*, **34A**(10), 2003, 2223-2231.

[15] G. Burkle, F. Banhart, A. Sagel, C. Wanke, G. Corrpnick, and H. J. Fecht, Determination of the Mechanical Properties of Nanocrystalline Fe-Cr-based Thermal Spray Coatings, *Materials Science Forum*, **386**(3), 2002, 571-576.

[16] R. Ahmed, Contact Fatigue Failure Modes of HVOF Coatings, *Wear*, **253**, 2002, 473-487.

[17] R. T. R. McGrann, D. J. Greving, J. R. Shadley, E. F. Ryblckl, B. E. Bodger, and D. A. Somerville, The effect of residual stress in HVOF tungsten carbide coatings on the fatigue life in bending of thermal spray coated aluminum, *Journal of Thermal Spray Technology*, **7**, 1998, 546-552.

[18] X. Q. MA, Y. Mizutani, and M. Takemoto, Laser induced surface acoustic waves for evaluation of elastic stiffness of plasma sprayed materials, Journal of material science, **36**, 2001, 5633-5641.

[19] P. Poza and P. S. Grant, micro structure evaluation of vacuum plasma sprayed CoNiCrAlY coatings after heat treatment and isothermal oxidation, *Surface and Coatings Technology*, **201**, 2006, 2887-2896.

[20] J. Oh, N. J. Kim, S. Lee, and L. W. Eui, Correlation of Fatigue Properties and Microstructure in Investment Cast Ti-6 Al-4 V Welds, *Materials Science and Engineering*, **A340**, 2003, 232-242.

[21] L. Hernández, F. Oliveira, J. A. Berríos, C. Villalobos, A. Pertuz, and E. S. Puchi Cabrera, Fatigue Properties of a 4340 Steel Coated with a Colmonoy 88 Deposit Applied by High-Velocity Oxygen Fuel, *Surface and Coatings Technology*, **133-134**, 2000, 68-77

[22] K. Padilla, A. Veláquez, J. A. Berrios, E. S. Puchi Cabera, Fatigue behavior of a 4140 steel coated with a NiMoAl deposit applied by HVOF thermal spray, *Surface and Coatings Technology*, **150**, 2002, 151-162.

[23] A. Ibrahim, and C. C. Berndt, The Effect of HFPD Thermally Sprayed WC-Co Coatings on the Fatigue Behavior and Deformation of Al 2024-T4, Proceedings of the International Thermal Spray Conference, 2000, 1297-1301.

[24] O. C. Brandt, Mechanical Properties of HVOF Coatings, *Journal of Thermal Spray Technology*, **4**(2), 1995, 147-152.

[25] H. Y. Al-Fadhli, J. Stokes, M. S. J. Hashmi, and B. S. Yilbas, HVOF coating of welded surfaces: Fatigue and corrosion behaviour of stainless steel coated with Inconel-625 alloy, *Surface and Coatings Technology*, **200**(16-17), 2006, 4904-4908

[26] F. Oliveira, L. Hernández, J. A. Berríos, C. Villalobos, A. Pertuz, and E. S. Puchi Cabrera, Corrosion-fatigue properties of a 4340 steel coated with Colmonoy 88 alloy, applied by HVOF thermal spray, *Surface and Coatings Technology*, **140**, 2001, pp.128-135.

[27] V. Higuera Hidalgo, J. Belzunce Varela, A. Carriles Menendez, and S. Poveda Martinez, Experimental study effects of thermal spray procedure and thermal fatigue on microstructure and properties of NiCrAlMoFe coating, *Surface Engineering*, **17**(6), 2001, 512-517.

[28] S. De Palo, M. Mohanty, H. Marc-Charles, and M. Dorfman, Fracture Toughness of HVOF Sprayed WC-Co Coatings, Thermal Spray: Surface Engineering Via Applied Research, Proceedings of the 1st International Thermal Spray Conference, Montreal, Canada, Editor(s): Christopher C. Berndt, 2000, 245-250.

[29] H. Li, K. A. Khor, and P. Cheang, Young's modulus and fracture toughness determination of high velocity oxy-fuel-sprayed bioceramic coatings, *Surface and Coating Technology*, **155**, 2002, 21-32.

[30] F. Otsubo, H. Era, T. Uchida, and K. Kishitake, Properties of Cr_3C_2-NiCr cermet coating sprayed by high power plasma and high velocity oxy-fuel processes, *Journal of Thermal Spray Technology*, **9**(4), 2000, pp.499-504.

[31] A. H. Dent, A. J. Horlock, S. J. Harris, and D. G. McCartney, Enhanced wear resistant nickel-based alloy coatings produced by high velocity oxy-fuel spraying, *Trans. IMF*, **77**(2), 1999, pp.60-63.

[32] J. He, M. Ice, and E. Lavernia, Particle melting behavior during high-velocity oxygen fuel thermal spryaing, *Journal of Thermal Spray Technology*, **10**(1), March 2001, pp.83-93.

[33] A. J. Horlock, D. G. McCartney, P. H. Shipway, and J. V. Wood, Thermally sprayed Ni(Cr)-TiB_2 coatings using powder produced by self-propagating high temeprature synthesis: microstructure and abrasive wear behavior, *Materials Science and Engineering*, **A336**, 2002, pp.88-98.

[34] G. Bürkle, H. J. Fecht, A. Sagel, and C. Wanke, Dynamic mechanical analysis of the mechanical properties of Al- and Fe-based thermal spray coatings, Thermal Spray 2001: *New Surfaces for a New Millennium*, Ed. C. C. Brandt, K. A. Khor, and E. F. Lugscheider, ASM International, Ohio, USA, 2001.

[35] L. Gil, and M. H. Staia, Microstructure and properties of HVOF thermal sprayed NiWCrBSi coatings, *Surface and Coatings Technology*, **120-121,** 1999, pp.423-429.

[36] Y. Liu, Y. Qiao, J. He, E. J. Lavernia, and T. E. Fischer, Near-nanostructured WC-18 Pct Co coatings with low amounts of non-WC carbide phase: Part II. Hardness and resistance to sliding and abrasive wear, *Metallurgical and Materials Transactions A*, **33A**, January 2002, pp.159-164.

[37] W. C. Oliver, and G. M. Pharr, Improved technique for determining hardness and elastic modulus using load and displacement sensing indentation experiments, *Journal of Materials Research*, **7**, 1992, 1564-1580.

[38] B. H. Kim, and D. S. Suhr, The influence of fuel/oxygen ratio in HVOF spraying on the deposition of Cr_3C_2 coatings, Mater Trans JIM **41**(12),2000 pp.1657-1662.

[39] S. Ahmaniemi, P. Vuoristo, and T. Mäntylä, Improved sealing treatments for thick thermal barrier coatings, *Surface and Coatings Technology*, **151-152**, 2002, pp.412-417.

[40] C. J. Li, W. Li, Effect of sprayed powder particle size on the oxidation behavior of MCrAlY materials during high velocity oxygen-fuel deposition, *Surface and Coatings Technology*, **162**, 2002, 31-41.

[41] S. Nuutinen, P. Vuoristo, S. Ahmeniemi, T. Mantyla, and J. A. Takeuchi, Microstructural Study of HVOF and VPS Sprayed MCrAlY Coatings Proceedings of the International Thermal Spray Conference, 2001, 661-670.

[42] J. A. Hearley, J. A. Little, and A. J. Sturgeon, The effect of spray paramters on the properties of high velocity oxy-fuel NiAl intermetallic coatings, *Surface and Coatings Technology*, **123**, 2000, pp.210-218.

[43] L. Pejryd, Wigren, J., Greving, D.J., Shadley, J.R., Rybicki, "Residual stresses as a factor in the selection of tungsten carbide coatings for a jet engine application", Journal of Thermal Spray Technology, vol. 4, p 268-274, 1995.

[44] H. Li, K. A. Khor, and P. Cheang, Properties of heat-treated calcium phosphate coatings deposited by high-velocity oxy-fuel (HVOF) spray, *Biomaterials*, **23**, 2002, 2105-2112.

[45] R. Okada, Effect of heat treatment on characteristics of high velocity oxygen-fuel flame sprayed coatings (WC-27 mass%NiCr) *Journal of Japan Institute of Metals*, **61**, 1997, 625-628.

[46] S. Watanabe, T. Tajiri, N. Sakoda, and J. Amano, Fatigue cracks in HVOF thermally sprayed WC-Co coatings, *Journal of Thermal Spray Technology*, 7(1), Mar. 1998, 93-96.

[47] I. Natalia-Sora, F. Mor, G. M. La Vecchia, and M. Zocchi, Structural Changes in High Velocity Oxy-Fuel Sprayed Cr_2C_2/NiCr 75/25 Coatings after Annealing Treatments Materials Science Form, 1998, 278-281, 520-525.

[48] D. A. Stewart, P. H. Shipway, and D. G. McCartney, Influence of heate tretment on the abrasive wear behavior of HVOF sprayed VC-Co coatings, *Surface and Coatings Technology*, **105**, 1998, pp.13-24.

[49] K. Hamashima, , Y. Shinozaki, and M. Sasaki, Thermal spraying of Mo_2NiB_2-Ni cermet, pp.2.43-2.49.

[50] M. Eskner, *Mechanical Behavior of Gas Turbine Coatings*, Doctoral Thesis, Department of Materials Science and Engineering, Royal Institute of Technology, Stockholm, Sweden, 2004.

[51] R. Knight, D. Zhangxiong, E. H. Kim, and R.W. Smith, Influence of bondcoat surface characteristics on the performance of TBC systems, Proceedings of the 15th International Thermal Spray Conference, Nice, France, 1549-1554, 25-29 May 1998.

[52] E. Strock, P. Ruggiero, and D. Raynolds, The effect of off-angle spraying on the structure and properties of HVOF WC/CoCr coatings, *Journal of Thermal Spray Coatings*, 2001 pp.671-676.

[53] C. H. Chang, and R. L. Moore, Numerical simulation of gas and particle flow in a high-velocity oxygen-fuel (HVOF) torch, *Journal of Thermal Spray Technology*, 4(4), December 1995, pp.358-366.

[54] O. Knotek, and U. Schnaut, Numerical simulation of the influences of HVOF spraying parameters on coating properties, Proceedings of the 1993 National Thermal Spray Conference, Anaheim, CA, USA, 7-11 June 1993, pp.7-12.

[55] S. Tuurna, P. Vuoristo, S. Ahmaniemi, T. Mantyla, and J. Takeuchi, MCrAlY coatings sprayed with HVOF and VPS processes, VTT Symposium (Valtion Teknillinen Tutkimuskeskus), 2001, 211, 163-172.

[56] M. H. Staia, T. Valente, C. Bartuli, D. B. Lewis, C. P. ConsTable, A. Roman, J. Lesage, D. Chicot, and G. Mesmacque, Part II: Tribological performance of Cr_3C_2-25% NiCr reactive plasma sprayed coatings deposited at different pressures, *Surface and Coatings Technology*, **146-147**, 2001, pp.563-570.

[57] L. Zhao, and E. Lugscheider, High velocity oxy-fuel spraying of NiCoCrAlY and an intermetallic NiAl-TaCr alloy, *Surface and Coatings Technology*, **149**, 2002, pp.231-235.

[58] E. Lugscheider, C. Herbst, L. Zhao, Parameter studies on high-velocity oxy-fuel spraying of MCrAlY coatings, *Surface and Coatings Technology*, **108-109**, 1998, 16-23.

[59] H. Hamatani, and Y. Miyazaki, Optimization of an electron beam remelting of HVOF sprayed alloys and carbides, *Surface and Coatings Technolgy*, **154**, 2002, pp.176-181.

[60] H. D. Steffens, and K. Nassenstein, Influence of the spray velocity on arc-sprayed coating structures, *Journal of Thermal Spray Technology*, **8**(3), 1999, pp.454-460.

[61] K. Dobler, H. Kreye, and R. Schwetzke, Oxidation of stianless steel in the high velocity oxy-fuel process, *Journal of Thermal Spray Technology*, **9**(3), 2000, pp.407-413.

[62] W. Lih, S. H. Yang, C. Y. Su, S. C. Huang, I. C. Hsu, and M. S. Leu, Effects of process parameters on molten particle speed and surface temeprature and the properties of HVOF CrC/NiCr coatings, *Surface and Coatings Technology*, **133-134**, 2000, pp.54-60.

[63] R. C. Tucker, Jr., and A. A. Ashary, Advanced thermsl spray coatings for corrosion and wear resistance, in *Advances in Coatings Technologies for Corrosion and Wear Resistant Coatings*, Ed. A. R. Sivastsa, C. R. Clayton, and J. K. Hirvonen, The Minerals, Metals & Materials Society, 1995, pp.89-98.

[64] H. Edris, G. D. McCartney, A. J. Sturgeon, Microstructural characterization of high velocity oxy-fuel sprayed coatings of Inconel 625, Journal of Material Science, Vol. 32 (4), 863-872.

[65] V. Higuera, F. J. Belzunce, A. Carriles, and S. Poveda, Influence of the thermal-spray procedure on the properties of a nickel-chromium coating, *Journal of Material Science*, **37**, 2002, 649-654.

[66] S. V. Joshi, and R. Sivakumar, Particle behavior during high velocity oxy-fuel spraying, *Surface and Coatings Technology*, **50**, 1991, pp.67-74.

[67] N. Ait-Messaoudene, and A. A. El-Hadj, Effect of the substrate and of thermophoresis on the acceleration and heating of particles during HVOF spraying, *Surface and Coatings Technology*, **106**, 1998, pp.140-144.

[68] A. Sturgeon, High velocity oxy-fuel spraying, *IMF*, **72**(4), 1994, 139-140.

[69] X. M. Li, Y. Y. Yang, T. M. Shao, Y. S. Jin, and G. Barbezat, Impact wear performances of Cr_3C_2-NiCr coatings by plasma and HVOF spraying, *Wear*, **202**, 1997, 208-214.

[70] W. A. Baeslack, III, and W. A. Baeslack, Evaluation of triplex postweld heat treatments for alpha-beta titanium alloys, *Welding Journal*, **61**(6), 1982, 197. s-199.

[71] F. Tang, L. Ajdelsztajn, G. E. Kim, V. Provenzano, and J. M. Schoenung, Effects of surface oxidation during HVOF processing on the primary stage oxidation of CoNiCrAlY coating, *Surface & Coatings Technology*, **185**, 2004, 228-233.

[72] J. Tuominen, P. Vuoristo, T. Mäntylä, M. Kylmälahti, J. Vihinen, P. H. Andersson, Properties of nickel superalloy coatings as-sprayed and with Nd-YAG laser remelting, *Journal of Thermal Spray Technology*, 589-596.

[73] D. Zhangxiong, R. Knight, and R. W. Smith, Effect of bond coat processes and surface characteristics on the failure mechanism of thermal barrier coatings, Thermal Spray 2001: *New Surfaces for a New Millennium*, Ed. C. C. Brandt, K. A. Khor, and E. F. Lugscheider, ASM International, Ohio, USA, 2001.

[74] A. Neville, T. Hodgkiess, Corrosion behavior and microstructure of two thermal spray coatings, *Surface Engineering*, **12**(4), 1996, 303-312.

[75] Y. Itoh, M. Saitoh, M. Tamura, Characteristics of MCrAlY coatings sprayed by high velocity oxygen-fuel spraying system, *Journal of Engineering for Gas Turbines and Power*, **122**, 2000, 43-49.

[76] T. Teratani, K. Tani, and Y. Harada, Reaction diffusion behavior of thermally sprayed MCrAlY coatings on Ni-based super alloys, Thermal Spray 2001: *New Surfaces for a New Millennium*, Ed. C. C. Brandt, K. A. Khor, and E. F. Lugscheider, ASM International, Ohio, USA (2001).

[77] V. Panova, R. Vignjevica, N. Bourneb, and J. Milleta, Material failure modelling in metals at high strain rates, American Institute of physics, 2006, 646-649.

[78] Kh. G. Schmitt-Thomas, H. Haindl, D. Fu, Modifications of thermal barrier coatings (TBCs), *Surface and Coatings Technology*, **94-95**, 1997, 149-154.

[79] H. Gassot, T. Junquera, V. Ji, M. Jeandin, V. Guipont, C. Coddet, C. Verdy, and L. Grandsire, Comparative Study of Mechanical Properties and Residual Stress Distributions of Copper Coatings Obtained by Difference Thermal Spray Processes, *Surface Engineering*, **17**(4), 2001, 317-322.

[80] F. Tang, L. Ajdelsztajn, and J. M. Schoenung, Influence of cryomilling on the morphology and composition of the oxide scales formed on HVOF CoNiCrAlY coatings, *Oxidation of Metals*, **61**, 2004, 219-238.

[81] S. Gray, M. P. Taylor, E. Chau, and H. E. Evans, Evaluation of the critical oxide thickness to initiate spallation from a LPPS CoNiCrAlY coating, *The Journal of Corrosion Science and Engineering*, **6**, p.p.3-16. Paper presented at the conference "Corrosion Science in the 21st Century," UMIST, July 2003.

[82] V. V. Sobolev, J. M. Guilemany, and J. A. Calero, Thermal processes in HVOF sprayed WC-Co coating on a copper substrate, *Journal of Thermal Spray Technology*, **7**(2), June 1998, pp.191-192.

[83] R. Wang, and J. Ru, Investigation on the microstructure changes of NiCrAlY coating due to shot peening plastic deformation and aging, The 7th International Conference on Shot Peening, Institute of Precision Mechanics, warsaw, Poland, p.p. 33-41,1999

[84] A. Scrivani, U. Bardi, L. Carratiello, A. Lavacchi, F. Niccolai, and G. Rizzi, "A comparative study of high velocity oxygen fuel, vacuum plasma spray, and axial plasma spray for the deposition of CoNiCrAlY bond coat alloy," *Journal of Thermal Spray Technology*, **12**, 2003, 504-507.

[85] A. Scrivani, S. Ianelli, A. Rossi, R. Groppetti, F. Casadei, and G. Rizzi, "A contribution to the surface analysis and characterization of HVOF coatings for petrochemical application," *Wear*, **250**, 2001, 107-113.

[86] R. Schwetzke, and H. Kreye, Microstructure and properties of tungsten carbide coatings sprayed with various high-velocity oxygen fuel spray systems, *Journal of Thermal Spray Technology*, **8**(3), 1999, pp.433-439.

[87] M. Mohanty, R. W. Smith, M. De Bonte, J. P. Celis, and E. Lugscheider, "Sliding wear behavior of thermally sprayed 75/25 Cr_3C_2/NiCr wear resistant coatings," *Wear*, **198**, 1996, pp.251-266.

[88] V. V. Sobolev, J. M. Guilemany, and J. A. Calero, Development of coating structure and adhesion during high velocity oxygen-fuel spraying of WC-Co powder on a copper substrate, *Journal of Thermal Spray Technology*, **9**(1), 2000, pp.100-106.

[89] M. L. Lau, V. V. Gupta, and E. J. Lavernia, Mathematical modeling of partricle behavior of nanocrystalline Ni during high velocity oxy-fuel thermal spray, *NanoStructured Materials*, **10**(5), 1998, pp.715-722.

[90] P. Ganesan, G. D. Smith, and D. H. Yates, Performance of Inconel alloy 617 in actual and simulated gas turbine environments, *Materials and Manufacturing Processes*, **10**(5), 1995, pp.925-938.

[91] J. R. Rairden, M. R. Jackson, J. R. Ross, and W. A. Seaman, Plasma-sprayed alloys considered for an advanced concept for a gas turbine bucket, *Thin Solid Films*, **73**, 1980, pp.37-42. Paper presented at the International Conference on Metallurgical Coatings, San Diego, California, USA, April 21-25, 1980.

[92] N. Sakaklbara, Development of high quality thermal spayed metal coating process by shielding control, *proceedings of the international Thermal spray conference 2004*, 595-599

[93] B. S. Yilbas, M. Khalid, and B. J. Abdul-Aleem, Corrosion behavior of HVOF coated sheets, *Journal of Thermal Spray Technology*, **12**(4), 2003, 572-575.

[94] F. Khalid, S. Benjamin, effect of deformation on the oxidation of Inconel superalloy, ICEM14, Cancun, Mexico, 31 August, Symposium U, Volume II, p.p. 183-184.

[95] L. Singheiser, R. Steinbrech, W. Quadakkers, R. Herzog, Failure aspects of thermal barrier coatings, Materail at high temperturs 18(4), p.p. 249-259.

[96] Shaanxi Haven Equipment & Trading Co., Ltd. 10804 Reisen-Yunfeng Building, No. 29 Nan Er Huan East Road, Xi'An, China

[97] L. F. Kawashita, D. R. Moore, and J. G. Williams, The development of a mandrel peel test for the measurement of adhesive fracture toughness of epoxy–metal laminates, Journal of Adhesion, 80: 147–167, 2004.

[98] K. C. Tang, A. Faulkner, S. Sen and R. D. Arnell, The finite element analysis of a strain hardening layered medium under normal loading by (a)

a rigid and (b) a deformable indenter, Journal of Strain Analysis Vol. 33 NO 6,IMechE 1998.

[99] M. Benedetti and V. Fontanari, The effect of bi-modal and lamellar microstructures of Ti-6Al-4V on the behaviour of fatigue cracks emanating from edge-notches, Blackwell Publishing Ltd. Fatigue Fract Engng Mater Struct 27, 2004,1073–1089.

[100] BUEHLER® , BUEHLER Worldwide Headquarters 41 Waukegan Rd. P.O. Box 1Lake Bluff, IL 60044-1699 • USA

[101] K. Niihara, R. Morena, and D. P. H. Hasselman, Indentation fracture toughness of brittle materials for palmqvist cracks, *Fracture Mechanics of Ceramics*, **5**, 1983, 97-105.

[102] www.andrew.cmu.edu/course/24-ansys/, About ANSYS, Mechanical Engineering Department, Carnegie Mellon University, 2007

[103] T. Matic and Z. Domazet, Determination of structural stress for fatigue analysis of welded aluminium components subjected to bending, Blackwell Publishing Ltd. Fatigue Fract Engng Mater Struct 28, 2005, 835–844.

[104] asm.matweb.com/search/SpecificMaterial.asp?bassnum=MTP641, 2007

[105] C. Rinaldi, L. Ferravante, F. Uberti Paci, and P. Bianchi, Extensive Characterization of Dense and Corrosion Resistant Coatings Produced by Improved Shrouded Techniques, *Proceedings of the International Thermal Spray Conference*, 2001, 1185-1193.

[106] ASTM E 790, standard test methods for flexural properties of unreinforced and reinforced plastics and electrical insulation, ASM handbook, Mechanical testing, Designation: D 790, 2001.

[107] ASTM E 8M, standard test methods for tension testing of metallic materials, ASM handbook, Mechanical testing, Designation: M 00b, 2000.

[108] ASTM E 466, standard practice for conducting force controlled constant amplitude axial fatigue tests of metallic materials, ASM handbook, Mechanical testing, Designation: E 466-96, 2002.

[109] ASTM E 739, standard practice for statistical analysis of linear or linearized stress- life and strain- life fatigue data, ASM handbook, Mechanical testing,8, ASTM, 1995, pp.363-426.

[110] K. Keshava Murthy, N. B. Potluri, and S. Sundaresan, Fusion zone microstructure and fatigue crack growth behaviour in Ti-6Al-4V alloy weldments, Materials Science and Technology, 13(6), 1997, 503.

Appendix – Formulation of Young's Modulus and Error Analysis

Formulation of Young's Modulus of Coating:

Consider the Figure shown below, the total force applied can be written as:

$$P = P_s + P_c \tag{1.a}$$

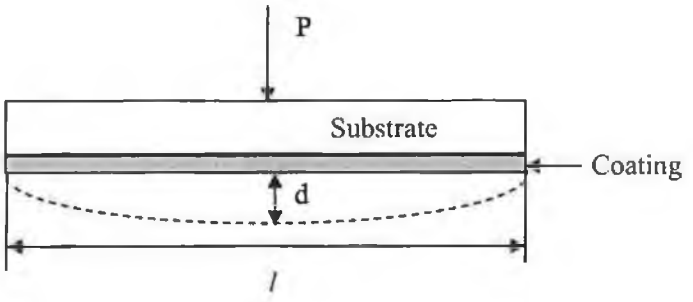

However, in general, the displacement (d) is:

$$d = \frac{Pl^3}{48E_sI_s} \tag{2.a}$$

where l is the length of the coated workpiece (the span between the two supports in three point bending), E_s is the Young's modulus of the substrate material, I_s is the second moment of area of the substrate.

However, displacement is almost the same for the coating and the substrate material, which yields:

$$d = \frac{P_s l^3}{48 E_s I_s} = \frac{P_c l^3}{48 E_c I_c} \tag{3.a}$$

where P_s and P_c are the applied loads corresponding to the substrate material and the coating, respectively and E_c is the Young's modulus of the coating, I_c is the second moment of area of the coating.

Rearrangement of equation 3.a results:

$$P_s = \frac{d(48 E_s I_s)}{l^3} \quad and \quad P_c = \frac{d(48 E_c I_c)}{l^3} \tag{4.a}$$

Substituting into equation 1.a, yields:

$$P = \frac{d(48 E_s I_s)}{l^3} + \frac{d(48 E_c I_c)}{l^3} \tag{5.a}$$

or

$$P = \frac{48d}{l^3}(E_s I_s + E_c I_c) \tag{6.a}$$

Rearrangement gives:

$$\frac{Pl^3}{48d} = (E_s I_s + E_c I_c) \tag{7.a}$$

Finally, Young's modulus of the coating can be written as:

$$E_c = \frac{1}{I_c}\left(\frac{Pl^3}{48d} - E_s I_s\right) \tag{8.a}$$

Error Analysis due to Non-symmetric Coating onto the Substrate Material Situation:

Consider the Figure shown below:

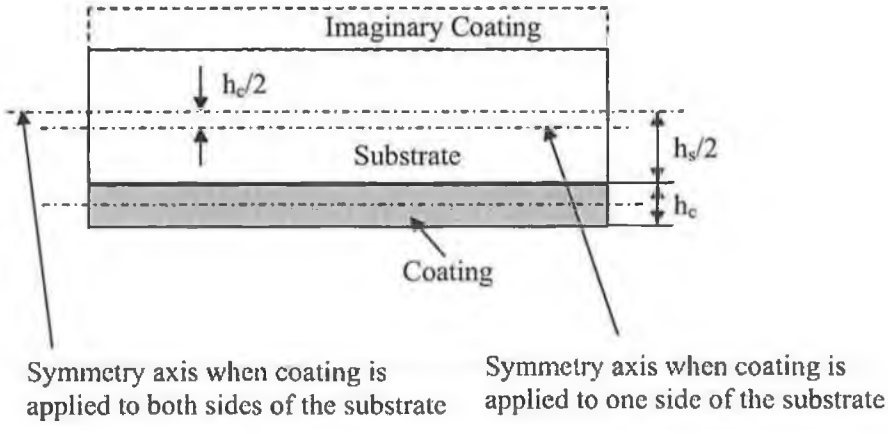

The second moment of area (I_{c_xx}) when coating is applied to both sides can be written as:

$$I_{c_xx} = I_c + (\frac{h_s}{2} - \frac{h_c}{2})^2 bh_c \tag{9.a}$$

where b is the width (normal to the page) of the workpiece.

The second moment of area ($I_{c_x'x'}$) when coating is applied to one sides only can be written as:

$$I_{c_x'x'} = I_c + (\frac{h_s}{2})^2 bh_c \tag{10.a}$$

After taking the ratio of equations (10.a) to equation (9.a) gives:

$$\frac{I_{c_x'x'}}{I_{c_xx}} = \frac{I_c + (\frac{h_s}{2})^2 bh_c}{I_c + (\frac{h_s}{2} - \frac{h_c}{2})^2 bh_c} \tag{11.a}$$

However,

$$I_c = \frac{bh_c^3}{12} \tag{12.a}$$

After the mathematical arrangements, equation 11.a reduces to:

$$\frac{I_{c_x'x'}}{I_{c_xx}} = \frac{\frac{h_c^2}{12} + (\frac{h_s}{2})^2}{\frac{h_c^2}{12} + (\frac{h_s}{2} - \frac{h_c}{2})^2} \qquad (13.a)$$

The error can be calculated from equation 13.a.

INTERNATIONAL JOURNALS AND CONFERENCES

- D. Al-Anazi, M.S.J. Hashmi and B.S. Yilbas, Three-point bend testing of HVOF AMDRY 9954 coating on Ti–6Al–4V alloy, material processing technology, vol.174, 2006, p.p. 204-210.

- D. Al-Anazi, M S J Hashmi and B S Yilbas ,HVOF Sprayed AMDRY 995 Powders onto Ti-6Al-4V Alloy: Tensile Properties, conference of Advances in Materials & Processing Technologies, Las Vegas, USA, 30 July-3 August,2006.

- D. Al-Anazi, M S J Hashmi and B S Yilbas, High-velocity oxy-fuel coating of AMDRY 9954 on to Ti-6Al-4V alloy: fracture toughness measurement, Proceedings of the Institution of Mechanical Engineers, Part B: Journal of Engineering Manufacture, Vol.221, No.4, 2007, p.p. 617-623.

- D. Al-Anazi, M S J Hashmi and B S Yilbas, High-velocity oxy-fuel thermally sprayed CoNiCrAlY coatings on Ti-6Al-4V alloy: high cycle fatigue properties of coating , Proceedings of the Institution of Mechanical Engineers, Part B: Journal of Engineering Manufacture, Vol.221, No.4, 2007, p.p. 647-654.